

---


Electronic Theses and Dissertations, 2004-2019

---

2013

## Monolithically Integrated Broadly Tunable Light Emitters Based On Selectively Intermixed Quantum Wells

Abdullah Zakariya  
*University of Central Florida*

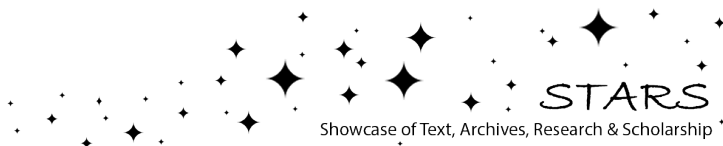
 Part of the [Electrical and Electronics Commons](#)  
Find similar works at: <https://stars.library.ucf.edu/etd>  
University of Central Florida Libraries <http://library.ucf.edu>

This Doctoral Dissertation (Open Access) is brought to you for free and open access by STARS. It has been accepted for inclusion in Electronic Theses and Dissertations, 2004-2019 by an authorized administrator of STARS. For more information, please contact [STARS@ucf.edu](mailto:STARS@ucf.edu).

---

### STARS Citation

Zakariya, Abdullah, "Monolithically Integrated Broadly Tunable Light Emitters Based On Selectively Intermixed Quantum Wells" (2013). *Electronic Theses and Dissertations, 2004-2019*. 2810.  
<https://stars.library.ucf.edu/etd/2810>



MONOLITHICALLY INTEGRATED BROADLY TUNABLE LIGHT  
EMITTERS BASED ON SELECTIVELY INTERMIXED QUANTUM WELLS

by

ABDULLAH J. ZAKARIYA

B.S. in Electrical Engineering, College of Engineering, Florida Institute of Technology, 2000

M.S. in Electrical Engineering, College of Engineering, Florida International University, 2007

A dissertation submitted in partial fulfillment of the requirements  
for the degree of Doctor of Philosophy  
in the Department of Electrical Engineering and Computer Science  
in the College of Engineering and Computer Science  
at the University of Central Florida  
Orlando, Florida

Summer Term  
2013

Major Professor: Patrick LiKamWa

© 2013 Abdullah J. Zakariya

## ABSTRACT

A monolithically integrated broadly tunable MQW laser that utilizes a combined impurity-free vacancy disordering (IFVD) of quantum wells and optical beam steering techniques is proposed and investigated experimentally. The device consists of a beam-steering section and an optical amplifier section fabricated on a GaAs/AlGaAs quantum well (QW) *p-i-n* heterostructure. The beam steering section forms a reconfigurable optical waveguide that can be moved laterally by applying separately controlled electrical currents to two parallel contact stripes. The active core of the gain section is divided into selectively intermixed regions. The selective intermixing of the QW in the gain section results in neighboring regions with different optical bandgaps. The wavelength tuning is accomplished by steering the amplified optical beam through the selected region where it experiences a peak in the gain spectrum determined by the degree of intermixing of the QW. The laser wavelength tunes to the peak in the gain spectrum of that region. The IFVD technique relies on a silica (SiO<sub>2</sub>) capped rapid thermal annealing and it has been found that the degree of intermixing of the QW with the barrier material is dependent on the thickness of the SiO<sub>2</sub> film. The QW sample is first encapsulated with a 400nm thick SiO<sub>2</sub> film grown by plasma enhanced chemical vapor deposition (PECVD). In the gain section, the SiO<sub>2</sub> film is selectively etched using multiple photolithographic and reactive ion etching steps whereas the SiO<sub>2</sub> film is left intact in all the remaining areas including the beam-steering section. The selective area quantum well intermixing is then induced by a single rapid thermal annealing step at 975°C for a 20s duration to realize a structure with quantum well that has different bandgaps in the key regions. Optical characterizations of the intermixed regions have shown a blue shift of peak of the electroluminescence emission of 5nm, 16nm and 33nm for the uncapped, 100nm and 200nm

respectively when compared to the as grown sample. The integrated laser exhibited a wavelength tuning range of 17nm (799nm to 816nm).

Based on the same principle of QW selective intermixing, we have also designed and fabricated a monolithically integrated multi-wavelength light emitting diode (LED). The LED emits multiple wavelength optical beams from one compact easy to fabricate QW structure. Each wavelength has an independent optical power control, allowing the LED to emit one or more wavelengths at once. The material for the LED is the same AlGaAs/GaAs QW *p-i-n* heterostructure described above. The device is divided into selectively intermixed regions on a single QW structure using IFVD technique to create localized intermixed regions. Two different designs have been implemented to realize either an LED with multiple output beams of different wavelengths or an LED with a single output beam that has dual wavelength operation capabilities. Experimental results of the multiple output beams LED have demonstrated electrically controlled optical emission of 800nm, 789nm and 772nm. The single output LED has experimentally been shown to produce wavelength emission of 800nm and/or 772nm depending on electrical activation of the two aligned intermixed regions.

To my family and my friends: For their continuous support throughout this journey.

## ACKNOWLEDGMENTS

I am very grateful to my advisor, Dr. Patrick LiKamWa, for giving me the opportunity to work with him over the last few years. I would also like to thank the dissertation committee members for their time and effort. Also my appreciation to my fellow group members past, present and visiting researchers, Dr. Nathan Bickel, Dr. Daniel May-Arrijoja, Dr. Tony Ho, and Enrique Lopez. I would also like to mention Dr. Bassam Alfeeli, Edris Sarailou, Abhijeet Ardey, James Ross, Matt Weed and Dr. Scott Webster, and to all the CREOL students, staff, and faculty, thank you.

Moreover, I want to express my gratitude for the Ministry of Interior-Kuwait for the financial support, and also Information Technology and Communication Sector undersecretary Sheikh Mishal Al-Jaber Al-Abdullah Al-Sabah for his moral support though out my time at UCF.

I would also extend my appreciation to IEEE, OSA and SPIE organizations for considering and publishing my work and results in their conferences which really validated my dissertation. I also would like to the editors for permitting me to use those publications as a part of my dissertation.

## TABLE OF CONTENTS

LIST OF FIGURES .....	xii
LIST OF TABLES .....	xvi
LIST OF ACRONYMS .....	xvii
CHAPTER 1: INTRODUCTION .....	1
1.1 Outline.....	3
CHAPTER 2: SEMICONDUCTOR MULTIPLE QUANTUM WELLS MATERIAL THEORY AND PRINCIPLES .....	5
2.1 Semiconductor Theory and Principles .....	5
2.2 Quantum Wells.....	9
2.3 Light Emitting Diodes (LEDs).....	11
2.4 Semiconductor Lasers .....	14
2.5 Impurity Free Vacancy Disordering (IFVD)/ Quantum Well Intermixing (QWI) .....	16
2.6 Current Induced Guiding.....	18
CHAPTER 3: ALL-OPTICAL PROGRESSIVELY INTERMIXED QW WAVEGUIDES.....	21
3.1 Introduction .....	21
3.2 Device Design and Simulations .....	24
3.3 Device Fabrication .....	24
3.3.1 Mask Design and fabrication .....	25
3.3.2 SiO <sub>2</sub> film deposition.....	26



3.3.3	Rapid thermal annealing .....	27
3.3.4	Photolithography .....	27
3.3.5	Wet etching .....	28
3.4	Testing and Results .....	29
CHAPTER 4: BEAM STEERING OVER SELECTIVELY INTERMIXED REGIONS.....		33
4.1	Introduction .....	33
4.2	Principle of Operation for the Proposed Tunable Laser Device .....	34
4.3	Device Design .....	35
4.4	Device Fabrication .....	37
4.4.1	Mask design and fabrication .....	38
4.4.2	Metal evaporation .....	38
4.4.3	SiO <sub>2</sub> film deposition.....	39
4.4.4	Photolithography.....	39
4.4.5	Reactive Ion Etching (RIE).....	40
4.4.6	Repeat of 4.4.4 and 4.4.5 .....	40
4.4.7	Rapid Thermal Annealing (RTA) .....	40
4.4.8	Wet Etching .....	41
4.4.9	P-type contacts deposition .....	42
4.4.10	Sample polishing.....	42
4.4.11	Repeat of 4.4.9 .....	43

4.5	Testing and Results .....	43
4.6	Conclusion.....	47
CHAPTER 5: SELECTIVELY INTERMIXED MQW TUNABLE LASER .....		49
5.1	Introduction .....	49
5.2	Device Design .....	50
5.3	Fabrication.....	51
5.3.1	Mask design and fabrication .....	51
5.3.2	Metal evaporation .....	52
5.3.3	SiO <sub>2</sub> film deposition.....	52
5.3.4	Photolithography.....	53
5.3.5	Reactive Ion Etching (RIE).....	53
5.3.6	Repeat of 5.3.4 and 5.3.5 .....	53
5.3.7	Repeat of 5.3.6 for the sample with three intermixed regions only .....	54
5.3.8	Rapid Thermal Annealing (RTA) .....	54
5.3.9	Wet Etching .....	55
5.3.10	P-type contacts deposition .....	55
5.3.11	Sample Polishing .....	55
5.3.12	N-type contacts deposition.....	55
5.4	Testing and Results .....	56
5.5	Conclusion.....	67

## CHAPTER 6: MONOLITHIC DUAL & MULTI-WAVELENGTH LIGHT EMITTING

DIODES .....	68
6.1 Introduction .....	68
6.2 Dual-Wavelength LED.....	69
6.3 Multi Wavelength Diode.....	70
6.4 Device Design .....	71
6.4.1 Dual Wavelength LED.....	71
6.4.2 Multi Wavelength LED.....	72
6.5 Dual Wavelength LED Fabrication.....	73
6.5.1 Step one.....	73
6.5.2 Step two .....	74
6.5.3 Step three .....	74
6.5.4 Step four.....	74
6.5.5 Step five .....	75
6.5.6 Step six.....	76
6.5.7 Step seven .....	76
6.5.8 Step eight .....	76
6.5.9 Step nine.....	76
6.6 Multi Wavelength LED Fabrication.....	77
6.6.1 Step one.....	77

6.6.2	Step two .....	77
6.6.3	Step three .....	78
6.6.4	Step four.....	78
6.6.5	Step five .....	78
6.6.6	Repeat of steps four and five .....	78
6.6.7	Step six.....	78
6.6.8	Step seven .....	79
6.6.9	Step eight .....	79
6.6.10	Step nine.....	79
6.7	Testing and Results .....	80
6.8	Conclusion.....	84
CHAPTER 7: CONCLUSIONS & FUTURE WORK .....		86
LIST OF REFERENCES.....		89

## LIST OF FIGURES

Figure 2-1 Energy band diagram .....	6
Figure 2-2 Energy band diagram .....	8
Figure 2-3 Energy levels in a potential well and its wavefunctions .....	10
Figure 2-4 LED emission process as forward voltage is applied.....	13
Figure 2-5 Laser emission process as electrical current is applied.....	15
Figure 2-6 The shift in the absorption due to IFVD/QWI thermal annealing .....	17
Figure 2-7 (a) Steering area with no current injected (b) Injected current effect forming a waveguide .....	20
Figure 3-1 Proposed System overview showing the test device. The input waveguides lead light into the steering beam section where the progressively disordered area is surrounded by metal contacts with different spacing .....	22
Figure 3-2 System overview showing the fabricated test device.....	24
Figure 3-3 Fabricated masks showing waveguides and disordered areas.....	25
Figure 3-4 graded sample and an inset of the graded SiO <sub>2</sub> film .....	27
Figure 3-5 Fabrication process steps.....	28
Figure 3-6 Photoluminescence set-up.....	29
Figure 3-7 Change in bandgap energy compared to as grown sample for different cap thicknesses .....	30
Figure 3-8 Photoluminescence peaks of the graded sample and an inset of the graded SiO <sub>2</sub> film	30
Figure 3-9 Labview controlled optical setup for measurements of the waveguide transmission characteristics.....	31
Figure 3-10 Transmission spectra of the progressively disordered waveguides .....	32

Figure 4-1 Proposed Device.....	35
Figure 4-2 Fabricated Device.....	36
Figure 4-3 Fabricated Device.....	37
Figure 4-4 Fabricated Device.....	38
Figure 4-5 Selectively intermixed regions of the steering section.....	41
Figure 4-6 Fabricated device .....	43
Figure 4-7 Electroluminescence spectra of samples intermixed using different thicknesses of SiO <sub>2</sub> .....	44
Figure 4-8 Experimental set-up .....	45
Figure 4-9 A close up picture showing two selectively intermixed regions bounded by contacts.....	45
Figure 4-10 Electroluminescence and laser beam output .....	46
Figure 4-11 Electroluminescence and laser beam output .....	46
Figure 4-12 steering sequence .....	47
Figure 5-1 Schematic drawing of the first device design .....	50
Figure 5-2 Schematic drawing of the second device design.....	51
Figure 5-3 Schematic drawing of the second device design.....	52
Figure 5-4 Three selectively intermixed regions .....	55
Figure 5-5 Schematic drawings of the fabrication steps for both devices .....	56
Figure 5-6 Schematic of the electrical controllers circuit.....	57
Figure 5-7 Experimental set-up .....	58
Figure 5-8 L-I curves .....	58
Figure 5-9 Final Device .....	60
Figure 5-10 700μm laser device wavelength tuning.....	61

Figure 5-11 L-I curve for the lasers with three intermixed regions .....	62
Figure 5-12 L-I curve.....	63
Figure 5-13 Electroluminescence emission across the facet.....	63
Figure 5-14 Laser facet intensity profile.....	64
Figure 5-15 Three selectively intermixed QW regions of uncapped, 100nm and 200nm thick SiO <sub>2</sub> of the fabricated device .....	65
Figure 5-16 Output spot moving across the facet .....	65
Figure 5-17 Wavelength tunability for the three intermixed region laser.....	66
Figure 6-1 Proposed device with three selectively intermixed regions .....	69
Figure 6-2 Fabricated device with two selectively intermixed regions .....	71
Figure 6-3 System overview showing the fabricated test LED device .....	73
Figure 6-4 Dual wavelength LED contacts mask .....	74
Figure 6-5 System overview showing the fabricated test LED device .....	75
Figure 6-6 (a) Sequence pictures showing: 1.Three fabricated LED devices, 2.Current applied to the 400nm SiO <sub>2</sub> intermixed region, 3. Current applied to the uncapped region and 4.Current applied to both regions.....	76
Figure 6-7 Multi Wavelength LED contacts mask design.....	77
Figure 6-8 System overview showing the fabricated test LED device .....	79
Figure 6-9 shows sequence pictures of the top view of the device with different combinations of current applied to two contacts of the device.....	80
Figure 6-10 Device output spectrum.....	82
Figure 6-11 (a) Three output device test orientation (b) Single output device test orientation ....	83
Figure 6-12 Sequence picture of the device under test .....	83

Figure 6-13 Device output spectra ..... 84



## LIST OF TABLES

Table 2-1 Some III-V compounds and their bandgap energies .....	12
Table 5-1 Gain Section L-I curve values .....	59
Table 5-2 Steering and tunability current injection values for the device with 700 $\mu$ m gain section .....	60
Table 5-3 Gain section L-I curve values.....	61
Table 5-4 Steering and tunability current injection values .....	66

## LIST OF ACRONYMS

BER	Bit Error Rate
BOE	Buffered Oxide Etchant
DOS	Density of States
IID	Impurity Induced Disorder
IFVD	Impurity Free Vacancy Disorder
MEMS	Micro-Electro-Mechanical Systems
MMI	Multimode Interference
MOCVD	Metalorganic Chemical Vapor Deposition
MQW	Multiple Quantum Well
PECVD	Plasma Enhanced Chemical Vapor Deposition
PL	Photoluminescence
QW	Quantum Well
QWI	Quantum Well Intermixing
RIE	Reactive Ion Etching
RTA	Rapid Thermal Annealing
TE	Transverse Electric
TM	Transverse Magnetic
SEM	Scanning Electron Microscope
WCE	Wet Chemical Etching
WDM	Wavelength Division Multiplexing

## CHAPTER 1: INTRODUCTION

Telecommunication technology has made a tremendous jump in the last 40 years. Microwave wireless communication and coaxial cables have been the main transmission medium for communication and are still in use today; however, both have their drawbacks. Firstly coaxial cable is capable of transmitting only around 300 voice channels or a single television channel because the bandwidth is limited by the frequency dependent cable losses which increases rapidly for high frequencies [1, 2]. In wireless microwave communication systems, the bit error rate (BER) is limited by carrier frequency [3], and the range is affected by weather conditions. In addition, purely microwave systems sites can be very expensive due to the need for the installation and maintenance of communication towers for antennas and high power radio transceivers. Moreover, microwave signals can only travel over a limited range before the need arises for one or more repeaters to relay the signal over long distances, which adds to the total number of required sites [4].

Scientists have long realized that optical waves can be adapted to serve as carrier frequencies, but it wasn't until the 1960's when an actual medium for optical waves was available. Thereafter, a switch to optical communication systems was carried out to overcome the shortcomings of traditional communication systems. When fiber optic cables were introduced, researchers found that there are low-loss transmission windows in the optical spectrum that allows optical waves to propagate in fiber optic cables over very long distances. Ever since the introduction of fiber optic communication, research for newer and better active components for optical communication systems has been relentlessly pursued. Active components development such as III-V semiconductor lasers operating at room temperature and especially InGaAsP

semiconductor lasers operating at 1.3 $\mu\text{m}$  and 1.55 $\mu\text{m}$ [5] wavelengths were being developed at the same time that research was being conducted on optical fibers. These and other research resulted in a series of generations of lightwave systems with innovations such as low loss fibers [6], fiber amplifiers [7, 8], new wavelengths diode lasers and wavelength division multiplexing (WDM) [1, 9-13].

More recently, it has been recognized that photonic integrated circuits based on III-V semiconductors are the way forward in which both electronic, electro-optical and all-optical information control can be achieved, with multiple functionalities, such as modulation, amplification, detection, and switching, combined into a single construct. Heterostructures employing InP and GaAs material systems typically have broad operational bandwidths, which can be well matched to optical fiber transmission windows. The active layer materials in these structures have transitioned from bulk semiconductors to quantum wells [14, 15]. Signal processing in optical communication networks continuously strives for faster and more efficient optical components that can perform multiple functions for telecommunication networks signal processing [16-18]. Optical switching and laser scanning, semiconductor lasers and optical beam steering can provide an attractive functionality needed for such applications [3, 19-26]. Electromechanically beam steering devices which are implemented using micro-electromechanical systems (MEMS) consist of a free space suspended beam which acts as a cantilever to direct light to different arrays or acts as an on/off switch [27-29]. Moreover, broadly tunable laser diodes are not only limited to the communications field applications, they are widely used in environmental sensing applications such as atmospheric spectroscopy and chemicals detection [30-35]. Tunable lasers have been proven to be an excellent spectroscopic source to be used environmentally monitoring systems. These systems can monitor air and water

quality, industrial emissions. Moreover, tunable lasers are a good tool for atmospheric chemistry, which is utilized in national security for chemical warfare. It also used in several medical diagnosis equipment and cancer cells recognitions [36-38].

III-V semiconductors have also shown great potential for their applications in Light Emitting Diodes (LEDs). LEDs have recently become a target of the electronics industry due to its versatility that ranges from everyday consumer uses to specialized technological applications including medical uses. For example, LEDs have shown promising results in medical research where it is used in monitoring blood pressure, hair therapy and dermatology [39, 40]. Furthermore, LEDs are also being used in archeological research to provide a non-invasive sample analyses [41-43]. In addition, visible LEDs are widely marketed as a compliant future green technology that would replace compact fluorescent lighting units [44-46]. LEDs allow lower power consumption, are longer lasting, and give very little heat dissipation. They provide a brighter display, with thinner and smaller panels, as well as better visual contrast levels. Commercial multicolor LED products are in high demand and have already taken over as the main components for specialized light fixtures and digital TV displays. LEDs are now used mainly as backlights for high end displays and monitors [44, 47], however size and fabrication complexity in producing multicolor LEDs are still main challenges that the industry has to overcome.

## 1.1 Outline

In this work, epitaxially grown GaAs/AlGaAs multiple quantum wells (MQW) and single quantum well (QW) steering devices and lasers have been designed, simulated, fabricated and tested. The optical properties of the materials have been characterized by either optical pumping or electrical carrier injection. Chapter two discusses the underlying theory and principles

semiconductor optoelectronics; mainly, III-V materials and QW structures used in the proposed devices and their optical and optoelectronic properties. A brief background of semiconductor lasers, quantum wells and pin junctions are reviewed. Furthermore, techniques of Impurity Free Vacancy Disordering (IFVD), Quantum Well Intermixing (QWI) are studied and explained. In this work we show two novel ideas of a tunable laser and a multi wavelength LED. The tunable laser device is explored in three steps discussed in chapters three to five. Chapter three discusses the characterization of selectively intermixed QW optical waveguides design which is the foundation for the final device. This chapter also addresses simulations and optical characterization of partially intermixed QWs. Chapter four describes experiments that confirm the ability of guiding and steering an optical beam over a material with regions of selectively engineered energy bandgaps. These regions of engineered bandgaps are obtained by the selective area disordering process in this chapter is based on the optical characterization in the previous chapter. Chapter five shows the final realized designs of two tunable lasers based on the beam steering device. Two different designs are shown in this chapter, one device with two intermixed regions in the gain section and another with three intermixed regions in the gain section. Their performance in the wavelength tuning range is compared. Chapter six discusses two LED designs of different configurations; one LED has a single output with dual wavelength emission. The second design consists of an LED with three adjacent output sections each at emitting light at a different wavelength. Both devices are designed on a single structure using simple reliable fabrication methods. Chapter seven summarizes the work-to-date and discusses future work.

## CHAPTER 2: SEMICONDUCTOR MULTIPLE QUANTUM WELLS

### MATERIAL THEORY AND PRINCIPLES

Semiconductors devices have a huge impact in the evolution of optoelectronic devices. III-V materials are widely used in MEMS, sensors, LEDs, integrated circuits and lasers. AlGaAs based quantum wells materials are used to fabricate all-optical devices and electro-optical devices. This chapter is dedicated to discussing semiconductors, QW semiconductor laser materials and some optical properties which form the core of this work. The chapter is divided into four sections; the first section discusses semiconductor theory and properties of the AlGaAs material which is used for the tunable laser and the LED devices in this research. The second section focuses on quantum well theory and explains how they contribute to the fabricated devices. The third section discusses optical bandgap tuning and engineering techniques of selective area Impurity-Free Vacancy Disorder (IFVD) also known as Quantum Well Intermixing (QWI). Finally, section four explores current induced waveguiding and optical beam steering theory.

#### 2.1 Semiconductor Theory and Principles

Semiconductors materials are the cornerstone of modern optoelectronic devices because of the ability to control the flow of electrons electrically and the energy of electrons optically. In a semiconductor, the energy of electrons are spread over quasi-continuous energy levels in either the valence band or the conduction band with a forbidden energy range that is commonly referred to the bandgap energy. The bandgap energy is the difference in energy between the top of the valence band and the bottom of the conduction band and is the most significant attribute of a semiconductor because it signifies the characteristic energy of photons that are released when excited electrons in the conduction give up their excess energy via a radiative transition to occupy an energy state in the valence band. It is also the minimum energy that is required to

excite electrons from the valence band into the conduction band. Electron excitation can be performed by either electrical pumping via injection of electrons and holes across energy barriers or optical pumping as long as the pump photons have energies that are larger than the bandgap energy.. The wavelength of the photons corresponding to the absorption edge of the semiconductor is related to its bandgap energy by the following formula

$$E_g (eV) = \frac{1.24}{\lambda(\mu m)} \quad (2.1)$$

Fig 2-1 shows a graphic representation of optical pumping that leads to the excitation of an electron from the valence band into the conduction band and the eventual recombination of the electron with the hole to emit a photon.

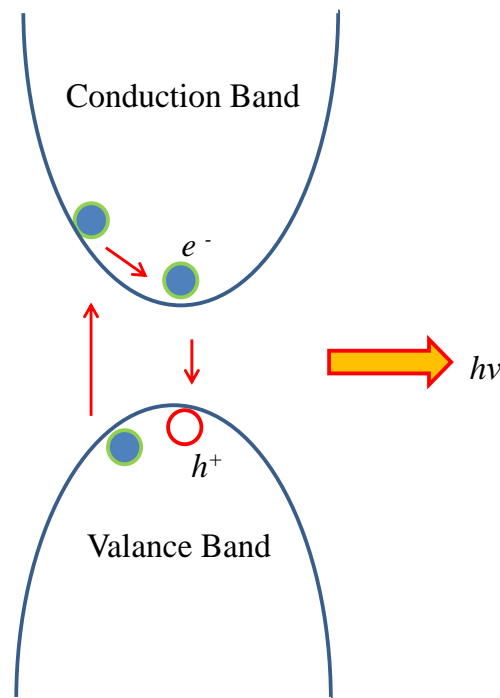


Figure 2-1 Energy band diagram

Whether the electrons are in the conduction band or the valence band is dictated by two important aspects of the semiconductor, the Density of States (DOS) and the Fermi-Dirac functions. The DOS, which is also referred to as  $N(E)$ , represents the number of electronic states



in a band energy per energy per unit volume of the crystal. We can derive the electron concentration in the conduction band and the hole concentration in the valance band from the integrals by calculating the number electron wavefunctions at a certain energy per unit volume of the crystal. The DOS in the conduction band is expressed with the following equation[48].

$$N_c(E) = \frac{\sqrt{2}}{\pi^2} \left(\frac{m_e^*}{\hbar^2}\right)^{\frac{3}{2}} (E - E_c)^{1/2} \quad (2.2)$$

Likewise, the DOS for holes in the valance band can be determined with the following equation

$$N_v(E) = \frac{\sqrt{2}}{\pi^2} \left(\frac{m_h^*}{\hbar^2}\right)^{\frac{3}{2}} (E_v - E)^{1/2} \quad (2.3)$$

The Fermi-Dirac function which provides the probability of finding an electron in any of the quantum states in reference to a virtual energy level, the Fermi energy  $E_F$ , is mathematically represented by

$$f_e(E) = \frac{1}{1 + \exp\left(\frac{E - E_F}{K_B T}\right)} \quad (2.4)$$

Where  $K_B$  is the Boltzmann constant and the product of the Fermi-Dirac function with the DOS function give the energy distribution of electrons in the conduction band and that of holes in the valance band. If we consider a constant DOS, we can graphically represent the electron/hole concentration in Fig# 2-2

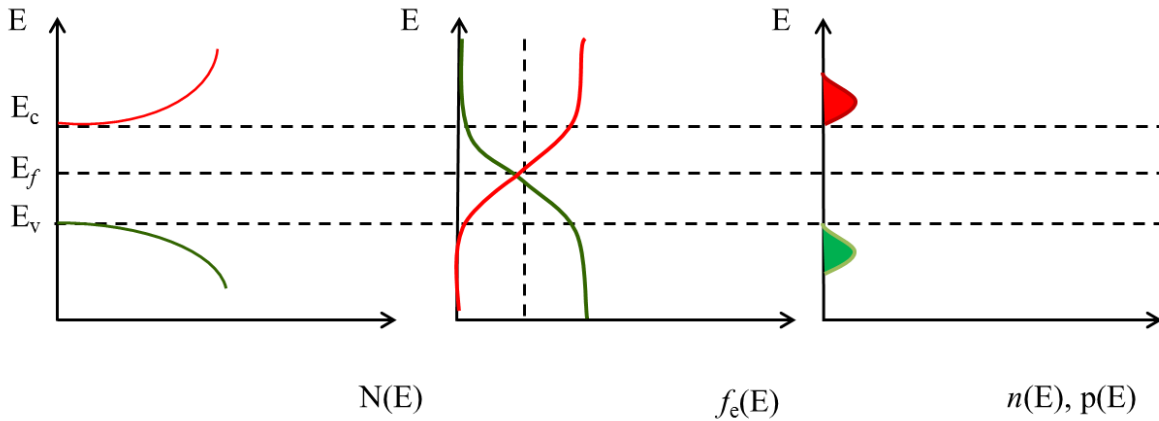


Figure 2-2 Energy band diagram

In a pure (or intrinsic) crystal, the number of electrons in the conduction band (free electrons) is equal to the number of holes in the valence band (free holes). However, the concentration of free electrons (and/or free holes) in a semiconductor can easily be manipulated by the introduction of dopant impurities allowing us the ability to control conductivity and engineer semiconductors to a wide range of application specific requirements. When a semiconductor crystal is doped, it becomes an extrinsic semiconductor, and depending on the dopant impurity the hole to electron ratio will change drastically and the semiconductor will either be a p-type semiconductor that contains a large hole concentration in the valence band or an n-type semiconductor with a large electron concentration in the conduction band.

An optoelectronic device requires separation of free electrons from free holes with a built-in energy potential that can lead to photon generation if the electrons (or holes) can be made to overcome the energy barrier. This can be easily achieved by creating a *p-i-n* structure in which an intrinsic layer is sandwiched between two doped regions, one doped with donor impurities to form the n-type layer and the other one doped with acceptor impurities to form the p-type layer. When voltage is applied to a *p-i-n* junction in the forward bias direction, the holes diffuse across the junction into the intrinsic region and the electrons diffuse across the junction into the same

intrinsic layer. Current flows from the external circuit to replenish the electrons that recombine with the holes in the intrinsic region. Furthermore in order to enhance optoelectronic device performance, the i-region can be made of a semiconductor that has smaller bandgap energy than that of the p and n regions, thereby forming a double heterostructure. The double heterostructure very conveniently blocks the holes injected from the p-side from escaping the i-regions while at the same time it blocks the electrons injected from the n-side from escaping the i-region too. The injected holes/electrons are forced to recombine in the intrinsic layer, which usually has a direct energy band and the excess energy of the electrons is transformed into the creation of photons. Furthermore, the i-regions which has a lower bandgap energy than the p and n regions also naturally has a higher index of refraction following Moss rule and therefore the heterostructure also help to confine the emitted photons to remain in the i-region.

## 2.2 Quantum Wells

A quantum well can be defined as an energy potential that confines the motion of electrons in at least one-dimension. The Heisenberg uncertainty principle shows if a particle is confined in a region of the x-axis with a length of  $\Delta x$  can be defined by the following equation

$$\Delta x = \sqrt{\frac{\hbar^2}{mK_B T}} \quad (2.5)$$

By calculating the quantum size effect of  $\Delta x$  we find that for an electron in a typical semiconductor layer to observe the quantum effect a layer of  $\Delta x$  at least 5nm is required. Another way to consider this is that the physical dimension of the potential well that is required to achieve quantum effect is comparable of the de Broglie wavelength of the electron and is typically less than about 20nm [49]. [49]. An electron in a quantum well has a set of known potential energies that can be solved using Schrödinger's equation. The potential energy levels are solved as eigen values, which are the energies at which an electron can occupy. The potential

energy are represented with eignefunctions and are numbered with respect to the conduction band as shown in Fig 2-3.

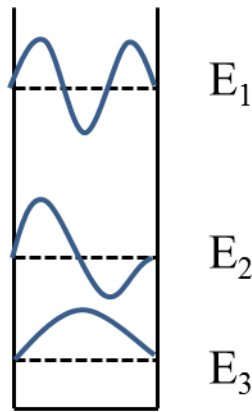


Figure 2-3 Energy levels in a potential well and its wavefunctions

When electrons are present in a quantum well, the quantum confinement prevents the electrons from occupying energies that correspond to the bottom of the conduction band of the semiconductor. Instead, discrete eigen-energies are created as electrons take on a wave-like nature. The energy of the electron wave packets can be calculated from solving the one-dimensional Schrödinger's equation. Because the confinement is only along the crystal growth direction, the eigen-energy values represent the lowest energy state of the electrons in the quantum well for any allowed quantum number. Along the other two crystal directions, the energy of the electron still follows the quasi-continuous parabolic E-k dependence. This leads to a unique DOS for the electrons in the conduction band and the holes in the valence band. In fact the density of allowed states for electrons and holes are constant for each allowed quantum number. This leads to a step-like DOS function for quantum wells instead of the parabolic DOS function for bulk semiconductors. This property accounts for the increased efficiency of QW lasers because the gain coefficient is maximum at the bottom of the allowed energy level as soon as the quasi-Fermi energy levels have moved into the respective QW levels. The clear benefit of

QW lasers is that the threshold current for lasing is reduced considerably and this contributes directly to an improved conversion efficiency from electrical input power to optical output power.

As mentioned in the previous sections, the *p-i-n* structure is the main physical feature of any semiconductor light emitter. However in many instances, the efficiency of the light emission can be improved by the incorporation of one or more quantum wells in the intrinsic layer. The quantum well then becomes the region where electron/hole recombination occurs; hence, the characteristics of the quantum well dictate the properties of the emitted photons.

### 2.3 Light Emitting Diodes (LEDs)

A typical semiconductor light emitting diode (LED) is in fact a *p-n* or *p-i-n* junction made from a direct bandgap semiconductor, such that electron hole recombination results in photon emission.

Various materials of direct bandgap semiconductors are used as LEDs. The most common class of semiconductor materials used consists of the III-V's ternary alloys that cover the visible spectrum to the infrared end of the energy spectrum. For a typical *p-n* LED structure, the fabricated III-V's ternary materials are epitaxially doped semiconductor layers grown on top of a substrate. Usually, the *n-type* layer is highly doped to ensure most of electron-hole recombination is done in the *p-type* side where the light will be emitted. Depending on the required wavelength, different materials can be combined to produce semiconductor LEDs. The III-V compounds are widely used for infrared wavelength emitters and all the way to visible wavelength emitters. Table 2-1 shows some of the binary III-V compounds materials and their bandgap energies. To operate semiconductor LEDs, carriers must be injected across the junction of the semiconductor to start the emission.

Table 2-1 Some III-V compounds and their bandgap energies

Material	Abbreviation	Bandgap energy (eV)
Aluminum arsenide	AlAs	2.16
Gallium arsenide	GaAs	1.42
Indium phosphide	InP	0.36
Gallium nitride	GaN	3.36
Gallium antimonide	GaSb	0.72

The energy of the emitted photon is equal to the transition energy of the electron in the conduction to the hole in the valence band, and this is fairly close to the bandgap energy.

$$h\nu \approx E_g \quad (2.6)$$

Where  $E_g$  is the bandgap energy. Most LEDs are made with a double heterostructure *p-i-n* design such that one barrier at the n-doped semiconductor to the i-layer prevents electrons from diffusing into the i-layer while the other barrier at the p-doped semiconductor to the i-layer prevents holes from diffusing into the i-layer. When the device is forward-biased, the potential barrier  $V_0$  is reduced allowing electrons to diffuse from the n-layer into the i-layer and at the same time holes can diffuse from the p-layer into the i-layer. The recombination of electrons and holes creates spontaneous emission in the i-region as shown in Fig. 2-4

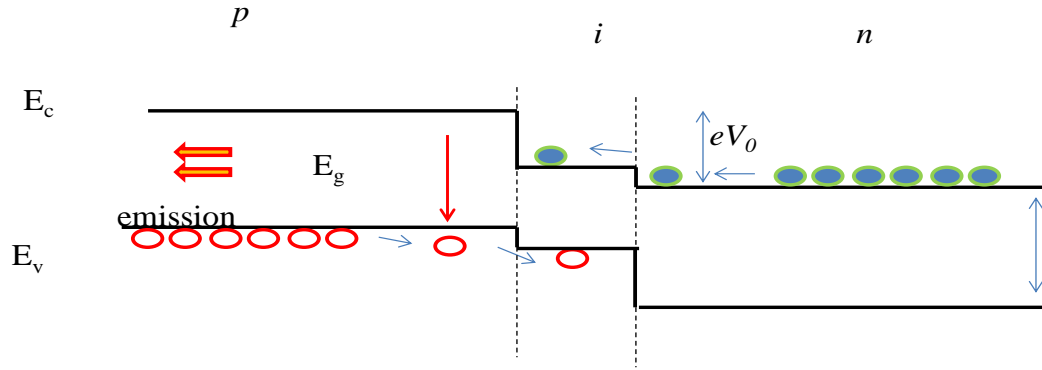


Figure 2-4 LED emission process as forward voltage is applied

The photon generated as a result of the carrier injection is called electroluminescence. For surface emitting LEDs the light that is generated in the active region between the p and n-regions is emitted out of the p-type layer and since that semiconductor has a larger bandgap energy than the active layer, minimum absorption of the emitted photons occurs there.

LEDs overall efficiency ( $\eta_0$ ) and LEDs responsivity are two important properties for any finished LED product. The overall efficiency is a product of three components.

$$\eta_0 = \eta_e \eta_{int} \eta_{inj} \quad (2.7)$$

The first component is the external efficiency ( $\eta_e$ ), which is also known as the extraction efficiency, is defined as the efficiency of converting of electrical power into optical energy. The external efficiency combines the efficiency of the radiative recombination that are extracted out of the structure since not every hole/electron radiative recombination make it out. The second component is the internal efficiency ( $\eta_{int}$ ) which is basically the radiative recombination efficiency of holes/electrons in the depletion region and the injection efficiency. Finally, the injection efficiency ( $\eta_{inj}$ ) which the amount of electron being injected into the active region.

LED responsivity is defined as the ratio of the emitted optical power to the input current in (W/A)

$$\mathcal{R} = \frac{P_0}{I} \quad (2.8)$$

## 2.4 Semiconductor Lasers

Semiconductor lasers have significant advantages over other types of lasers; they are compact, operate with low power and are very energy efficient. As mentioned in section 2.3, different semiconductor materials are combined to produce *p-n* and *p-i-n* junctions in LEDs. That same principle is also applied in semiconductor lasers. However, a *p-i-n* junction is required for a semiconductor laser diode. Similarly, the emitted wavelength depends on the material bandgap.

As forward voltage is applied, the potential barrier is reduced allowing electrons and hole to cross over into the intrinsic region and it becomes highly populated with electrons in the conduction band and holes in the valence band. At this point, there are more electrons near the bottom of in the conduction band than in the narrow range of energies near the top of the valence band resulting in a population inversion. Photons with energy within that energy range experience optical gain when they pass through the active region because they are more likely to cause stimulated emission of the electrons in the conduction band than getting absorbed by electrons in the valence band. The photon energy that is created during the stimulated radiative recombination process is identical to that of the photon that initiates the process. [48, 49]. The recombination of electrons and holes in the i-region creates stimulated emission as shown in Fig.

2-5



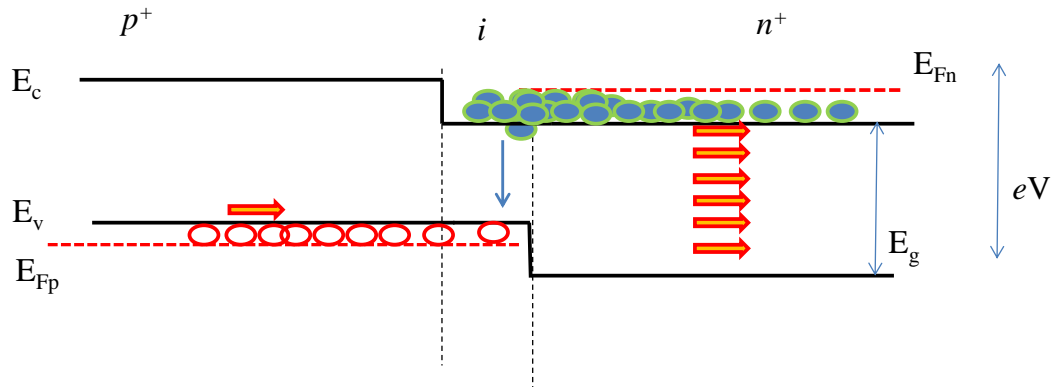


Figure 2-5 Laser emission process as electrical current is applied

As mentioned earlier, a *p-i-n* heterostructure laser is used because it has a significant reduction in the threshold current and an improved stimulated emission. The injected electrons/holes are confined to a narrower region, meaning less current is needed for the population inversion. Carriers and optical confinement lead to a reduced threshold current density and less current heat. In a heterostructure laser, the active layer is surrounded by higher bandgap energy semiconductor; the higher the bandgap energy in a semiconductor, the lower the index of refraction [50, 51] Therefore, the change in the index of refraction defines an optical waveguide represented by the active region creating an oscillation media. The emitted photons will oscillate in the active region, which acts as an optical cavity, and the absorption loss is reduced [48, 52]

An optical cavity or an optical resonator is a must in a laser. The active region in a semiconductor acts as the optical cavity needed for the laser where light can oscillate and gets to lase. The oscillations provide a coherent radiation at the device output leading to a Fabry-Perot laser effect. The active region can be represented as a slab optical waveguide where light is confined in the active region and surrounded by layers of lower in index of refraction values. The Fabry-Perot effect is a result of these coherent oscillations, an internal multiple reflections within

the optical will occur. Once the device is cleaved, the sharp cleaved edges act as a partial mirrors reflecting optical light inside the active region, in some applications reflective materials are deposited on the facets to increase reflectivity The multiple coherent reflections results in the gain to be highest at the resonant frequency of the cavity and it amplify that frequency and it operates at a lower threshold current.

## 2.5 Impurity Free Vacancy Disordering (IFVD)/ Quantum Well Intermixing (QWI)

The industry has seen an increased number of optoelectronic devices that utilize quantum wells in their active regions.. Some devices require several QW bandgap configurations within the same structure which can be achieved via multiple MOCVD growth steps or several post growth fabrication steps such as QW etching. However, these techniques can be time consuming and expensive. There are other cost-effective and reliable methods of post growth QW bandgap configuration such as optical bandgap engineering are ion-implantation-enhanced inter-diffusion impurity-induced disordering (IID), laser induced disordering (LID) and Impurity free vacancy disordering (IFVD). IID introduce changes in the material resistivity and trap concentrations in addition to a questionable device lifetime performance. Whereas in IFVD, the material crystal retains its high quality and low optical propagation concentration. Moreover, IFVD is an inexpensive, reliable and highly reproducible process granted stable equipment. Eventually the QW material, structure and application dictates the desirable and preferable method.

IFVD is a process where a quantum well optical structure goes through a rapid thermal annealing (RTA) step resulting in an increase in the bandgap with an accompanying change in the refractive index [53]. During an RTA process the atoms diffuse in the quantum well region penetrating the interface causing the sub-band energies to move apart resulting in an increase in the n=1 electron to heavy-hole transition energy .IFVD allows for post growth optical badgap

configuration which is a desirable feature for the fabrication of integrated optical devices and low loss waveguides on a monolithic wafer as mentioned earlier [54-56]. Fig. 2-5 show the annealing process portrayed in a schematic manner.

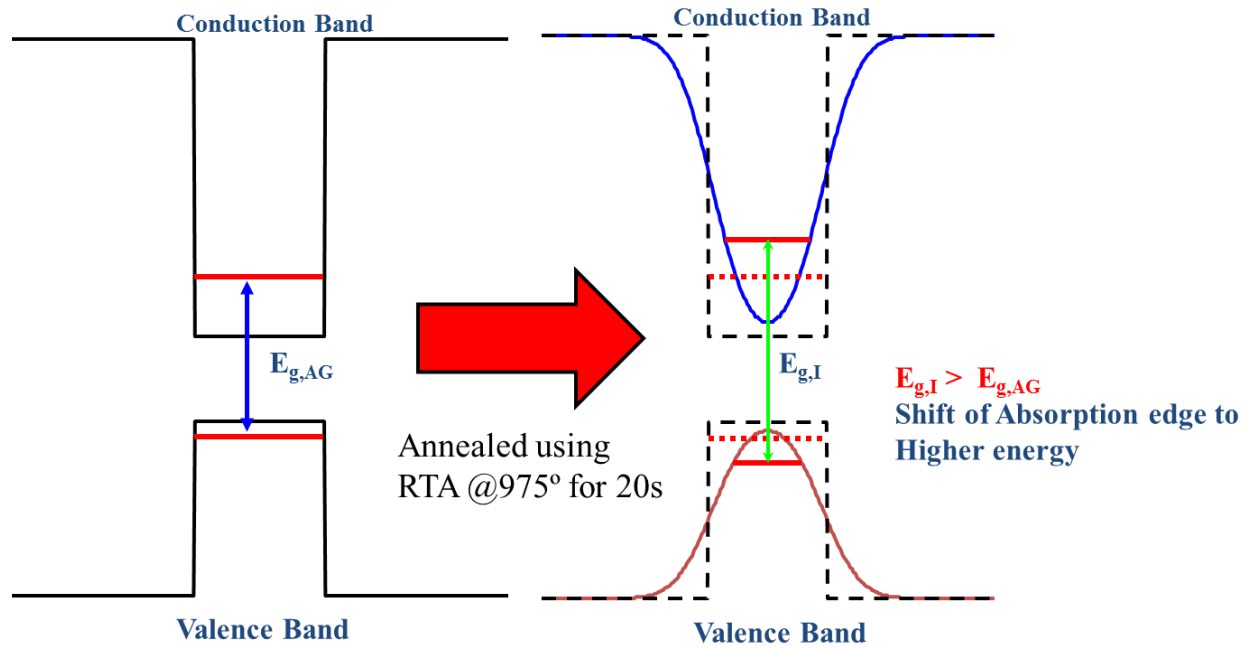


Figure 2-6 The shift in the absorption due to IFVD/QWI thermal annealing

Quantum Well Intermixing (QWI), is essentially the same method as of IFVD, with only one difference. In this work, we perform quantum well intermixing (QWI) that relies on a process of IFVD induced by a porous dielectric cap. A dielectric layer deposited on top of the quantum well structure, serves as a diffusion layer for the constituent atoms of the semiconductor. At high temperatures the Ga atoms from GaAs crystal, diffuse into the capping layer creating a large density of vacancies at the semiconductor-dielectric interface [53, 57-59]. These vacancies are quickly filled by other atoms in the semiconductor creating more vacancies in the layers next to the quantum well barrier. As the vacancies rapidly diffuse downward into the substrate they pass through the QW region. Thus, atoms diffuse into the quantum well modifying the shape of the

quantum well and the energy levels within. Area selectivity is accomplished by covering only specific areas with the dielectric cap and leaving other areas uncovered, since only the dielectric cap covered areas will undergo QWI. Selective area IFVD induced QWI processes are desirable techniques to produce devices with multiple regions of different bandgap energies on the same structure using a single RTA step[54, 60]. The degree of bandgap tuning depends on the material composition of wells and barriers in addition to the thickness of the wells. The degree of intermixing of the QW with the barrier, depends on the dielectric material type and porosity which can either promote or inhibit the atoms diffusion. We have found that the thickness of the dielectric material is also an important factor since it controls the number of vacancies generated the semiconductor allowing for more atoms to diffuse. In this work, SiO<sub>2</sub> film deposition is used as a capping dielectric layer for GaAs/AlGaAs quantum well structures since Ga has a high diffusion coefficient in the SiO<sub>2</sub> that is deposited in our laboratory. The dielectric-semiconductor diffusion interface can also be modified to either minimize or maximize diffusion by plasma exposure and surface modification.

## 2.6 Current Induced Guiding

In QW structures, the index of refraction value can be manipulated by electrical current injection [61-63]. When electrical current is injected into the QW, the electrons fill up the bottom of the eigen-level of the conduction band. Hence, the effective bandgap is increased and the absorption edge shifts toward higher energies. This change in the index of refraction is due to the band-filling (Burstein-Moss) effect theory. The index of refraction and absorption of a material can be expressed as a single value described by the complex index of refraction

$$\tilde{n} = n + ik \quad (2.6)$$

Where  $n$  is the index of refraction and  $k$  is the extinction coefficient and directly related to the absorption coefficient  $\alpha$ .

$$\alpha = \frac{2k\omega}{c} = \frac{2k}{\lambda} \quad (2.7)$$

Where  $\lambda$  is the free space wavelength of light and  $\omega$  is the angular frequency. Therefore, from Kramer's-Kronig's relationship

$$n(\omega) = 1 + \frac{1}{\pi} P \int_{-\infty}^{\infty} \frac{k(\omega')}{\omega - \omega'} d\omega' \quad (2.8)$$

At energies below the bandgap, the injected carriers into the semiconductor result in a decrease in the index of refraction. Furthermore, the refractive index of a semiconductor is affected by a high density of electrons and holes through the plasma effect. The change in the index of refraction can be calculated through

$$\Delta n = -\left(\frac{e^2 \lambda^2}{8\pi^2 c^2 \epsilon_0 n}\right) \left(\frac{N}{m_e} + \frac{P}{m_h}\right) \quad (2.9)$$

Where  $N$  is the electrons concentration,  $m_e$  is the electrons mobility,  $P$  is the holes concentration and  $m_h$  and  $m_e$  are the holes/electrons mobility. A typical optical waveguide consists of an area of high index of refraction surrounded by an area of a lesser value of index of refraction and light propagates in the area of high index of refraction. In our semiconductor heterostructure, the QW is region where the electron/hole recombination take place and it is in the middle of the active core layer with an index of refraction higher than the surrounding layers; therefore, light propagation is confined mostly in the active core of the QW layer. When light is launched into the QW it effectively spreads out into a slab mode that is only confined in the vertical direction. To eliminate light from spreading in the lateral directions, electrons and holes can be injected into a region to decrease the index of refraction and force light to move away from that region. Single mode optical waveguiding can be achieved by depositing two parallel metal contact

stripes on top of the area of interest of the QW structure. When current is injected through the metal stripes, electrons and holes are forced into the quantum well and they can only diffuse sideways across the QW creating two regions of smaller index of refraction value than the region in between where the electrons and holes have not reached. Thus light is confined and guided in the region that is surrounded by the regions overflowing with electrons and holes. Moreover, we can move or steer this optical channel to either way by increasing or decreasing the relative levels of the injected currents through either contact stripe.

Fig. 2-6 is schematic representation of the optical guiding and steering of light that can be realized in a semiconductor slab structure. As mentioned in the previous paragraph, when light is launched into a quantum well it spreads out in lateral directions. If we were to observe a near field image of the output facet for a propagating light in the slab waveguide, light would spread across the whole facet. By injecting current into the two stripes, we decrease the index of refraction beneath those areas and create an optical channel that confines light into a higher index of refraction area. Therefore, by changing the ratio of the injected currents we can optically move the channel from right to left and vice versa [64].

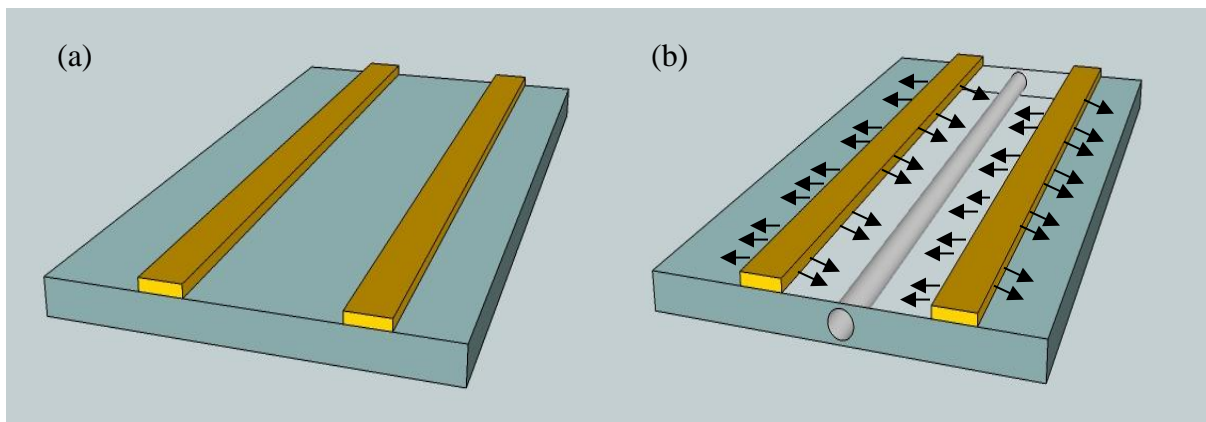


Figure 2-7 (a) Steering area with no current injected (b) Injected current effect forming a waveguide

## CHAPTER 3: ALL-OPTICAL PROGRESSIVELY INTERMIXED QW WAVEGUIDES

### 3.1 Introduction

Solid state tunable laser diodes are vital for environmental sensing applications such as atmospheric spectroscopy, chemical detection; moreover, they are also considered an important factor in medical diagnosis. Tunable laser sources can be a central tool in any optical test that requires spectral analysis. In addition, tunable laser diodes present an attractive solution to many challenges in optical communication networks that require complex multiplexing processes. Compact size and ease of fabrication is also key to the realization of optoelectronic integrated circuits with complex functionalities using conventional semiconductor technology. Moreover, optical switching, laser scanning, semiconductor lasers and optical beam steering are also industry desired functionalities needed for many types of sensing equipment including atmospheric and medical applications [19, 20, 65-67]. Micro-electromechanical systems (MEMS) such as cantilevers are electromechanically actuated optical beam steering devices. They consist of free space optical beams that can be directed to on-board optical devices or sensors [27, 68].

Current state-of-the-art in MEMS cantilevers requires an extensive and precise fabrication process and has limited operational capabilities. Another method that serves the same purpose is micro-lens optical steering. The micro-lens is placed on a movable stage and the beam is steered using electro-thermal actuators, which also requires extensive fabrication process and offers a limited steering range [69] while suffering from slow actuation speed. As an alternative to the mechanical means, carrier-induced beam steering in a post-growth multiple quantum well (MQW) structure is proposed as a solid state mechanism for optical beam steering. This

mechanism relies on the change in index of refraction resulting from current injection in semiconductor heterostructures [61, 64].

It has been shown in previous works that such steering mechanism can be used to produce a continuously controlled motion of an optical beam [54]. It is envisaged that a device can be conceived to produce tunable laser operation by combining the concept of optical beam-steering section together with multiple optical gain regions achieved through area-selective disordering of multiple quantum well structure as shown in Fig 3-1. The disordering method used in this work is impurity-free vacancy diffusion (IFVD). This technique offers a cost effective, area selective and highly reproducible method of realizing different optical bandgaps on one single substrate. The areas that are designated to be intermixed are capped with  $\text{SiO}_2$  film and the sample is annealed at a sufficiently elevated temperature for a very short time.

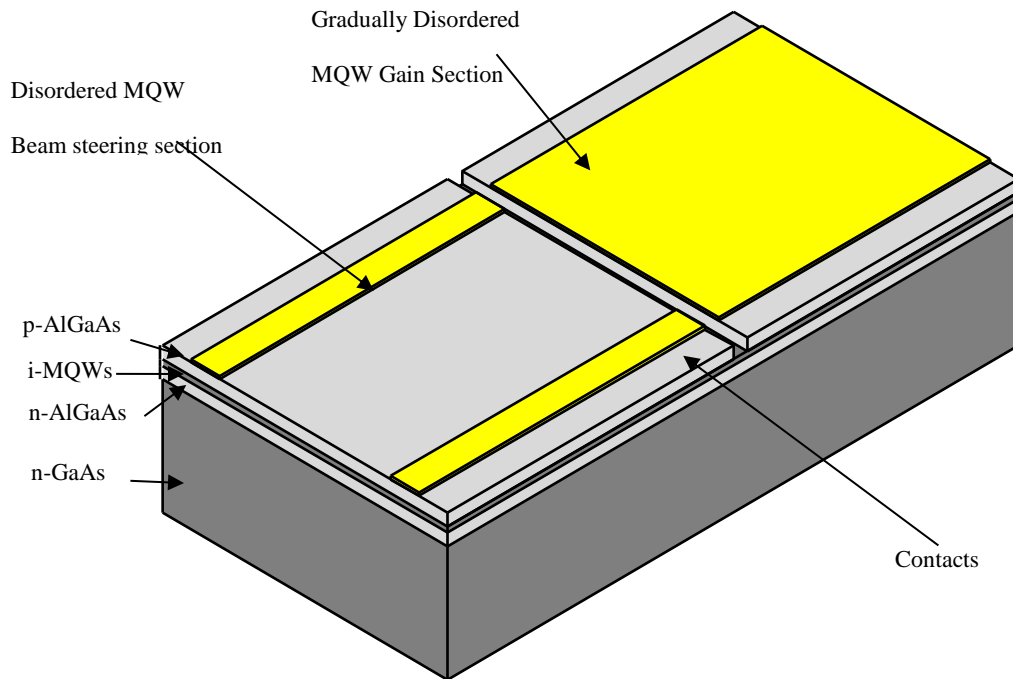


Figure 3-1 Proposed System overview showing the test device. The input waveguides lead light into the steering beam section where the progressively disordered area is surrounded by metal contacts with different spacing



Different degrees of MQW intermixing can be achieved by employing different SiO<sub>2</sub> film thicknesses followed by a single rapid thermal annealing. These intermixed MQWs can effectively serve as optical gain media with different gain spectra. There are other techniques that are widely used for producing tunable lasers, with the most successful ones being the sampled grating Distributed Bragg Reflector (DBR) laser [70-74]. Temperature tuning of a laser diode is also a very commonly used technique [75].

In this work, we demonstrate that we can controllably alter the wavelength corresponding to the peak of the gain spectrum by a blue shift of between 10nm and 60nm as compared to the as-grown device using a single rapid thermal annealing for the MQW disordering. The MQW disordering is a result of the deposited SiO<sub>2</sub> capping film on top of the MQW structure which upon rapid thermal annealing, promotes the diffusion of Ga into that cap resulting in vacancies being formed in the semiconductor structure immediately below the surface. Also during the rapid thermal annealing, the vacancies are driven toward the substrate, they pass through the MQW structure randomly exchanging lattice sites with Ga and Al especially at the quantum well to barrier interfaces. The inter-diffusion between the Ga and Al atoms at the interface between the GaAs quantum well and the AlGaAs barriers results in a gentle grading of the confining potential energy barrier which in turn gives rise to an increase in the eigen energy levels of the confined electrons and an equivalent decrease in the eigen level for holes thereby leading to an effective band gap increase [58]. Although not directly applicable in this work, it has been found that depending on the MQW structure and the deposited capping material, either an enhancement or a suppression of the shifting of the emission peak has been detected in photoluminescence (PL) studies of the disordering of MQW structures. Moreover, it has also been reported that

plasma exposure of the uncapped semiconductor surface can also limit the creation of vacancies and reduce the degree of unintentional intermixing of the uncapped regions of the MQW [76-78].

### 3.2 Device Design and Simulations

For this work, an initial prototype device is fabricated to determine the feasibility of the proposed device and to obtain preliminary results and conduct observations. A schematic overview is shown in Fig. 3-2. The test device that consists of two sections, is fabricated on a GaAs/AlGaAs MQW p-i-n hetrostructure on a GaAs substrate. The first section is the mode launching section which consists of 1 mm long, 4  $\mu\text{m}$  wide waveguides formed by etching away the most of the top cladding material. In these waveguides, the quantum well has been disordered progressively by different amounts using the procedure described earlier [54].

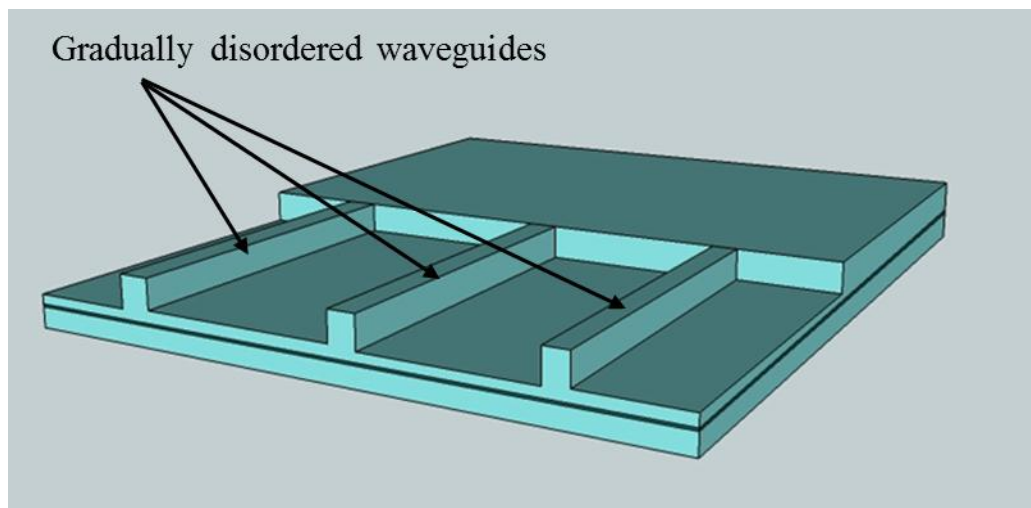


Figure 3-2 System overview showing the fabricated test device

### 3.3 Device Fabrication

The choice of materials for the proposed device was based on the optical and electrical properties and ease of fabrication. AlGaAs MQW p-i-n structure was chosen for the test device and the final proposed device. The AlGaAs MQW structure used consists of a 1  $\mu\text{m}$  thick AlGaAs lower cladding layer that is grown by MOCVD on a n-doped substrate. That layer is followed by 40

pairs of alternating GaAs wells and AlGaAs barriers each 10 nm thick and a 500 nm thick AlGaAs top cladding layer. The structure is finally capped with a 20 nm GaAs layer..

### 3.3.1 Mask Design and fabrication

First, the soda lime chrome plated mask is cleaned with methanol and isopropyl alcohol using a spinner and then, it is baked at 115° C for 1 min. Shipley 1805 photoresist is dispensed over the mask using a 1 micron filter then the mask is spun at intervals with gradually increasing speeds up to 3000 rpm for 30s for each interval. The mask is then baked in an oven for 30 min with the temperature set at 105° C. The mask pattern is written using the NEOS Laser Photo-Plotter to transfer the design to the mask using laser exposure power of 35μW at a wavelength of 442nm. The mask is then developed using a 1:7 mixture of Microposit 351 developer: water for ~50 sec. A post-bake step of 120° C for 5 min using a hotplate is performed. The uncovered chromium is then etched off in a diluted solution of Cr etchant:water in a ratio of 1:3 for between 2 – 2.5 min. After the chromium has been etched, the mask is immersed in acetone for a few seconds and then wiped dry with lens cleaning paper. It is again rinsed with methanol, followed by isopropanol, and DI water and then thoroughly dried. A final cleaning process is performed by immersing the mask in piranha etch a mixture of sulfuric acid and H<sub>2</sub>O<sub>2</sub> to remove any possible organic contaminants.

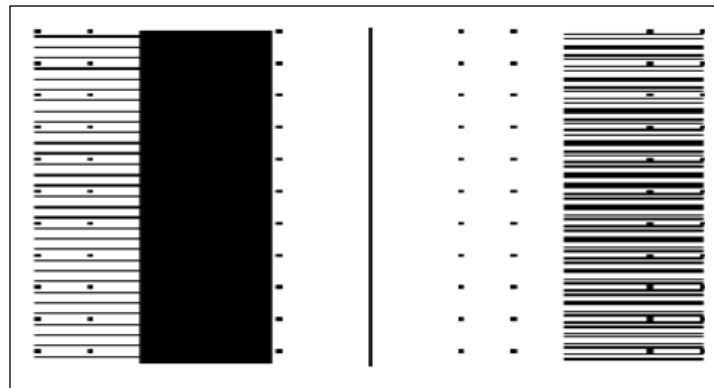


Figure 3-3 Fabricated masks showing waveguides and disordered areas

That mask is used for creating the waveguides, the intermixed regions and the metal contacts designs; Fig. 3-3 shows the mask design for the waveguides and steering contacts.

The second step of the mask making involves the creation of the reversal image of the original mask. We again start by cleaning a new chrome plated mask with alcohols and baking at 115°C for 1 min as described above. Then Futurrex PR NR7-500P negative photoresist is spun in a similar incrementally increasing speed up to 3000 rpm for 30s for each interval. The mask is then baked in an oven at 105° C for 30 min. The mask is then placed on the chuck of an MJB-3 mask aligner and the first mask is contact aligned to the so that chrome side of both mask are facing each other. The pattern designs is transferred onto the new mask by exposing it to UV light (350-400nm) for 5s at 12 mW/cm<sup>2</sup>. After that, the mask is baked for 30 min in the oven set at 105° C. After cooling down to room temperature the photoresist is developed in RD6 developer for 20 to 24 sec. A post-bake is performed at 150° C for 10 min using a hotplate to harden the photoresist. The chromium is then etched for approximately 2.5 to 3 min using the diluted chromium etchant 1 part etchant: 3 parts water. The photoresist is then removed by soaking in acetone and the mask is cleaned using the same procedure as for the first mask.

### 3.3.2 SiO<sub>2</sub> film deposition

The fabrication process for the sample starts with the plasma enhanced chemical vapor deposition (PECVD) of a SiO<sub>2</sub> layer using a Plasmatherm 790 machine. A specific recipe is programmed in which the substrate is placed on a stage inside the chamber, and the stage is heated to 250°C. Once the set temperature has been reached, the pressure of the chamber is regulated to 1050 mTorr while the gases SiH<sub>4</sub> and NO<sub>2</sub> are introduced in the deposition chamber at the precise flow rates of 401sccm and 826sccm respectively while an RF power of 24 W and a DC bias of 7V maintains a constant plasma glow discharge for 10:00 min. To achieve the

progressively SiO<sub>2</sub> film deposition over the sample, a cleaved GaAs piece is placed on top of the sample in the chamber. The GaAs piece covers only half of the sample and exposes the rest for film deposition. By introducing this piece on top of the sample, the SiO<sub>2</sub> can no longer be deposited evenly over the exposed area. This result in a thicker SiO<sub>2</sub> film deposition close to the covered edge and a thinner SiO<sub>2</sub> film as it moves away toward the edge of the sample. The picture in Fig. 3-4 shows a picture of the sample with a progressive thickness of the SiO<sub>2</sub> film, where darker color represents the thick SiO<sub>2</sub> film. Hence, the lower region (B) has the thickest film which was measured to have ~475nm of SiO<sub>2</sub>. The middle region (M) has the thinnest film measured at ~20nm of SiO<sub>2</sub> and the upper region (T) has a ~250nm SiO<sub>2</sub> thick. The film thickness distribution is not controllable over the sample. The GaAs piece that was placed on top of the sample disturbs the flow of the gases resulting in this film thickness distribution.

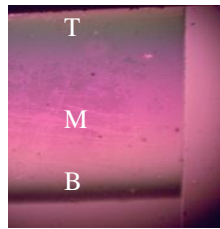


Figure 3-4 graded sample and an inset of the graded SiO<sub>2</sub> film

### 3.3.3 Rapid thermal annealing

After the SiO<sub>2</sub> deposition, a rapid thermal annealing (RTA) step at 975°C for 20s is performed in an AG Associates Heat pulse 210T under a constant flow of nitrogen gas flow of 5sccm. During the RTA, the sample is sandwiched between two GaAs wafers to provide an arsenic over-pressure that helps limit the loss of arsenic from the sample.

### 3.3.4 Photolithography

After the SiO<sub>2</sub> has been removed by etching in a solution of buffered oxide etch (BOE) consisting of pH balanced diluted hydrofluoric acid, the sample is coated by spinning Shipley

1805 positive photoresist @4000rpm for 40s followed by a baking step @105°C for 4:00. The sample is placed on the chuck of an MJB-3 mask aligner and the first mask containing the waveguide patterns is contact aligned with the sample. Then the photoresist is exposed for 5s to UV light through the mask pattern. After developing the sample in a 10:1 mixture of DI water and Microposit 351 developer, it undergoes a hard bake step at 100°C for 1min to harden the photoresist for the wet etching step.

### 3.3.5 Wet etching

The waveguides were then delineated by etching off the unwanted GaAs and AlGaAs using a mixture of  $H_3PO_4:H_2O_2:H_2O$  (1:2:30). The etching is carried out to form the ridge waveguides until the remaining cladding thickness on either side of the ridge is only 160nm. The resist is then stripped using acetone and sample is cleaned using the solvent cleaning process described above.. The steps involved in the waveguides fabrication process are outlined in Fig. 3-5.

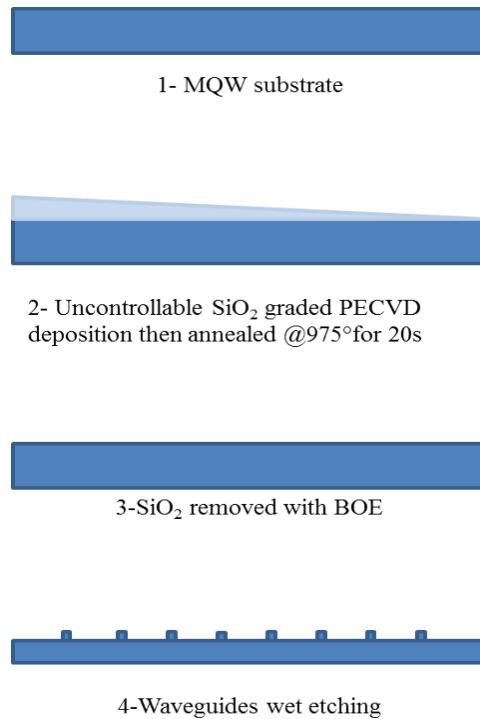


Figure 3-5 Fabrication process steps

### 3.4 Testing and Results

The degree of disordering was measured by comparing the room temperature photoluminescence (PL) spectra for several samples that were prepared differently for this part of the testing. The first sample was simply the as-grown sample. Each of the second batch of samples consisted of an uncapped region and a region coated with varying thicknesses of SiO<sub>2</sub> film that range from 25 to 350nm in 25nm increments. Finally, a third sample of a progressively deposited SiO<sub>2</sub> layer ranging from 0-475nm. To obtain the photoluminescence spectra, the samples were pumped by a 10mW Ti-Sapphire laser beam operating at a wavelength of 742nm. The laser beam was focused and launched into one port of a 2x2 50/50 optical fiber coupler and the PL emission was collected by the same fiber coupler and the spectrum was monitored using an Ando optical spectrum analyzer (OSA) as shown in Fig. 3-6.

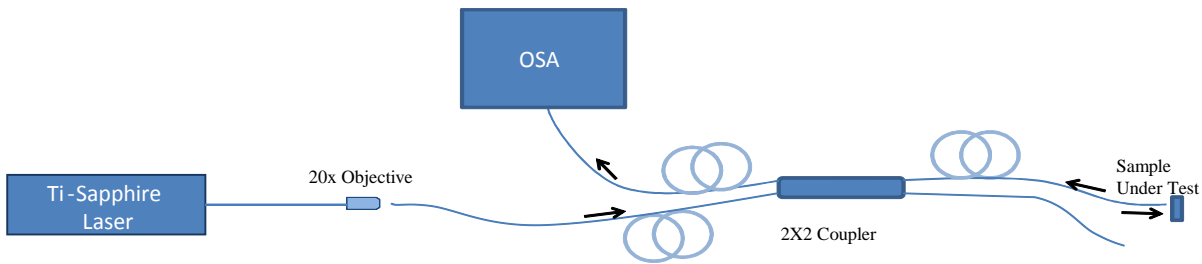


Figure 3-6 Photoluminescence set-up

The optical characterization was performed at room temperature for the following three samples: an as-grown sample, an annealed uncapped sample, and annealed samples with a range of 25 to 350nm of silicon dioxide film. The PL measurements indicate that the MQW intermixing using this method results in a controlled blue shift of the effective band edge of the coated samples in the range of 10 to 60 nm compared to a shift of 10nm for the PL of the uncoated samples.

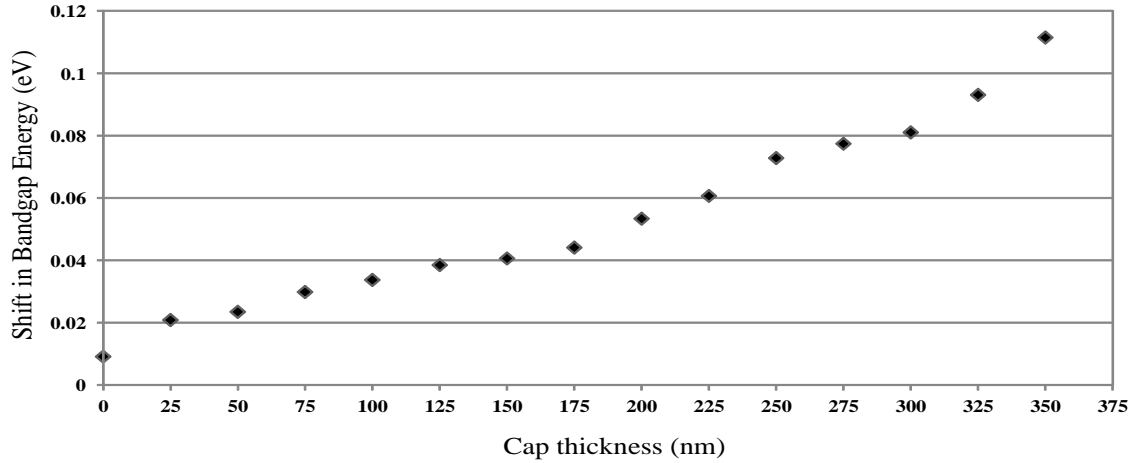


Figure 3-7 Change in bandgap energy compared to as grown sample for different cap thicknesses

Fig. 3-6 shows the measured bandgap energy change of the SiO<sub>2</sub> coated samples with respect to the bandgap energy of the as-grown sample. Fig. 3-7 shows the photoluminescence spectra of several SiO<sub>2</sub> capped samples at room temperature. The SiO<sub>2</sub> cap thickness in this case was progressively deposited SiO<sub>2</sub> film thickness distribution as explained in 3.3.2 across the MQW substrate which had a deposited film ranged of 0 to 475 nm over a distance of about 4mm as mentioned in section 3.3.2.

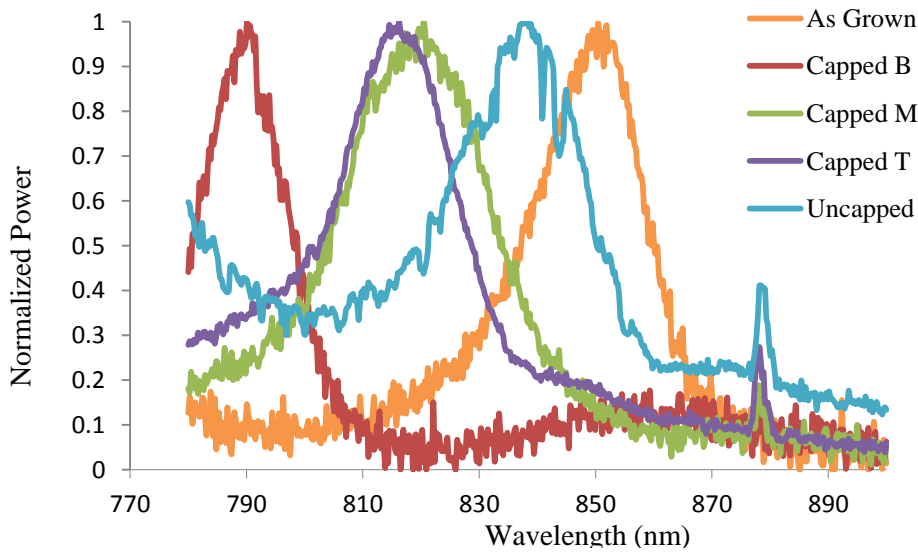


Figure 3-8 Photoluminescence peaks of the graded sample and an inset of the graded SiO<sub>2</sub> film



The degree of the blue shift can be clearly observed depend on the thickness of the deposited SiO<sub>2</sub> film, with a thicker the film resulting in a larger bandgap shift. From the PL spectra of fig. 3-7 for the sample shown in fig 4-3, it is obvious that the (B) region covered with ~475nm of SiO<sub>2</sub> experiences the largest change in bandgap energy. Moreover, these photoluminescence measurements demonstrate that lateral extent to which the degree of disordering can be confined as evidence by the distinct PL peaks that are captured within a small area (~20µm).

The device under test is cleaved and mounted on a copper plate. We tested the waveguides that have been fabricated in the progressively disordered MQW region, with each waveguide being disorder in incremental steps. The waveguides have been investigated using a tunable Ti:sapphire laser as the light source to probe their transmission characteristics. The waveguides are aligned in an end-fire optical setup shown in Fig. 3-8, using 40x microscope objective lenses to excite the waveguide mode and to collect the transmitted power onto a photodetector that is LABVIEW interfaced

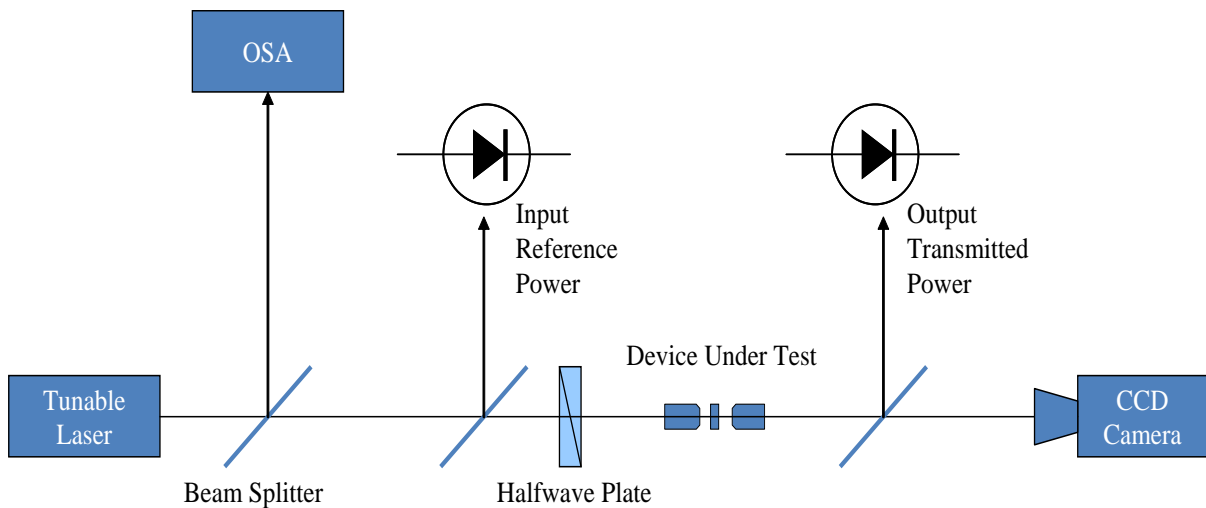


Figure 3-9 Labview controlled optical setup for measurements of the waveguide transmission characteristics

The output beam from each waveguide under measurement is also imaged onto a CCD camera. A labview program is designed to capture the transmission spectra of the selectively disordered waveguides by measuring the signals from the photodetector while scanning the wavelength of the laser. Fig. 3-9 shows plots of the transmission spectra of five of the waveguides that were intermixed to varying degrees. The spectra indicate that the waveguides fabricated in the regions that had the thickest SiO<sub>2</sub> film can transmit the shortest wavelength laser light. This is confirmation that the measured MQW waveguides each has progressively increasing bandgap energies.

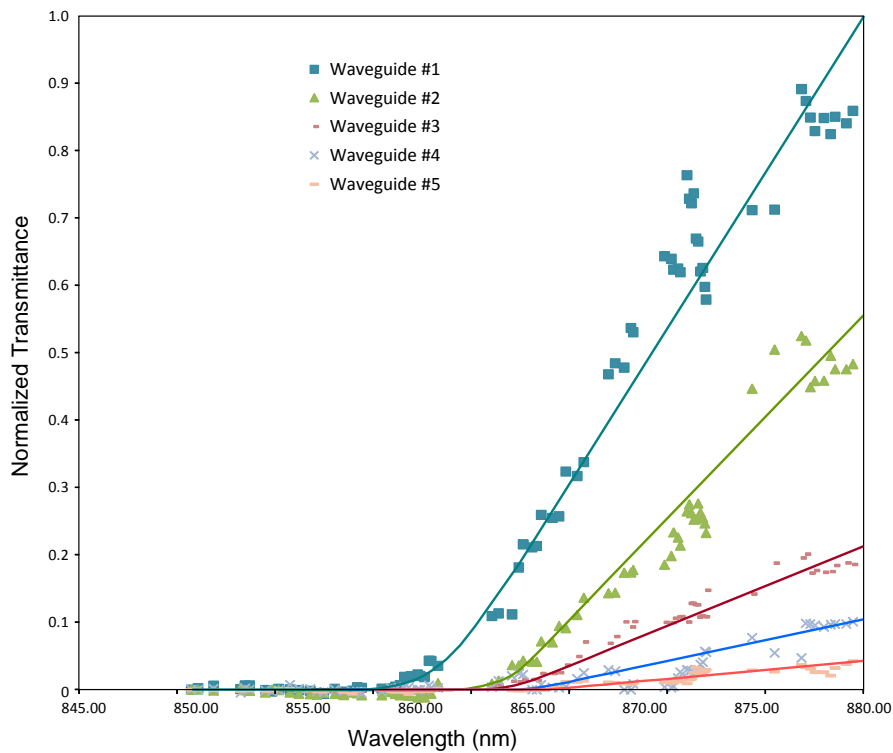


Figure 3-10 Transmission spectra of the progressively disordered waveguides

# CHAPTER 4: BEAM STEERING OVER SELECTIVELY INTERMIXED REGIONS

## 4.1 Introduction

In our previous work we investigated the absorption property of the proposed device QW structure. We have demonstrated that a highly intermixed region will have less absorption at shorter wavelengths than the unintermixed or lightly intermixed regions. Based on those results, we designed a beam steering device as a progression of that work. Steering devices over a QW region have been demonstrated before [20, 79]; however, for our device concept we need to demonstrate that the same steering mechanism can be applied to multiple selectively intermixed regions. Therefore, in this section we show the ability of the device to confine and laterally steer an optical beam over two differently intermixed regions.

The device demonstrates optical beam steering on a GaAs/AlGaAs QW graded-index, separate confinement heterostructure, single-quantum-well (GRIN-SCH-SQW) that is suitable for laser diode operation, by utilizing a combined impurity free-vacancy disordering and carrier-induced optical waveguiding and beam-steering techniques. The device consists of a single mode waveguide section that leads to a slab beam steering section. The slab contains two neighboring selectively intermixed QW regions each  $10\mu\text{m}$  wide bounded by two contact stripes. The spatially controlled current-induced refractive index change creates an optical waveguide channel that confines the optical beam and by controlling the electrical currents applied to each contact stripe, the optical beam is able to be steered laterally over the two selectively intermixed regions. The QW structure is first characterized for the degree of intermixing that can be achieved with different thicknesses of dielectric caps and then the device is fabricated and experimentally investigated [80].

#### 4.2 Principle of Operation for the Proposed Tunable Laser Device

The proposed device is a tunable quantum (QW) laser diode that operates by forming and steering an optical beam into an optical amplifier section that contains a disordered QW with different degrees of intermixing. The device consists of a beam-steering section and an intermixed optical amplifier section. Unlike previous devices where the optical beam is steered over an as grown QW structure [64, 69], in this work the optical beam is steered over selectively intermixed regions. The bandgap energies of the selectively intermixed regions are blue shifted by amounts that depend on the thickness of a SiO<sub>2</sub> capping film. The SiO<sub>2</sub> film promotes the diffusion of Ga into that cap resulting in vacancies that migrate very quickly through the QW structure during rapid thermal annealing [54] thereby inducing intermixing of the constituent atoms from the well and barrier materials. The beam steering section confines and steers an optical beam laterally by applying electrical currents to two parallel contact stripes as shown in Fig.4-1. The active core of the gain section is divided into adjacent regions in which the quantum well has been selectively intermixed to varying extents. When current is injected into the gain region, photons are produced spontaneously forming an optical beam that propagates in the core of the device. To control and confine the path of the optical beam, electrical currents are applied to the metal contacts of the steering region. As a result of the current injections, the electrons gather in the QW layer below the parallel contact stripes. When the injected electrons fill the regions below the stripes they diffuse sideways and the stretches occupied by the electrons experience a reduction in the refractive index. Hence, an optical channel is created in the region where there is a smaller concentration of electrons (high refractive index) surrounded by the regions of large electron concentration (low refractive index). The guided optical beam can be electrically steered in between the two parallel stripes by regulating the relative levels of the two injected currents. As the optical beam is steered over the selected gain region, its photons that

have energies that correspond to the peak in the gain spectrum determined by the degree of disordering of the QW experiences the most amplification and therefore after multiple roundtrips laser emission is obtained and the wavelength of the laser is determined by the beam-steered position.

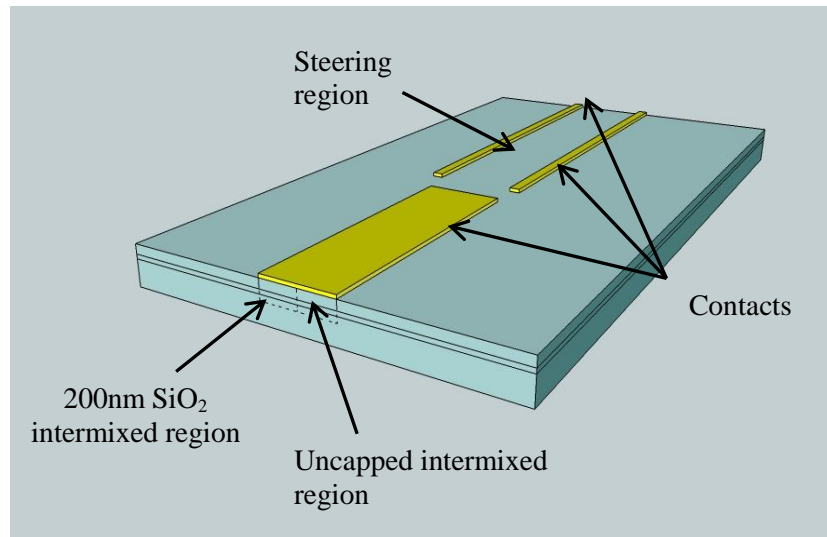


Figure 4-1 Proposed Device

### 4.3 Device Design

To demonstrate the concept of the proposed device shown in Fig 4-1, we have fabricated a simpler device in which an optical beam can be steered laterally over area-selectively intermixed regions of a QW structure. To reduce complexity in the proposed device, the gain section of the device was eliminated and replaced with a single mode waveguide to simulate the locally generated optical amplification by the gain section in the proposed device. The input waveguide is  $2\mu\text{m}$  wide and  $1.4\mu\text{m}$  high and guides an end-file coupled laser beam into the middle of the intermixed beam steering section where the mode expands into a slab mode. The beam steering section is a slab waveguide that consists of two regions intermixed using different  $\text{SiO}_2$  thicknesses and is bounded by a  $1\text{mm}$  long and  $10\mu\text{m}$  wide parallel metal contact stripe on either

side. The intermixed regions have been selectively blue shifted as a result of rapid thermal annealing of the sample with different SiO<sub>2</sub> capping film thicknesses. The choice of GaAs/AlGaAs QW p-i-n material for the proposed device is based on a well proven design for a simple to fabricate laser diode employing the GRIN-SCH-SQW structure. The wafer's active region consists of a single 4nm wide GaAs quantum well sandwiched between two 5nm wide Al<sub>0.25</sub>Ga<sub>0.75</sub>As barrier layers. These layers are surrounded by AlGaAs layers each 150nm wide, where the concentration of aluminum is gradually increased from Al<sub>0.25</sub>Ga<sub>0.75</sub>As to Al<sub>0.55</sub>Ga<sub>0.45</sub>As. Those layers are further sandwiched by Al<sub>0.55</sub>Ga<sub>0.45</sub>As upper and lower cladding layers that are each 1.2μm wide. The top of the wafer is capped off by a 50nm transition layer followed by 150nm GaAs layer. Two different devices with contact separations of 20 and 30μm were designed and fabricated. These gaps of either 20μm or 30μm constitute the beam steering sections of the device and each are sub-divided equally into either two 10μm or two 15μm wide regions. Mathematical simulations using a beam propagation code have been used to determine the waveguide dimensions for the device schematic shown in Fig.4-2.

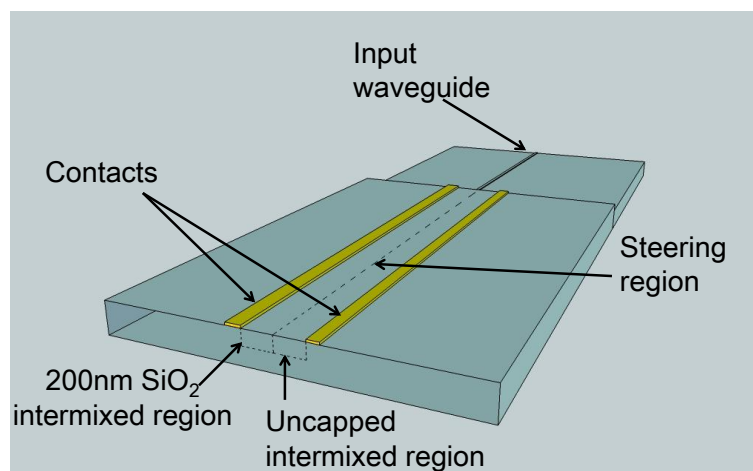


Figure 4-2 Fabricated Device

#### 4.4 Device Fabrication

A computer aided design (CAD) software was used to implement the design of the optical beam steering device, and the design was input to an in-house NEOS laser plotter that produced five photo-lithographic masks to be used in the fabrication of the device. The fabrication process is shown in Fig. 4-3.



1- Chrome evaporation (alignment marks)



2- SiO<sub>2</sub> PECVD deposition (400nm)



3- Selective RIE etching (400nm, 200nm, uncapped) mthen annealed @975° for 20s



4- SiO<sub>2</sub> is removed and waveguides are wet etched



Figure 4-3 Fabricated Device

#### 4.4.1 Mask design and fabrication

The same process mentioned in chapter three is repeated to create the masks required to fabricate the steering device. Five masks are designed and fabricated to realize the steering device. The first mask contains only alignment marks that are transferred to the semiconductor sample and serves as fiduciary marks for all the stages of the device fabrication. The second mask has the design patterns to define the waveguides and the areas to be disordered. The third and fourth masks are used create the two selectively intermixed regions over the steering section. The fifth mask contains the features for delineating the contacts that are on the sides of the steering section. Fig. 4-4 shows the contacts mask and a close up of the waveguides masks with different steering area widths.

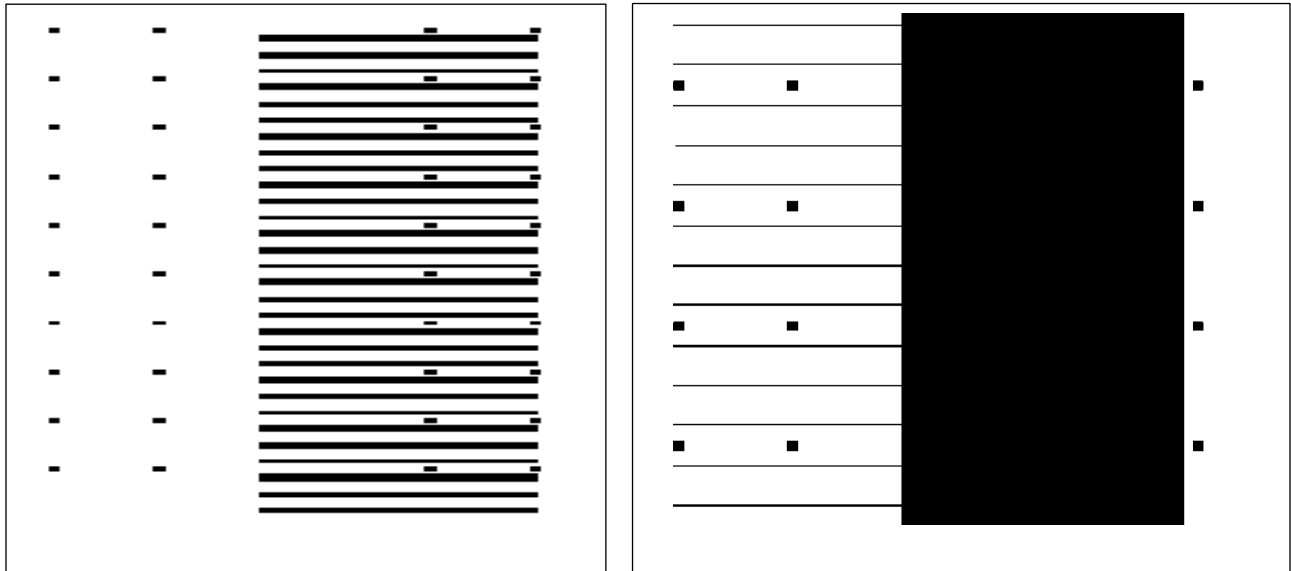


Figure 4-4 Fabricated Device

#### 4.4.2 Metal evaporation

The device fabrication starts with the creation of chromium alignment marks by photolithography, vacuum evaporation of the metal and the “lift-off” technique. These alignment marks which are repeated throughout all the set of masks serve as fiduciary markers for each of the photolithographic steps employed in the fabrication of the device. The sample with the



photoresist containing the pattern of alignment marks is placed in an Edwards Auto306 thermal evaporator and some chromium metal is placed in a tungsten boat inside the chamber. The chamber is pumped down to  $5 \times 10^{-1}$  Torr by a mechanical pump followed by a cryopump that creates a vacuum with a residual pressure of  $\sim 2 \times 10^{-6}$  Torr. Electrical current is applied to the tungsten boat and gradually increased to  $\sim 3.3$ A and the mechanical shutter is opened allowing the chromium vapor to coat the sample. A crystal monitor measures the thickness of the deposited layer of metal and the current is adjusted until the deposition rate is around 1nm/s. When a total thickness of 100nm of chromium has been deposited, the shutter is closed and the current is gradually reduced to zero. After the evaporation boat has cooled down to near room temperature, the chamber is vented with nitrogen and the sample is removed.

The sample is soaked in a beaker of acetone until the photoresist dissolves and lifts off the unwanted chromium metal leaving alignment marks on the sample. The sample is thoroughly cleaned with acetone followed by isopropyl alcohol and de-ionized water and is ready for the next step in fabrication process.

#### 4.4.3 SiO<sub>2</sub> film deposition

A 400nm thick layer of SiO<sub>2</sub> is deposited on the top surface of the sample using a Plasmatherm 790 PECVD machine as described in chapter 3.3.2.

#### 4.4.4 Photolithography

The sample is coated with a 1 $\mu$ m thick layer of NR7-1000PY photoresist by spinning at 4000 rpm for 40s. The photoresist is then baked at 150°C for 1 min. The photoresist is exposed to UV light through mask #2 containing the 20 $\mu$ m wide rectangular blocks using the mask aligner. The photoresist is post-baked at a temperature of 100°C for 1 min. and developed in RD6 developer

to open 20 $\mu$ m wide windows in the photoresist in the areas that will become the beam-steering sections.

#### 4.4.5 Reactive Ion Etching (RIE)

The sample is placed in the etching chamber of the Plasmatherm 790 machine and a programmed recipe is used to etch the uncovered SiO<sub>2</sub> layer by reactive ion etching. The chamber pressure is set to 40mTorr while CF<sub>4</sub> gas is introduced at a controlled rate of 45sccm. A plasma is struck using an RF power of 175W with a DC bias of 345V for 6.33 min to etch off 200nm of the SiO<sub>2</sub> in the exposed areas. At this point, the sample is still completely covered with SiO<sub>2</sub> however, the regions that are designated to become the beam-steering areas, are covered with only 200nm of SiO<sub>2</sub>.

#### 4.4.6 Repeat of 4.4.4 and 4.4.5

The sample is re-cleaned and spin-coated with negative photoresist again and baked at 150°C. The second half of mask #3 is used in the mask aligner so that after developing, half of each of the previously etched 20 $\mu$ m wide windows are opened. The sample is again loaded in the reactive ion etcher and processed until the SiO<sub>2</sub> is completely etched off in the 10 $\mu$ m wide windows. Consequently after this step, we have a beam-steering area consisting of two 10 $\mu$ m wide adjoining regions one covered with 200nm thick SiO<sub>2</sub> and the other completely uncovered. The remainder of the device is still covered with a 400nm thick SiO<sub>2</sub> layer.

#### 4.4.7 Rapid Thermal Annealing (RTA)

The sample is then annealed at 975°C for 20s. The all the areas that have been covered by 400nm thick SiO<sub>2</sub> including the waveguide section are intermixed to the extreme, and therefore the quantum well waveguides have the least absorption coefficient as described in the previous

chapter. The selectively intermixing of gain section regions creates two optical bandgaps as seen Fig. 4-5. The SiO<sub>2</sub> is then completely removed via BOE.

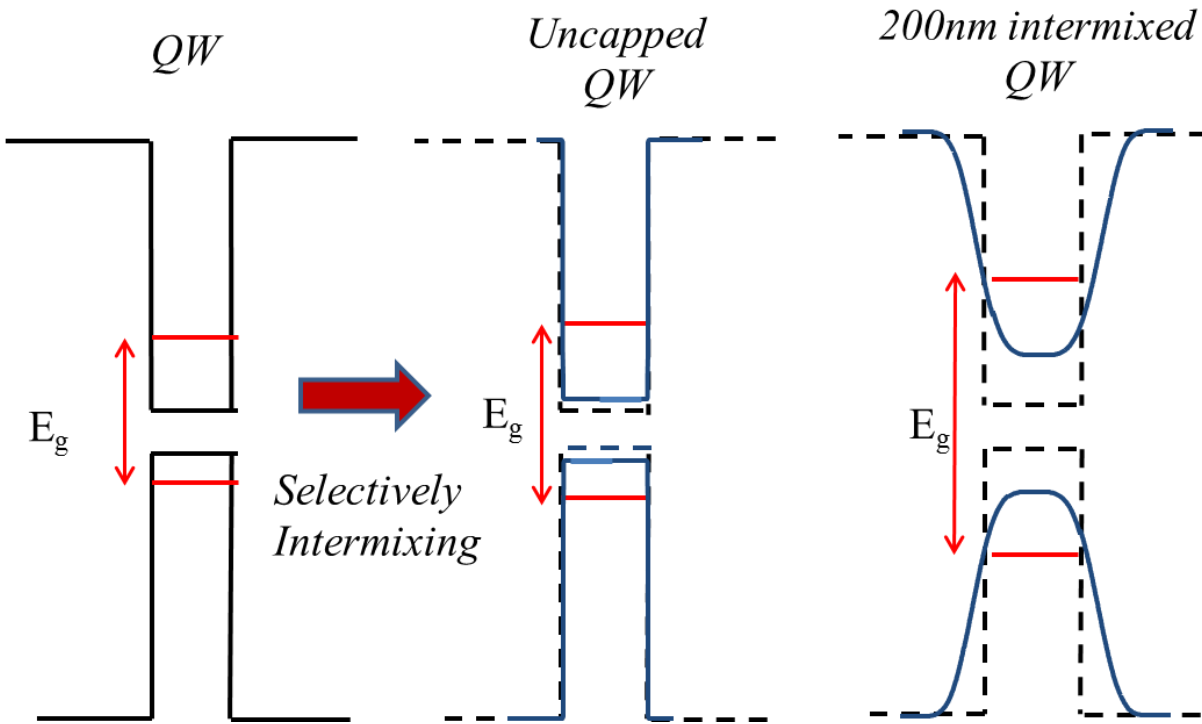


Figure 4-5 Selectively intermixed regions of the steering section

#### 4.4.8 Wet Etching

Positive photoresist Shipley's 1805 is then spun on the sample and exposed using mask #4 leaving only the contacts areas covered. The device is etched in a solution of H<sub>3</sub>PO<sub>4</sub>:H<sub>2</sub>O<sub>2</sub>:H<sub>2</sub>O (1:2:30) for 1.5min to remove 150nm of the capping layer over the steering section. The sample is re-cleaned and re-coated with Shipley 1805 positive photoresist and exposed to UV light from the MJB-3 mask aligner through the fourth mask to define the single mode waveguide ridges. After developing the photoresist in a 10:1 water to Microposit 351 developer for 12s, the uncovered areas are etched by a mixture of H<sub>3</sub>PO<sub>4</sub>:H<sub>2</sub>O<sub>2</sub>:H<sub>2</sub>O (1:2:30) to delineate the waveguides that are 1.4μm high by 4μm wide.

#### 4.4.9 P-type contacts deposition

The sample is cleaned and re-coated with negative photoresist and baked at 150°C once again. Mask #5 is used to delineate two thin parallel stripes followed by a post bake 1min step at 100°C. After the photoresist is developed for 7s in RD6, the two stripe windows are opened in the photoresist that still covers the rest of the sample. The sample is placed in the Edwards Auto306 thermal evaporator and the p-type contact metals are evaporated in three steps. The thermal evaporator is equipped with a rotational stage that allows us to evaporate a maximum of four different metals without the need to open the chamber after each evaporation step. The chamber is pumped down as discussed previously in section 4.4.2. First titanium (Ti) is evaporated at a current of ~3.2A to a thickness of 7nm. This is followed by a 20nm thick zinc (Zn) layer that is evaporated at a current of ~1.65A and finally these metals are topped off with a 300nm thick gold (Au) layer by passing a current of ~0.7A through the boat. The “lift-off” process is performed by dissolving the photoresist in acetone thereby removing all the unwanted metal layers except where the contacts are desired.

#### 4.4.10 Sample polishing

The sample is mounted on a chuck using crystal bond wax and thinned down by manually lapping the back side of the substrate to a 150µm thickness using 5µm diameter aluminum oxide powder mixed with DI water on a glass plate. The sample is then polished using a South Bay Technology model 920 lapping and polishing machine. The machine has a variable speed lapping wheel and a nozzle controlling the flow of DI water. The wheel speed is set at dial 2 and Buehler micropolish II powder with a grit size of 0.3µm is applied with the least water flow possible. The sample is left on the lapping wheel for 3min or until that surface becomes shiny

smooth. It is then soaked in a beaker of acetone to dissolve the wax and detach the sample from the polishing chuck.

#### 4.4.11 Repeat of 4.4.9

The sample is cleaned once more with acetone and alcohols and attached to a glass slide top-side down using a very small amount of photoresist and baked at 90°C to solidify the resist. The sample is then placed in the thermal evaporator chamber. Just as for the p-type contact, three metals are used for the n-type contact. First a 4nm layer of nickel (Ni) is evaporated at a current of ~3.1A followed by a 20nm layer of germanium (Ge) at a current of ~2.8A and topped off by 200nm of gold (Au) evaporated at a current of ~0.7A.

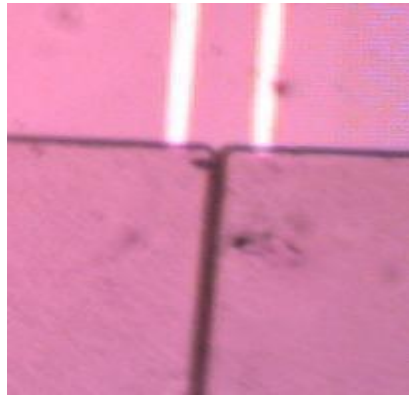


Figure 4-6 Fabricated device

### 4.5 Testing and Results

The device is cleaved to a total length of about 1.8 mm and mounted on a copper plate using a conductive adhesive made by Epoxy Technology. Fig.4-6 shows a photograph of the fabricated device that has a contact separation of 20µm. The degree of bandgap change as a result of annealing at 975°C for 20s with different SiO<sub>2</sub> capping films is characterized using electroluminescence measurements. The results shown in Fig.4-7 indicate that the peak of the luminescence spectrum which is at 805nm for the as-grown sample, is shifted to 799nm for the

un-capped sample, 779nm for the sample with a 200nm thick SiO<sub>2</sub> and 774nm for the sample capped with a 400nm thick SiO<sub>2</sub> film.

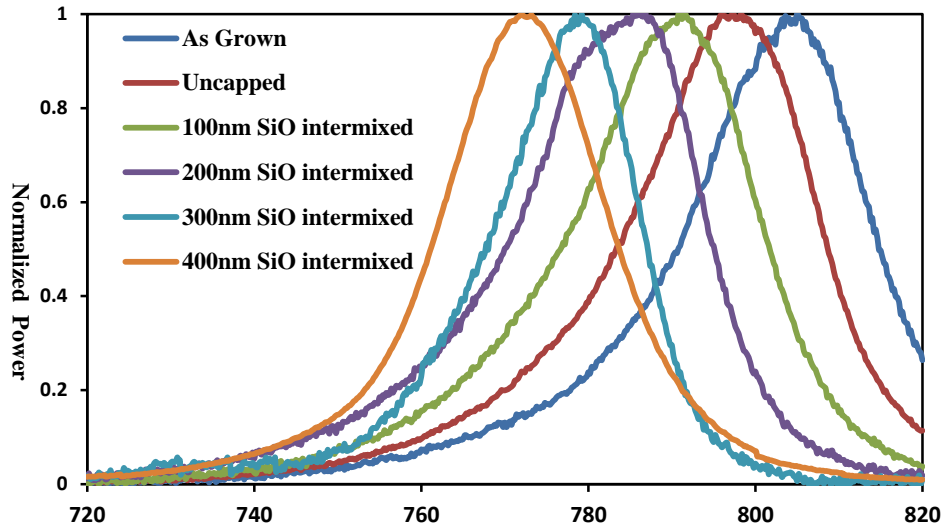


Figure 4-7 Electroluminescence spectra of samples intermixed using different thicknesses of SiO<sub>2</sub>

The devices are investigated using TE polarized light from a tunable Ti:sapphire laser set at 850nm and launched into the waveguide by end fire coupling using a 40x microscope objective lens. Two separate current drivers are used to inject currents to the beam-steering contact stripes via micropositioner probes. For the beam-steering experiment, an RG850 filter which blocks all light with a wavelength less than 850nm was placed at the output to block the electroluminescence from the carriers injected through the steering contacts. The output is collected by a spectrometer connected to a Labview program to digitally capture the output spectrum. Simultaneously, the output is monitored by a CCD camera that is connected to a digital frame grabber the experimental set-up Fig.4-8.

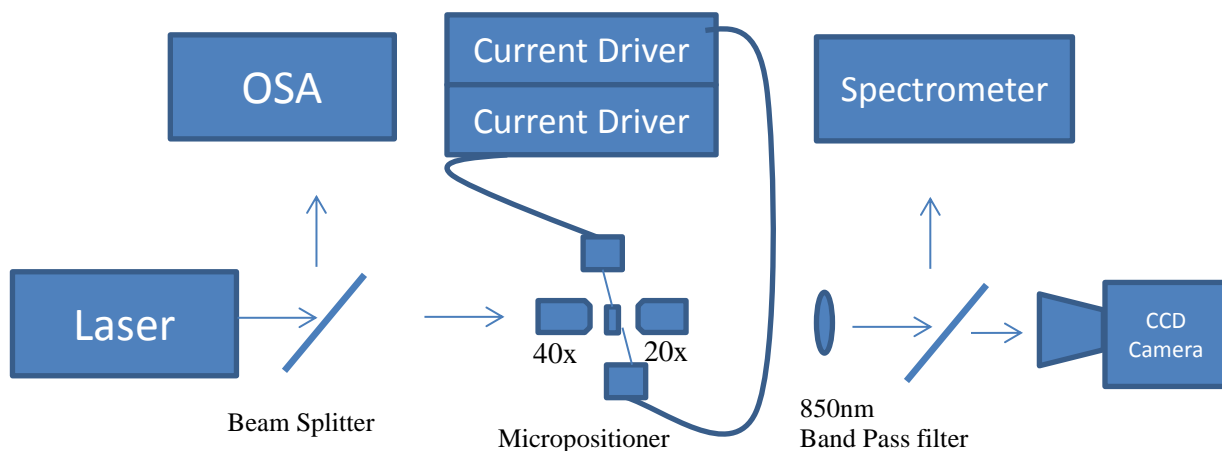


Figure 4-8 Experimental set-up

A top view of the two parallel contacts surrounding the two selectively intermixed regions is shown in Fig 4-9.

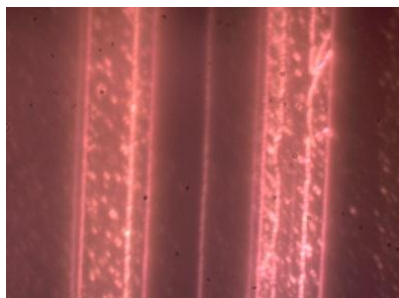


Figure 4-9 A close up picture showing two selectively intermixed regions bounded by contacts

To determine the position of those contacts on the CCD camera screen, current is applied separately to each of the contacts and the electroluminescence emission is captured by the camera with the RG850 filter removed as shown in Fig.4-10 (b, c). When no electrical current is applied to the contacts, the light that is launched in the single mode waveguide propagates to the beam-steering section then diverges into the slab mode in that section as shown in Fig. 4-10(a).

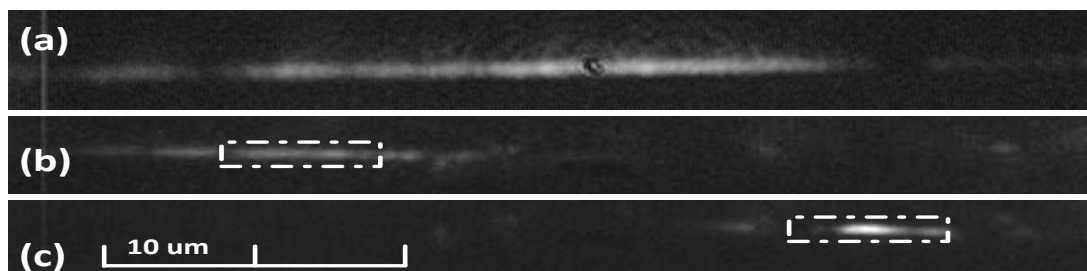


Figure 4-10 Electroluminescence and laser beam output

Fig.4-11 shows the spectra of the different optical beams at the output facet of the device. The electroluminescence peaks of each contact correspond to the respective peaks of the adjacent intermixed region. The areas beneath the stripes are intermixed with 400nm thick SiO<sub>2</sub> but these regions do not emit light in a wavelength that corresponds to the 400nm SiO<sub>2</sub> intermixed QW because the injected electrons leak into the lower energy levels of the adjacent less disordered regions. Therefore, each contact emits a wavelength that corresponds to its adjacent intermixed region. The variations in the power intensity of launched laser beam at 850nm in Fig 4-11 is due to the beam shifting position. As current is applied, the sample heats up and the output loses focus on the spectrometer resulting in an intensity change.

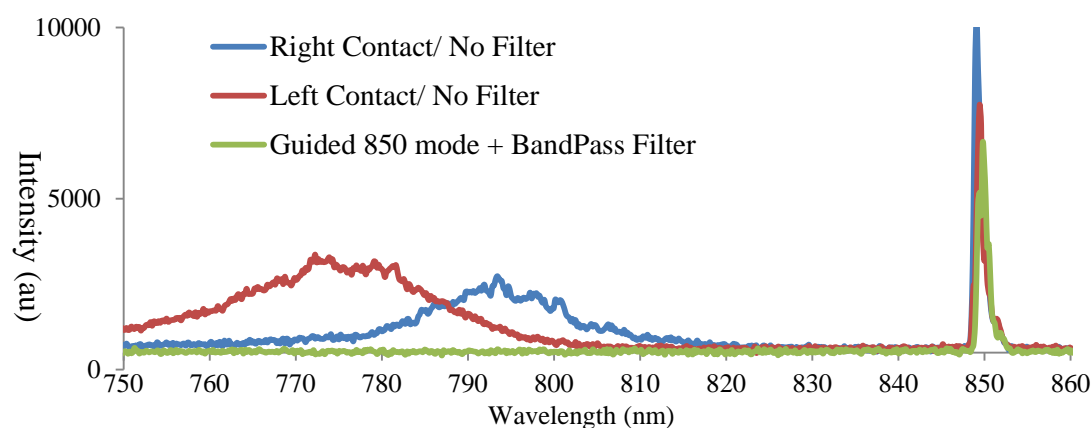


Figure 4-11 Electroluminescence and laser beam output

Optical mode confinement and lateral beam steering is clearly observed as current is injected into the two stripes of the device with the 20μm gap. With no or low currents applied through the



contacts the optical mode diverges into a slab mode until at the output the whole slab area between the two stripes is illuminated as shown in Fig. 4-10a. However, as currents values are slowly increased (up to 150mA), a guided-mode spot is clearly seen (Fig. 4-11). By changing the values of the injected currents, we are able to steer the output spot laterally. The output spot is pushed away from the contact stripe with the higher injected current due to the decrease in the index of refraction in that area. With equal current injections through the contacts the output spot settles in the middle of the facet.. Fig.4-12 shows the steering sequence from the output facet of the device with 20 $\mu$ m gap between the contacts as different currents are injected into the two metal stripes.

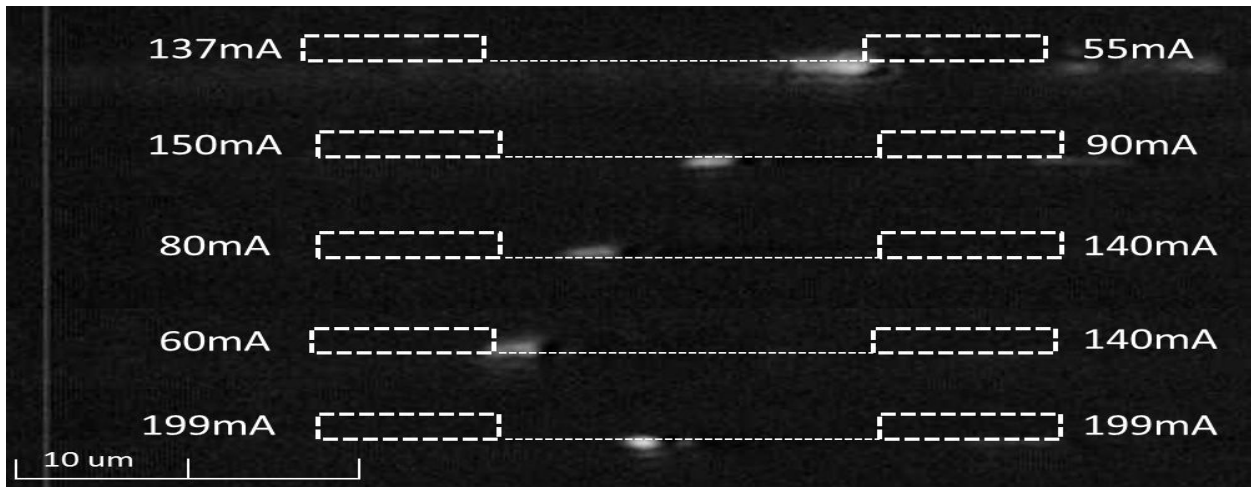


Figure 4-12 steering sequence

#### 4.6 Conclusion

A beam steering device over selectively intermixed GaAs/AlGaAs QW laser structure has been experimentally investigated in order to demonstrate the concept of a tunable laser based on beam steering. This section confirms the ability to steer a launched laser beam over two selectively intermixed regions by controlling the levels of currents injected in the two parallel contacts surrounding the steering area. The fabricated device has two sections, a waveguide section and a

selectively intermixed beam steering section. We have simulated the waveguide section of the device to optimize the optimal dimensions. The beam steering section was divided into two regions that were selectively intermixed to different extents. Based on the electroluminescence tests, the QW structure showed the ability to tune the peak of the optical gain spectrum by up to 20nm using intermixing induced by SiO<sub>2</sub> dielectric cap annealing. First, current was injected into the two contacts to determine the steering range and it was noticed that the spectrum peaks of each contact correspond to the respective peaks of the adjacent intermixed region. We were able to steer the beam over the two intermixed regions; however, the relative current levels that are needed to steer the waveguide spots to either extreme are not reciprocal. It is believed that this is due to the unequal accumulation rate of electrons in the two selectively intermixed regions of the steering section. We also believe that thermal effect due to high currents values limited the mode shape and size.

## CHAPTER 5: SELECTIVELY INTERMIXED MQW TUNABLE LASER

### 5.1 Introduction

In the two previous chapters we divided the realization of the monolithically integrated tunable laser in stages. First, we characterized the absorption property of the QW structure subjected to different conditions of intermixing. In our second experiment, we demonstrated the device's ability to steer and confine an optical beam over two differently intermixed QW regions. In this chapter, we fabricated the integrated device which demonstrates a tunable laser that utilizes optical beam steering over a gain section which has adjacent regions of different optical bandgaps. As the optical beam is steered over the selected region, it experiences a gain spectrum with a position of the peak that is determined by the degree of intermixing of the QW and that sets the lasing wavelength [81].

The concept of the device relies on the fact that an optical beam that experiences stimulated amplification and feedback in an intermixed region will have the lasing wavelength corresponding to the peak the gain spectrum of that intermixed region. Current-induced waveguiding technique has shown the ability to confine and steer an optical beam over a certain range [64, 69]. In this chapter, we demonstrate two monolithically integrated tunable laser designs with 10nm and 17nm wavelength tuning range respectively. Wavelength selection is achieved by confining and steering the generated optical beam laterally over two adjacent quantum well regions that selectively intermixed to different extents.

## 5.2 Device Design

The devices consist of a beam-steering section and an optical amplifier gain section as shown in Fig. 5-1 and 5-2. The beam steering section consists of two parallel 1mm long stripes separated by a 20 $\mu\text{m}$  wide gap. An optical beam is confined and laterally steered by applying electrical currents to the parallel contact stripes. The active gain section is cleaved to range in between 250 and 750 $\mu\text{m}$ . The active region, which is 20 $\mu\text{m}$  wide, is divided into adjacent regions in which the quantum well has been selectively intermixed to unequal extents [82] using different SiO<sub>2</sub> thicknesses during the rapid thermal annealing. In one design, the gain section is divided into two adjacent regions and in the second design it is divided into three contiguous regions where the bandgap energies of the selectively intermixed regions are altered by amounts that depend on the thickness of a SiO<sub>2</sub> capping film of each region.

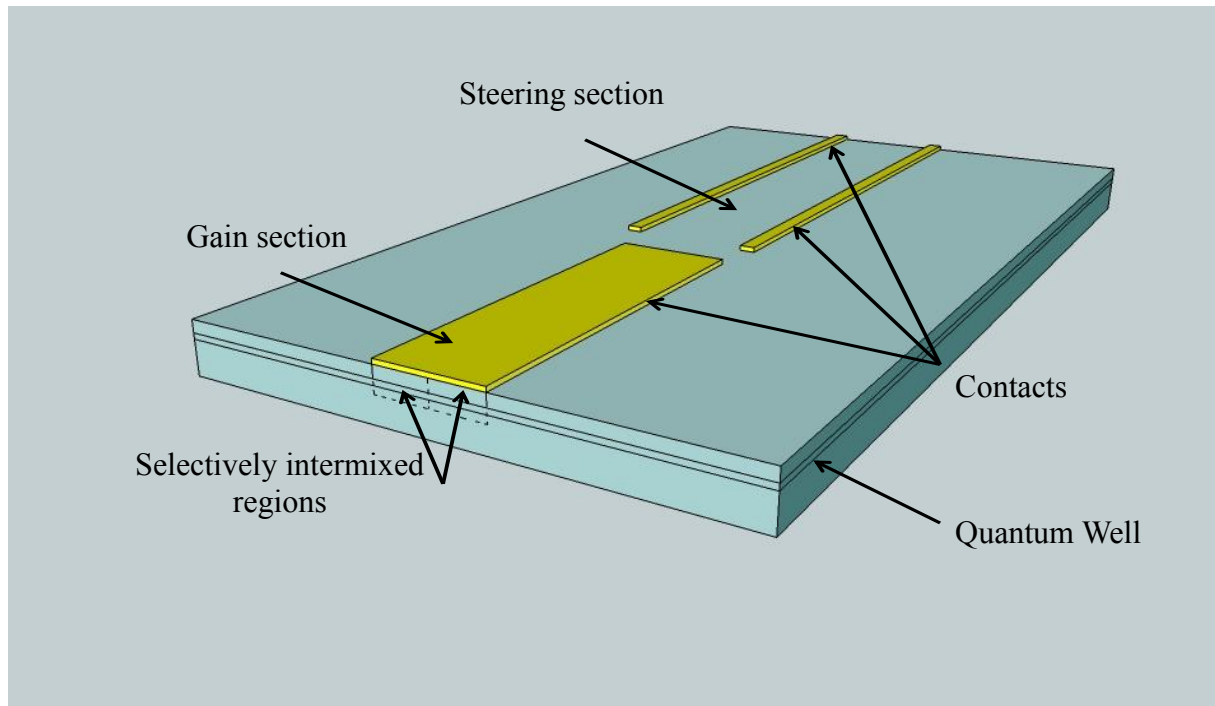


Figure 5-1 Schematic drawing of the first device design

The remainder of the device is intermixed to the maximum to minimize the absorption coefficient of the slab waveguide.

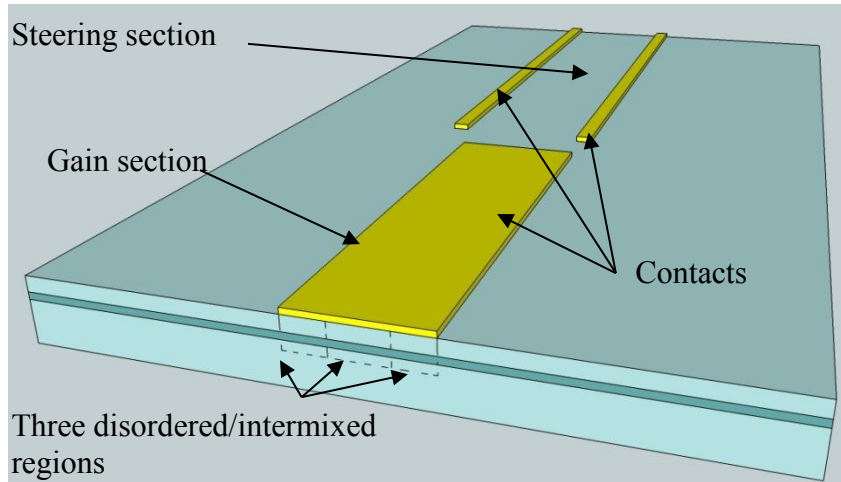


Figure 5-2 Schematic drawing of the second device design

### 5.3 Fabrication

The same GaAs/AlGaAs QW p-i-n structure as in the previous chapter is chosen for the fabrication of the laser device since this work is a continuation of the previous beam-steering device.

#### 5.3.1 Mask design and fabrication

The same process mentioned in chapter 3.3.1 is repeated to create the masks required to fabricate the tunable laser device. Four masks are designed and fabricated to realize the first laser device and an additional fifth mask is needed to create the second laser device. For both devices, a mask that contains the alignment marks is first created. Then two masks one containing 20 $\mu\text{m}$  wide rectangular blocks and the other containing 10 $\mu\text{m}$  wide blocks are created to produce the two 10 $\mu\text{m}$  wide selectively intermixed regions of the first laser device. For the other laser device, three masks are created containing rectangular blocks of width 20 $\mu\text{m}$ , 14 $\mu\text{m}$  and to define the

three distinct selectively intermixed regions of the gain section. Finally, a mask contains the contacts for the gain section and the steering section is designed and fabricated. Fig. 5-3 shows the contacts mask for the laser devices. The devices were designed in such a manner that we can choose the length of the gain section and the beam-steering section independently during the cleaving of the device.

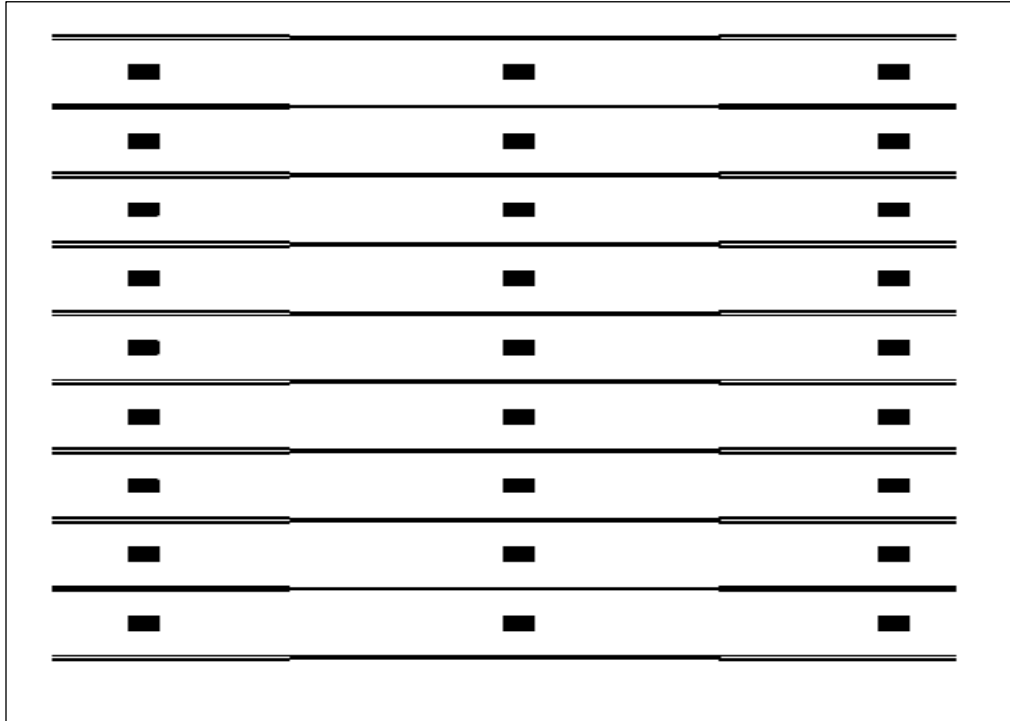


Figure 5-3 Schematic drawing of the second device design

### 5.3.2 Metal evaporation

The first step in the device fabrication of both devices is to delineate the alignment marks on the samples by photolithography, metal evaporation and “lift-off” as described in chapter 4.4.2.

### 5.3.3 SiO<sub>2</sub> film deposition

The samples are then cleaned with acetone and alcohols and placed in the Plasmatherm 790 PECVD machine to deposit a 400nm thick layer of SiO<sub>2</sub> on the top surface using the same recipe as described in chapter 3.3.2.

#### 5.3.4 Photolithography

Negative photoresist NR7-1000PY is spun at 4000rpm for 40s and the samples are baked at 150°C for 1min. Mask #2 is then used to create the 20 $\mu$ m wide windows for the gain section. This step is the same for both devices. The photoresist is exposed for 5s, post-baked at 100°C for 1min and then developed for 7s.

#### 5.3.5 Reactive Ion Etching (RIE)

The samples are then placed in the RIE chamber of the Plasmatherm 790 and the exposed SiO<sub>2</sub> in the 20 $\mu$ m wide photoresist windows is etched using the same process and recipe as described in chapter 4.4.5.

#### 5.3.6 Repeat of 5.3.4 and 5.3.5

The samples are cleaned again and NR7-1000PY photoresist is spun on the surface. The photoresist is exposed using the mask aligner and developed using the same parameters mentioned in 5.3.2. In this step, mask #3 is used to define the two unequally intermixed regions of the gain section. 10 $\mu$ m wide windows are opened in the photoresist film above the 20 $\mu$ m wide gain region with the window spanning between the middle and one edge of that gain region. The SiO<sub>2</sub> layer in that opened window is etched off completely by RIE leaving the samples each with a 20 $\mu$ m wide etched rectangles in the SiO<sub>2</sub> film. For one of the samples, each of the rectangles consists of a 10 $\mu$ m wide region with a 200nm thick layer of SiO<sub>2</sub> and another 10 $\mu$ m wide region with no SiO<sub>2</sub> film. Whereas as for the other sample with the device that consists of three differently intermixed regions, a different mask #3 is used to create 14 $\mu$ m wide windows within each of the rectangles in the SiO<sub>2</sub> film such that the rectangles are divided into two sections that are 6 $\mu$ m wide and 14 $\mu$ m wide respectively. After the RIE, the thickness of the SiO<sub>2</sub> film in the

rectangles that are 14 $\mu\text{m}$  wide is 100nm while there is no  $\text{SiO}_2$  film in the rectangles that are 6 $\mu\text{m}$  wide.

#### 5.3.7 Repeat of 5.3.6 for the sample with three intermixed regions only

The sample with the three intermixed regions is once more coated with NR7-1000PY photoresist and baked at 150°C for 1min. Then, mask #4 is used to create the third and last 6 $\mu\text{m}$  wide rectangles in the 14 $\mu\text{m}$  wide section of the gain region that is covered with 200nm of  $\text{SiO}_2$ . After the third RIE, we have a sample in which the 20 $\mu\text{m}$  gain sections are divided into three regions of 6 $\mu\text{m}$ , 7 $\mu\text{m}$  and 6 $\mu\text{m}$  covered with 200nm, 100nm of  $\text{SiO}_2$  no  $\text{SiO}_2$  film respectively.

#### 5.3.8 Rapid Thermal Annealing (RTA)

Both samples are cleaned and then annealed at 975°C for 20s. The areas covered with a 400nm thick film of  $\text{SiO}_2$  during the RTA, which include the whole device except for the gain section, will experience the smallest absorption coefficient at wavelengths close to the bandgap energy of the QW, as was shown in our previous work [68]. The gain sections that have been annealed with different thicknesses of  $\text{SiO}_2$  during the RTA are selectively intermixed by dissimilar amounts and each of the gain sections is subdivided into two regions of different optical bandgaps for the first sample and into three regions of different optical bandgaps for the second sample as shown in Fig. 5-4. The  $\text{SiO}_2$  is then completely removed via BOE.



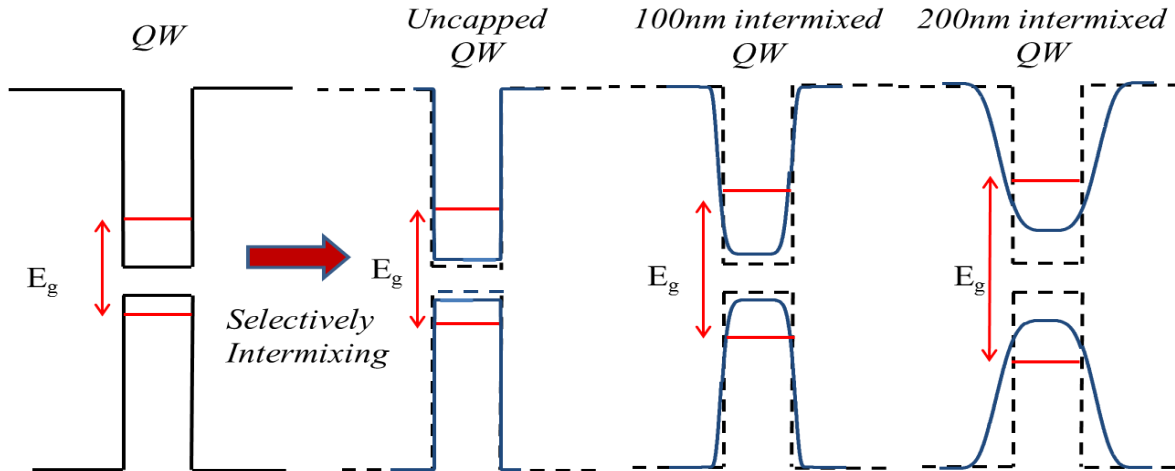


Figure 5-4 Three selectively intermixed regions

### 5.3.9 Wet Etching

Positive photoresist Shipley's 1805 is then spun on the samples and processed leaving only the contacts areas covered. The device is then wet etched in  $\text{H}_3\text{PO}_4:\text{H}_2\text{O}_2:\text{H}_2\text{O}$  (1:2:30) mixture for 1:30min to remove capping over the steering section.

### 5.3.10 P-type contacts deposition

Using the chromium alignment marks that were defined in the first step, the final lithography step is performed to delineate the two narrow (~10 $\mu\text{m}$  wide) parallel stripes around the beam-steering section and a 20 $\mu\text{m}$  wide stripe on the surface of the gain section by evaporation of the p-contact metals and the "lift-off" process as described in chapter 4.4.9.

### 5.3.11 Sample Polishing

The substrates sides of the samples are lapped down to a thickness of 150 $\mu\text{m}$  and polished until mirror smooth using the mechanical polisher as described in chapter 4.4.10.

### 5.3.12 N-type contacts deposition

The samples are attached to a glass slide and n-type contact metals are deposited on the polished substrate by vacuum evaporation described in chapter 4.4.11

## 5.4 Testing and Results

Electro-luminescence characterization of individual samples with different SiO<sub>2</sub> thick film was performed in chapter 4.5 figure 4.7 and based on those results we assessed the degree of bandgap change required for our devices. Therefore, we chose combination of uncapped and 200nm of SiO<sub>2</sub> intermixed regions for gain section in the two region laser. However, for the three region laser we chose an uncapped, 100nm and 200nm of SiO<sub>2</sub> intermixed regions for the gain section.

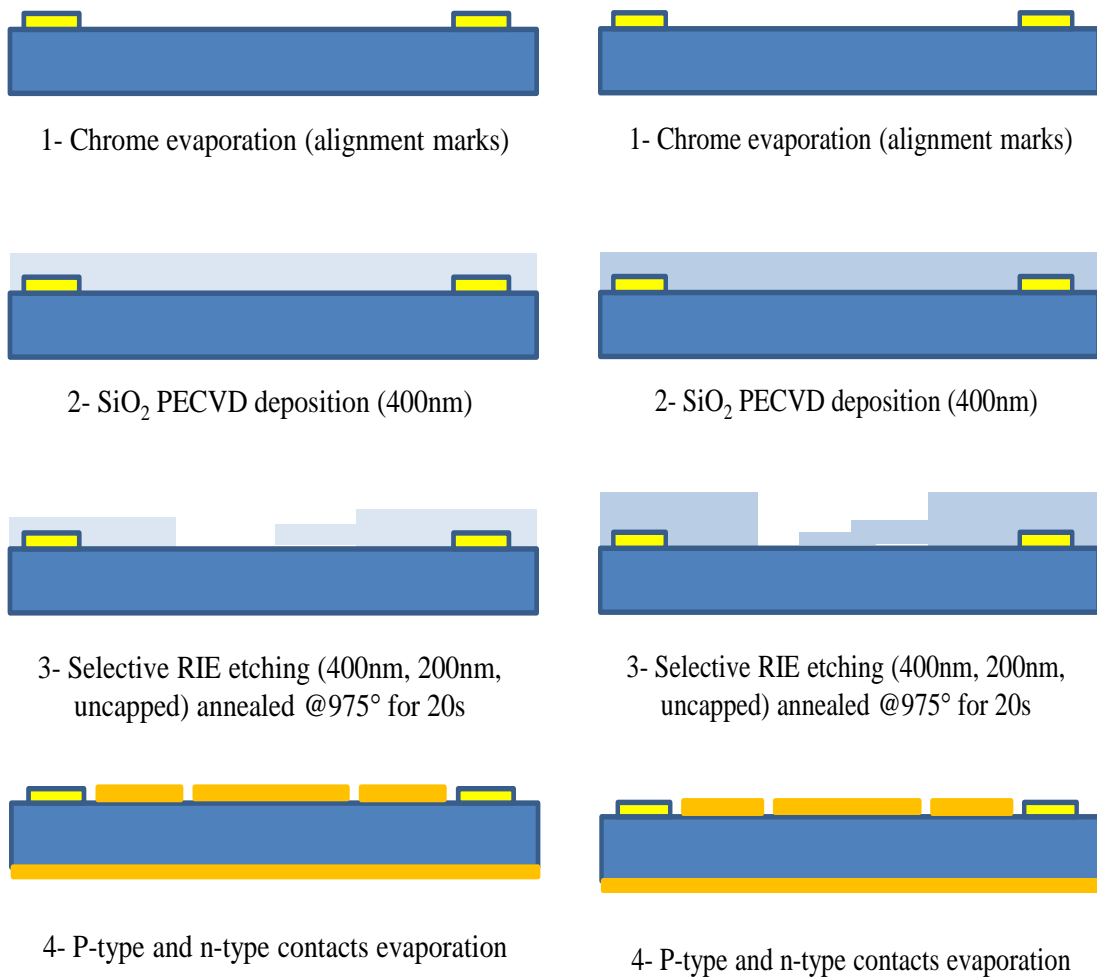


Figure 5-5 Schematic drawings of the fabrication steps for both devices

The operation of the device is investigated using three separate current drivers to inject pulsed currents to the contact stripes via micropositioner probes. Each current driver is individually

controlled using an electrical circuit that was designed to deliver pulsed electrical current to each probe independently. The circuit has three transistors each powered by a 12v D.C. power source and controlled by a common pulse generator using three separate rheostats, connected to the base of each of the transistors. The circuit design is shown in Fig 5-6.

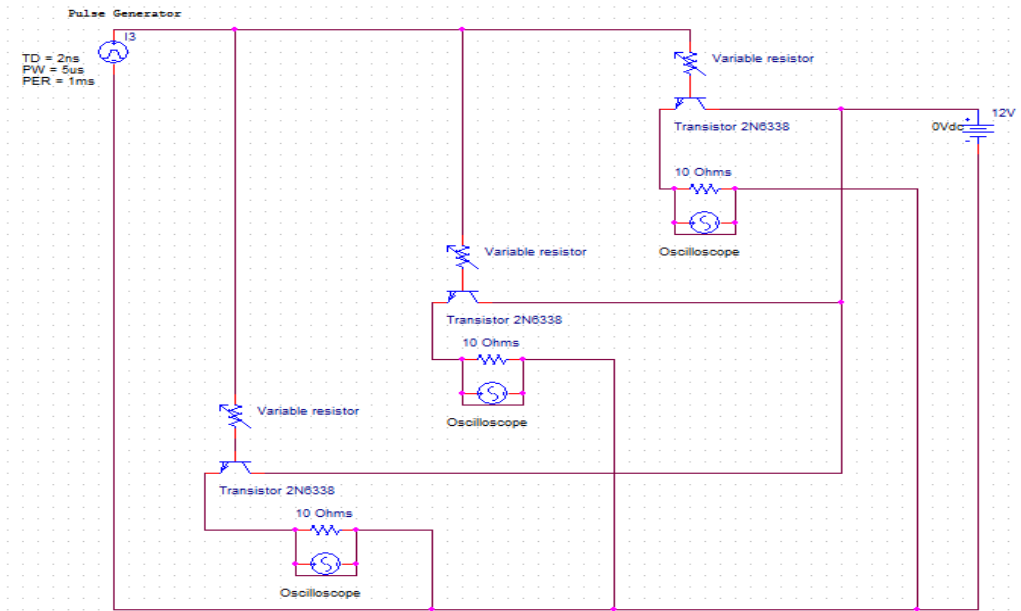


Figure 5-6 Schematic of the electrical controllers circuit

The output beam from the steering section is collected by a 20x lens and directed into a spectrometer and focused onto a CCD camera simultaneously using a beam-splitter. The output beam from the gain section is collected by a cleaved optical fiber connected to an OSA. The top surface of the device is also imaged through a microscope to a CCD camera that is connected to a digital frame grabber as shown in Fig.5-7.

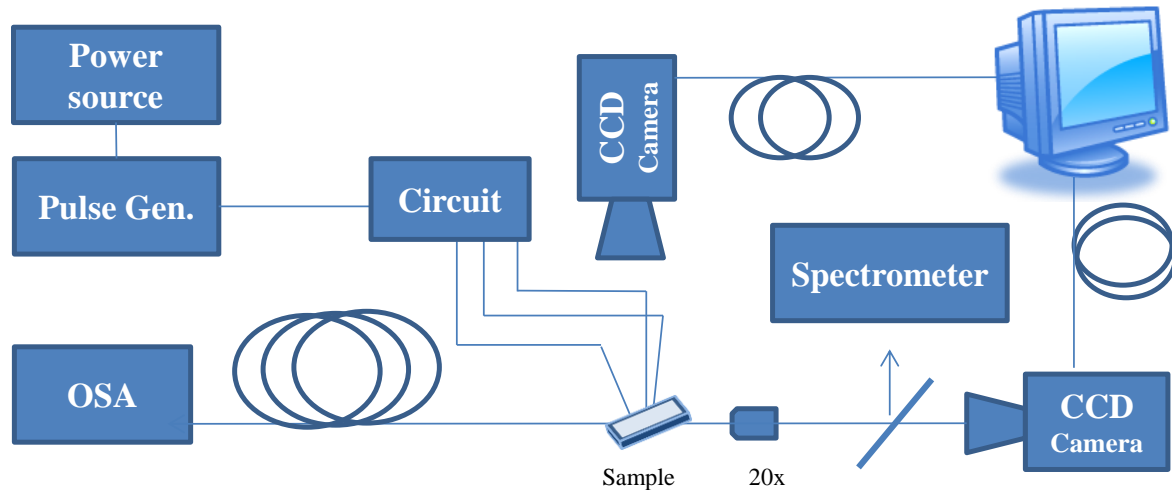


Figure 5-7 Experimental set-up

Three separate devices have been characterized by injecting pulsed electrical currents in the gain sections only at first. One device cleaved to total length of 1.7mm, with a 700 $\mu$ m long gain section has exhibited a threshold current of 300mA. A second device that has been cleaved to total length of 1.1mm with a gain section of 650 $\mu$ m length has been found to exhibit a threshold current of 280mA; finally, a device with a total length 1.4mm that has a 400 $\mu$ m long gain section has exhibited a threshold current of 275mA. The light output powers vs. current characteristics for the devices are shown in Fig.5-8 and table 5-1.

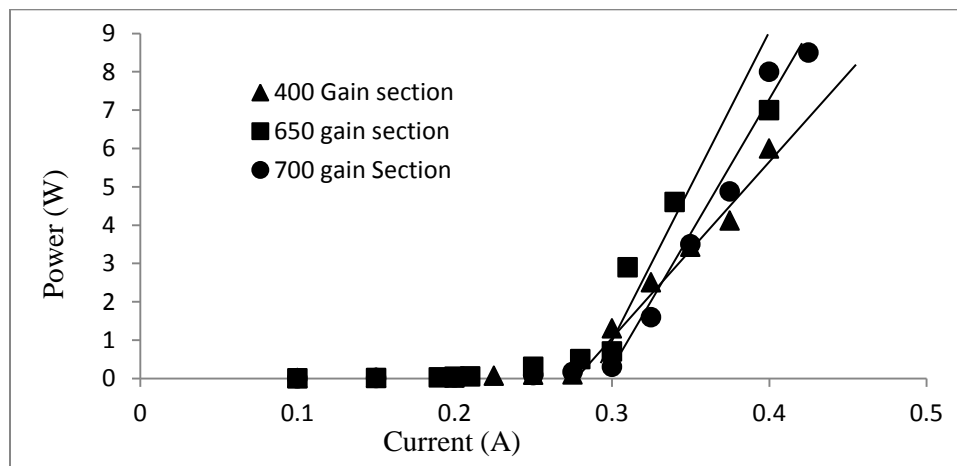


Figure 5-8 L-I curves

Table 5-1 Gain Section L-I curve values

400μm Gain section		700μm Gain section	
Current (mA)	Power (mW)	Current (mA)	Power (mW)
0.1	0.01	0.1	0.0025
0.15	0.02	0.15	0.01125
0.2	0.02	0.2	0.03
0.225	0.07	0.25	0.0875
0.25	0.09	0.275	0.165
0.275	0.1	0.3	0.3
0.3	1.3	0.325	1.6
0.325	3.41	0.35	3.5
0.35	4.60	0.375	4.875
0.375	5.29	0.4	8
0.4	6.56	0.45	8.55
0.425	6.82	0.475	8.55

When current is injected only into the gain section, it emits a wavelength of 800nm that corresponds the peak of the gain spectrum of the uncapped region. This can be explained by the fact that electrons naturally seek the lowest allowable energy states and therefore they accumulate in the region that is least intermixed. Consequently, that region will also have the highest gain coefficient since it has the highest population of electrons. The corresponding threshold current densities for lasing for the devices are determined to be  $J_{th700\mu m} = 2.1\text{KA/cm}^2$  and  $J_{th400\mu m} = 1.9\text{KA/cm}^2$  using

$$J_{th} = \frac{I_{th}}{Area} \quad (5.1)$$

To calculate the extraneous losses in the device, the slope efficiency,  $\eta_s$  is first obtained by extrapolating the maximum measured output power, the power slightly above threshold, and the corresponding current injection levels using the following formula

$$\eta_s = \frac{P_{max} - P_{th}}{I_{max} - I_{th}} \quad (5.2)$$

By multiplying the slope efficiency with the bandgap energy  $E_g$  in electron volts, the approximate differential quantum efficiency,  $\eta_d$  is obtained as

$$\eta_d = \eta_s \times E_g \quad (5.3)$$

and using the differential quantum efficiencies from two devices, we can arrive at a value for the total of all the extraneous losses in the laser cavity using the following equation

$$\alpha = \frac{1}{2} \ln \left( \frac{1}{\ln R1 \cdot \ln R2} \right) \left( \frac{\eta_{d2} - \eta_{d1}}{\eta_{d1} l_1 - \eta_{d2} l_2} \right) \quad (5.4)$$

Using the data for the devices with the 400 $\mu$ m and 700 $\mu$ m long gain sections, the total attenuation constant in the cavity is determined to be  $\alpha = 3.86$ dB/cm. a photograph of the final device with a total length of 1.4mm with 400 $\mu$ m gain section is shown in Fig.5-9.

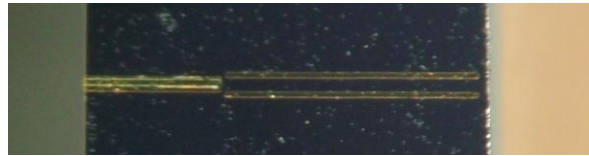


Figure 5-9 Final Device

The device is tested by injecting a series of different current values into the three contacts. The lasing wavelength is tuned in steps of 1nm with a total tuning range of 10nm being achieved in all the tested devices. The results from one device are shown in Fig.5-10 and table 5-2.

Table 5-2 Steering and tunability current injection values for the device with 700 $\mu$ m gain section

Gain Section (mA)	Left Contact (mA)	Right Contact (mA)	Wavelength (nm)
425	0	0	800
420	15	20	799
420	15	30	798
420	30	35	797
405	30	80	796
380	30	110	795
355	30	145	794
320	30	200	793
290	30	210	792
255	30	220	791
240	30	225	790
320	30	200	793
290	30	210	792
255	30	220	791
240	30	225	790

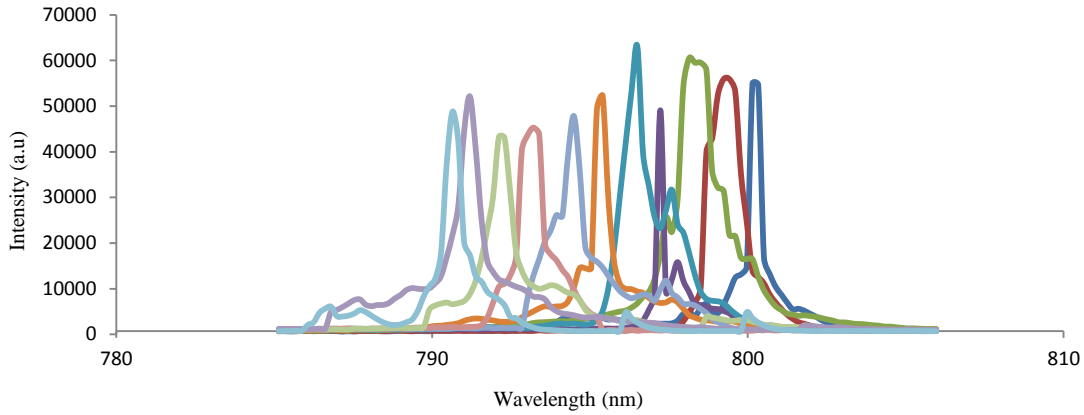


Figure 5-10 700µm laser device wavelength tuning

For the second device design, which has three selectively intermixed regions, two devices are cleaved to total length of 750µm with a 250µm long gain section and 1mm with a 350µm long gain section. The device with 250µm gain section exhibits a threshold current  $I_{th}$  of ~190mA with a calculated threshold current density of  $J_{th(250\mu m)} = 3.8KA/cm^2$ . The device with 300µm gain section exhibits a threshold current  $I_{th}$  of 235~mA with a calculated threshold current density of  $J_{th(350\mu m)} = 3.9KA/cm^2$ . The total attenuation constant in the cavity is determined to be  $\alpha \approx 4.81dB/cm^{-1}$ . Fig. 5-11 and table 5-3 show the L-I curve of the gain section.

Table 5-3 Gain section L-I curve values

250µm Gain section		350µm Gain section	
Current (mA)	Power (mW)	Current (mA)	Power (mW)
10	0.607	10	0.811
25	0.643	25	0.879
50	0.686	50	0.934
75	0.783	75	0.957
100	0.903	100	1.02
125	1.04	125	1.24
150	1.3	150	1.53
175	1.47	175	1.89
190	1.63	190	1.92
200	3.59	200	2.21
225	8.37	235	9.76
275	15.39	275	17.27
300	21.05	300	22.08

Again, to test the wavelength tunability of the laser, we first inject current into the gain section that is high enough to cause the device to lase. The optical beam will remain mainly in the least intermixed region that has the smallest bandgap energy due to electrons accumulation as mentioned above.

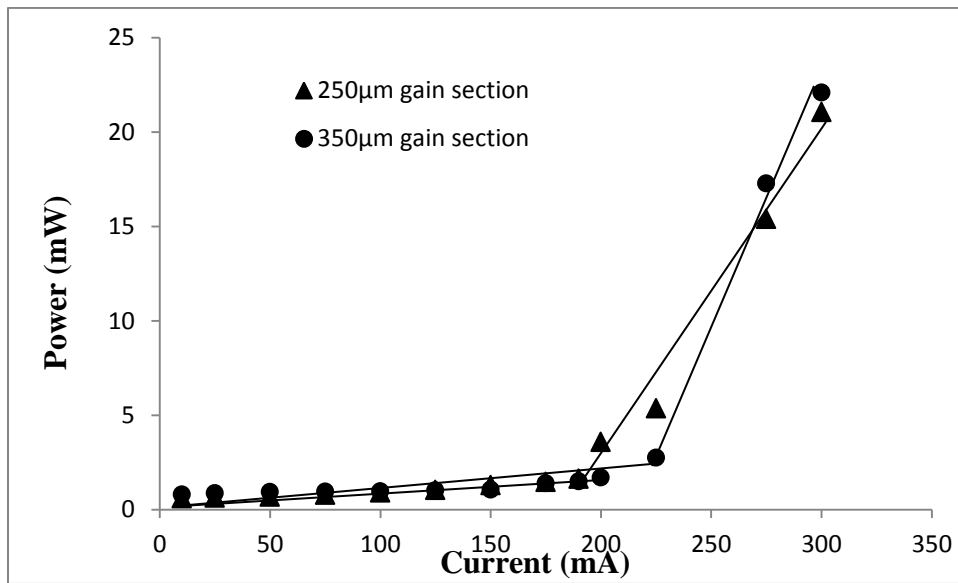


Figure 5-11 L-I curve for the lasers with three intermixed regions

With a pulsed current of 180mA (slightly below  $I_{th}$ ) injected into the gain section, the electroluminescence exiting the output facet is imaged on a CCD camera and an intensity profile is obtained by performing a line-scan across the beam in LABVIEW. The image of the output beam and its intensity profile are shown in Fig 5-12.



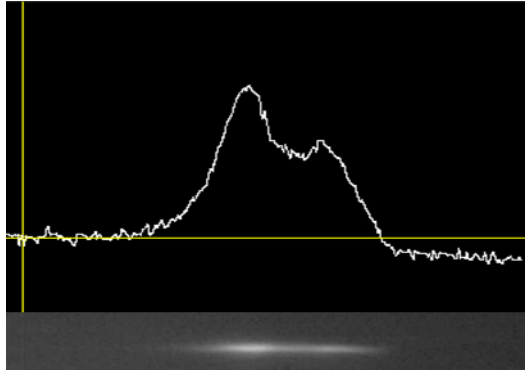


Figure 5-12 L-I curve

The output beam from the gain section of the device is also scanned with a cleaved fiber connected to an optical spectrum analyzer to determine the wavelength emission across that facet. The facet scan starts by aligning and optimizing the cleaved fiber with respect to the gain section facet and monitoring the optical power meter to maximize the amount of power going in to the fiber optic cable. Once the position is optimized, the cleaved fiber is moved to right about  $4\mu\text{m}$  away from the edge of where the gain section using micrometer.

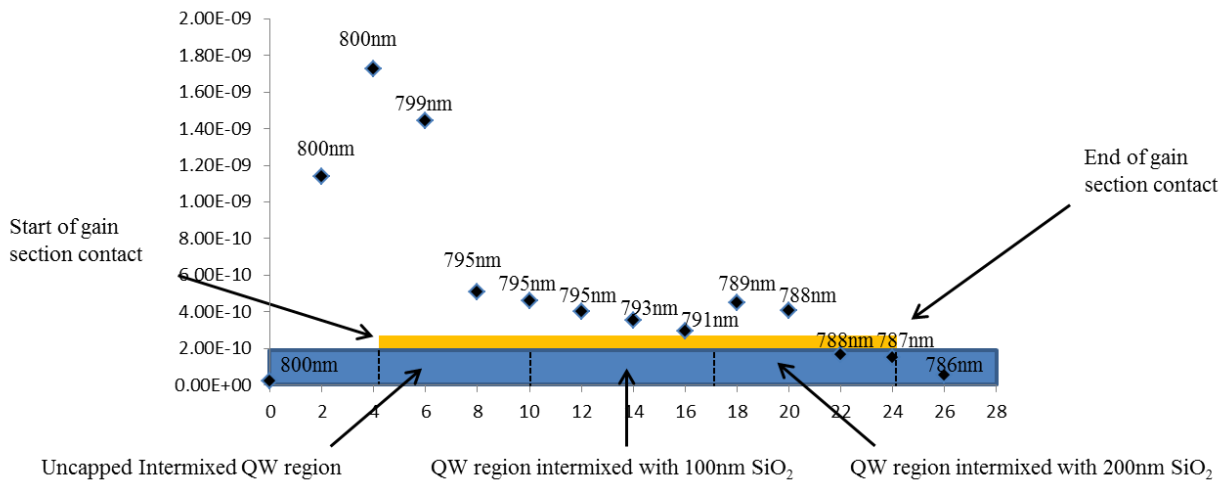


Figure 5-13 Electroluminescence emission across the facet

Current below threshold is then applied to the gain section and the cleaved fiber is moved across the facet covering the gain section contact width end to end. An extra  $4\mu\text{m}$  of movement on each

side is added to collect all emitted light covering a distance of  $28\mu\text{m}$ . Figure 5-13 is a graphical representation of the device cleaved output facet cross section to scale super imposed on the power intensity graph of the scanning range. The gain section contact on top of the structure defines the gain section length which is  $20\mu\text{m}$  long.

The current is next increased to  $> 190\text{mA}$  ( $I_{th}$ ) until laser emission is obtained and the output facet is again imaged on the CCD camera as shown in Fig 5-14. The intensity profile of the beam performed in LABVIEW is also shown in Fig 5-14. In the case of the electroluminescence, we observed a higher intensity the left of the output beam corresponding to the least intermixed region. This is attributed to a larger accumulation of electrons in the lower bandgap semiconductor i.e. the least disordered QW. When the device is operated with above threshold current, the laser emission is observed to emit from the same position of the most intense electroluminescence.

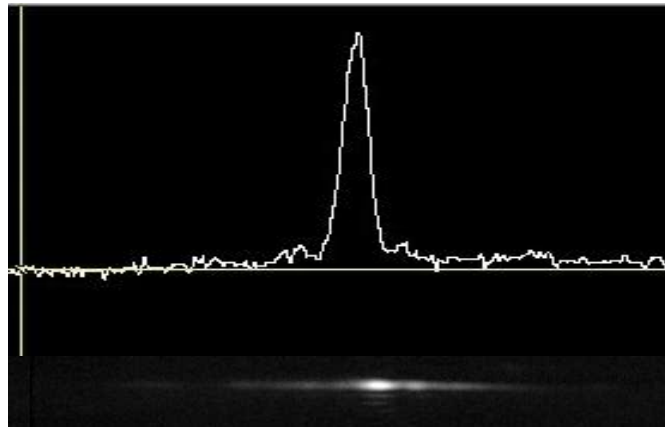


Figure 5-14 Laser facet intensity profile

Fig.5-15 shows the gain section of fabricated device. The three QW selectively intermixed regions with different  $\text{SiO}_2$  film thicknesses of the gain section can be clearly identified.

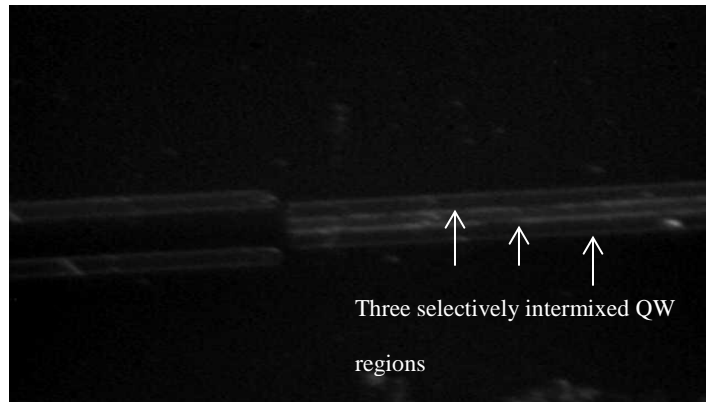


Figure 5-15 Three selectively intermixed QW regions of uncapped, 100nm and 200nm thick SiO<sub>2</sub> of the fabricated device

Electrical currents are then separately injected into the two parallel contacts of the beam-steering section of the device. As the current injected through the contact that is adjacent to the least intermixed region is slowly increased, the lasing beam is gradually pushed toward the more heavily intermixed region across the output. Fig 5-16 shows the emission from the output facet of the beam-steering section as a function of different currents applied through the two contact stripes.

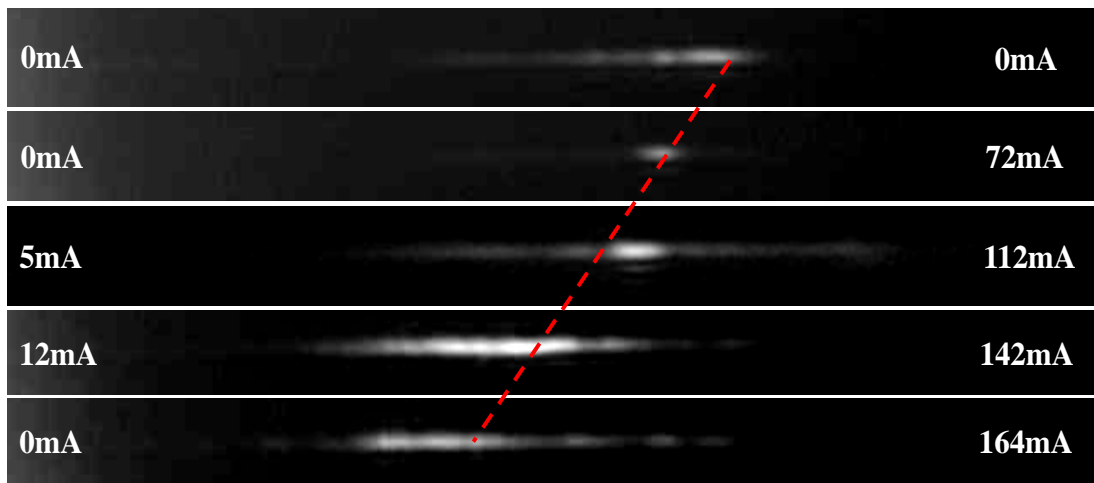


Figure 5-16 Output spot moving across the facet

The gradual movement of the laser beam allows for a fine wavelength tuning because at the interface between the intermixed regions there is a gradient in the degree of intermixing with a

total bandgap energy change of up to 17nm. The values of the currents injected into the gain section and each of the contact stripe of the steering section as well as the corresponding wavelength of the laser emission are shown in table 5-4 and the spectra of the laser emission at these current settings are shown in Fig.5-17.

Table 5-4 Steering and tunability current injection values

Gain (mA)	Left contact(mA)	Right contact(mA)	Wavelength (nm)
220	0	0	800
212	5	0	799
200	12	0	795
200	26	0	794
190	37	15	793
190	64	17	792
183	83	30	791
205	12	93	787
166	11	106	786
153	5	112	785
149	5	137	784
143	0	164	783

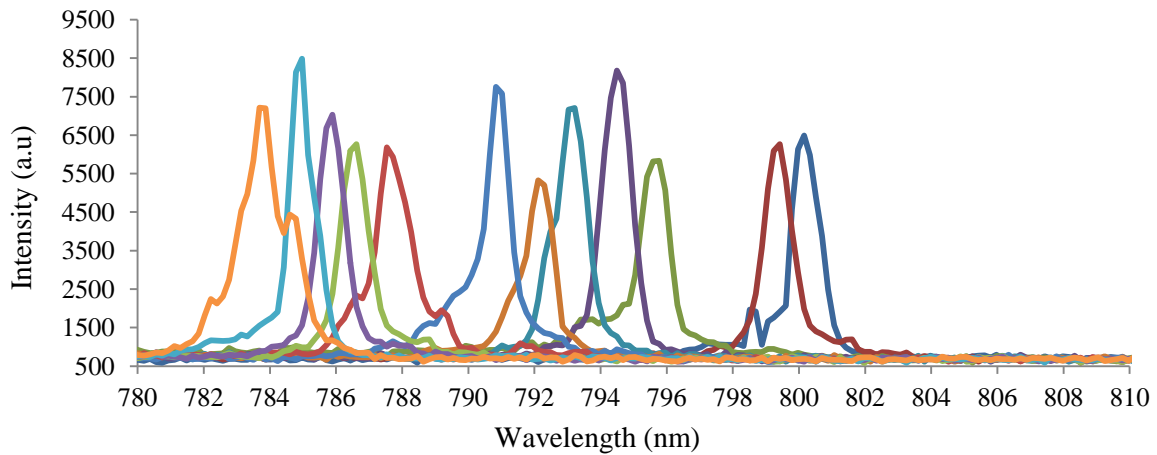


Figure 5-17 Wavelength tunability for the three intermixed region laser

## 5.5 Conclusion

In conclusion, we have fabricated and experimentally investigated two tunable lasers based on optical beam steering over a gain section that consists of two differently intermixed regions. The first device with two QW intermixed regions of different extents has a total wavelength tuning range of 10nm that has achieved by injecting a combination of different values of electrical current, and we have been able to controllably tune the laser emission over the 10nm range in steps of 1nm. The second device of three intermixed QW regions of uncapped, 100nm and 200nm of SiO<sub>2</sub> thick film has a total wavelength tuning range of 17nm. Although the speed of the wavelength switching has not been measured experimentally, it is expected to be only limited by carrier recombination lifetime and therefore should respond on a nanosecond time scale.

## CHAPTER 6: MONOLITHIC DUAL & MULTI-WAVELENGTH LIGHT

### EMITTING DIODES

#### 6.1 Introduction

Light Emitting Diodes (LEDs) have been a target of the optoelectronics industry due to its versatile uses in many of today's technology applications. LEDs are widely marketed as a compliant green technology too[83]. LEDs allow lower power consumption, have longer lasting life, and give better heat dissipation. In the display technology, they provide a brighter illumination, with thinner and smaller panels, as well as better contrast levels. Commercial multicolor LED products are in high demand and have already made significant as major contenders for light fixtures and digital TVs. Most high end video displays and computer monitors available today utilize white LEDs as backlights. However, full color LED displays are also available and are being used to display commercials in most large cities around the world, although size and fabrication complexity in producing multicolor LEDs are still the main challenges that the industry has to overcome [84] for such displays to come down in price sufficiently as to deployable in the home. There are even some applications for visible light communication[85]. Methods have been developed to overcome the size challenge where devices of multi-wavelengths are fabricated by growing two different MQWs on a single structure or nanocolumns emitting RGB wavelengths [86-90]. Although these devices are small in size, they require extensive and complex fabrication processes. We propose a single output monolithic LED shown in Fig. 6-1 that has the ability to shift wavelength by applying electrical currents to several sections. The proposed LED contains three regions with quantum wells (QW) that have been selectively intermixed by varying degrees [91]. Each region will emit a specific wavelength or a color that would be independently controlled. In this work, we set out to prove

the concept using a GaAs/AlGaAs QW structure that emits light in the infrared range of the optical spectrum. However, it is highly conceivable that such technology can be applied to semiconductors that emit in the visible range of the spectrum. The design of the multi-wavelength structure allows for monolithically integrating LED pixels of different wavelengths. In this work, we have designed, fabricated and tested two variations of LED devices based on the same principle of operation. We first investigate a single output dual wavelength LED with independent power controls. We have then fabricated a second device based on the dual wavelength LED, and have added an additional third region with the QW intermixed to a different extent with its own separate intensity control contact. [92, 93]

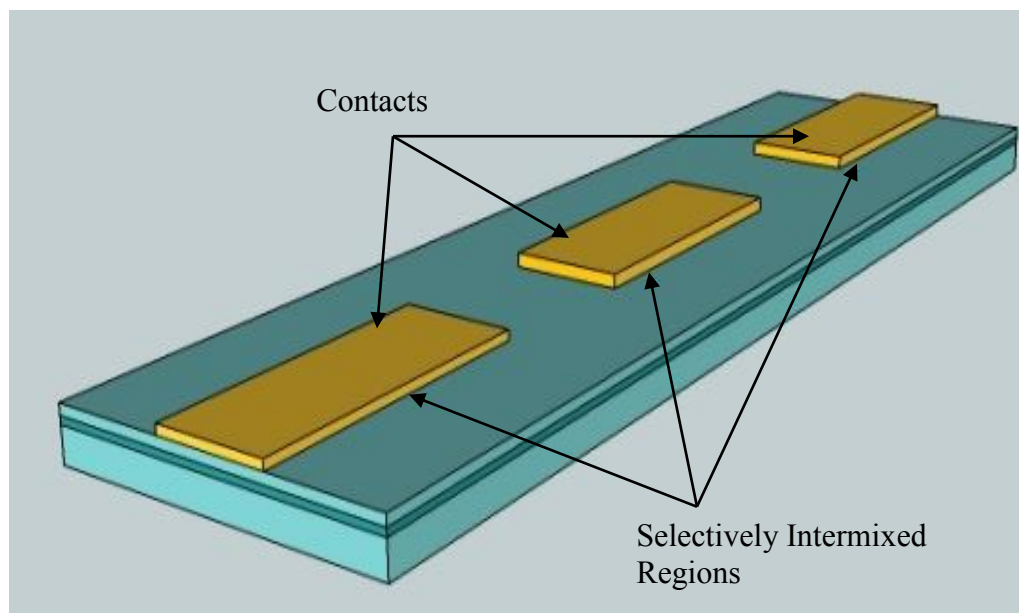


Figure 6-1 Proposed device with three selectively intermixed regions

## 6.2 Dual-Wavelength LED

The first device is a monolithic dual-wavelength LED based on selective intermixing of a QW structure that is induced by dielectric cap annealing. The device has a single output beam that contains photons of different energies origination from two separate sections with independently

controlled intensities. The two regions with different QW bandgap energies created using an impurity-free vacancy induced intermixing technique areas as described in the earlier chapters. Each region is intermixed to varying extent resulting in different luminescence peaks and by separately addressing each section with its own electrical current, the net emission spectrum can be fully controlled. The LED material is the same AlGaAs/GaAs QW p-i-n heterostructure that was used for the optical beam-steering devices and the tunable laser in chapters four and five. The QW structure peak emission wavelengths are at 800nm and 772nm corresponding to intermixed QW regions of uncapped and 400nm of SiO<sub>2</sub> film respectively. Each wavelength has an independent emission power control, allowing the LED to radiate one or two wavelengths at once and the shape of the emission spectrum can be set arbitrarily.

### 6.3 Multi Wavelength Diode

The second device is a monolithically integrated multi-wavelength LED that is also based on dielectric cap induced QW intermixing. The proposed LED emits radiation with multiple wavelength peaks from adjacent areas of one compact easy to fabricate QW structure. Just like the previous device, each wavelength has an independent emission power control, allowing the LED to radiate one or more wavelengths at once. The LED material is the same one that is used for the previous device. The device contains three QW regions that have been intermixed by rapid thermal annealing with no film cover, 100nm and 200nm of SiO<sub>2</sub> films respectively. By separately addressing each section with its own electrical current, the net emission spectrum can be fully controlled.



## 6.4 Device Design

### 6.4.1 Dual Wavelength LED

For the first device we demonstrate a monolithically integrated single output dual-wavelength LED based on selective area intermixing of a QW structure and the device is fabricated using only two photolithographic fabrication steps. Each wavelength has an independent emission power control, allowing the LED to radiate one or more wavelengths separately or at once. The device and can be as small as 200 $\mu\text{m}$ .

The fabricated device is shown in Fig. 6-2 which is based on two selectively intermixed regions. Each region is intermixed to a different extent, thereby resulting in different electroluminescence peaks.

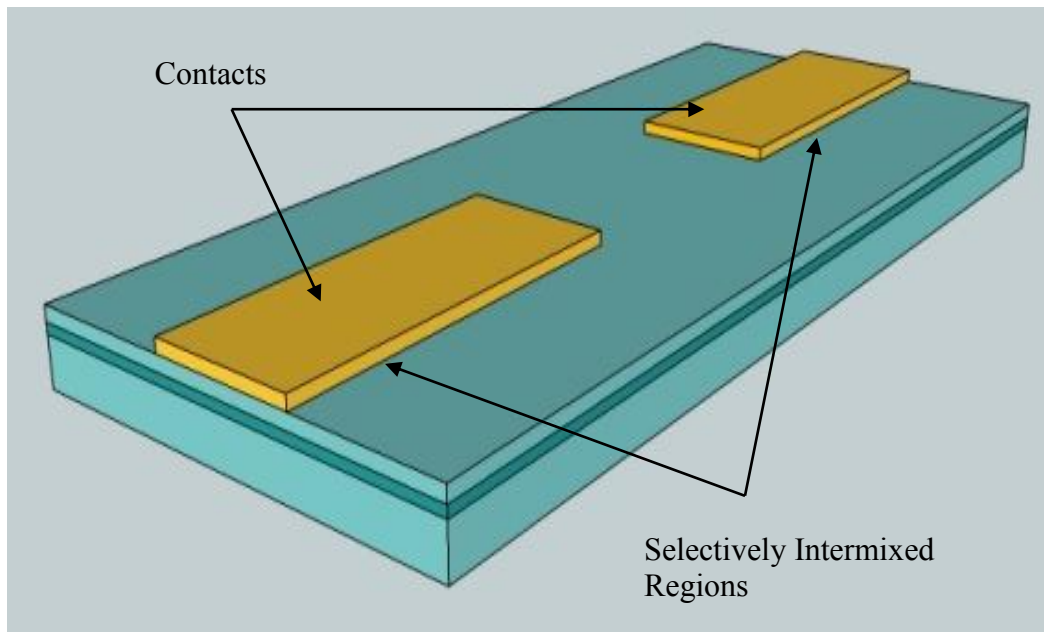


Figure 6-2 Fabricated device with two selectively intermixed regions

In this work, the QW intermixing is induced by impurity-free vacancy diffusion (IFVD) as describe in the earlier chapters. The area that is designated to be the light emitter with a different

optical spectrum is capped with a 200nm thick SiO<sub>2</sub> film and the sample is annealed at a temperature of 975°C for a duration of 20s. The degree of disordering, therefore the resultant bandgap energy can be controlled by using different thicknesses of SiO<sub>2</sub> film [64]. We can controllably tune the wavelength peak of the emission spectrum in the range of 10nm to 60nm compared to the emission spectrum from the as-grown device using a single rapid thermal annealing. Ultimately the choice of substrate material and quantum well intermixing characteristics will determine the wavelength of operation and the range of wavelengths attainable.

Each of the adjacent light emitting regions is covered with a 350µm long by 50µm wide p-type electrical contact and they are separated by 50µm gap. Electrical current can therefore be independently injected into the separate sections allowing full control of the net emission spectrum of the output light.

#### 6.4.2 Multi Wavelength LED

For this device we demonstrate the ability of fabricating a monolithically integrated multi-output multi-wavelength LED based on same principle of the device discussed in section 6.4.1..However, the LED emits radiation with three wavelength peaks instead of two and the light emission areas do not physically overlap. The LED is fabricated using only three photolithographic fabrication steps. Each wavelength has an independent emission power control, allowing the LED to radiate one or more wavelengths separately or all at once. The device and can be as small as 400µm<sup>2</sup>.

The intermixed regions are 20µm wide by 200µm long covered by p-type electrical contacts and separated by 50µm. Electrical current can therefore be independently injected into the separate

sections allowing full control of the net emission spectrum of the output light. Fig 6-3 shows a schematic of the fabricated device.

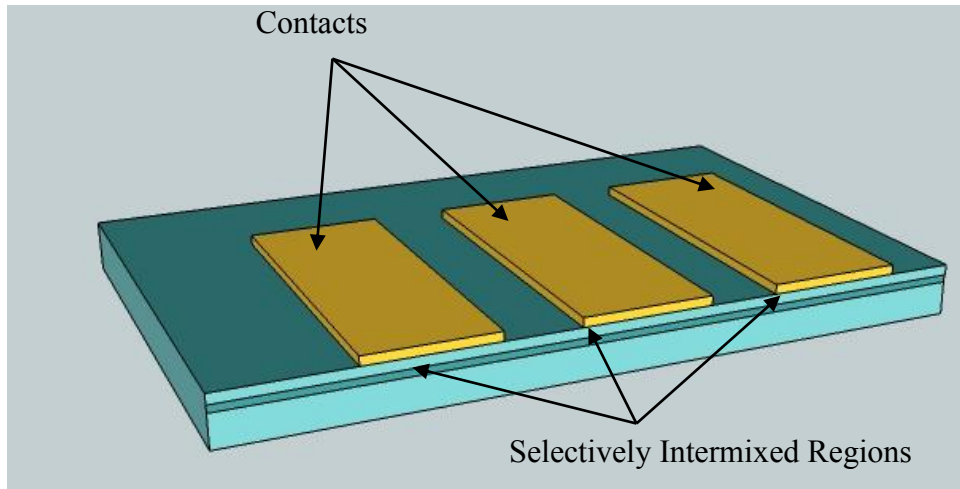


Figure 6-3 System overview showing the fabricated test LED device

### 6.5 Dual Wavelength LED Fabrication

In this work we designed and fabricated the LED using the same GaAs/AlGaAs QW described in chapter 4.3 with graded index separate confinement heterostructure (GRINSCH) *p-i-n* material that has an as-grown electroluminescence peak of 805nm.

#### 6.5.1 Step one

The same process mentioned in chapter 3.3.1 three is repeated to create the masks required to fabricate the LED device. Three masks are used to fabricate the dual-wavelength LED device. The first mask contains the alignment marks, the second mask is designed to create the 10 $\mu$ m wide 1mm long selectively intermixed lines separated by 100 $\mu$ m. Finally, a mask contains the contacts to go over the selectively intermixed regions is fabricated. Fig.6-4 shows the contacts masks for both devices. The length of the device can be determined when the device is cleaved; therefore, the contacts mask as shown allows us to cleave the device to any desired length between 250 $\mu$ m-2mm.

### 6.5.2 Step two

The same procedure mentioned in section 4.4.2 is repeated here to deposit the 100nm thick chromium alignment marks deposition. Once the deposition step is done and the sample is cooled down, the sample is soaked in acetone to lift-off the unwanted metal.

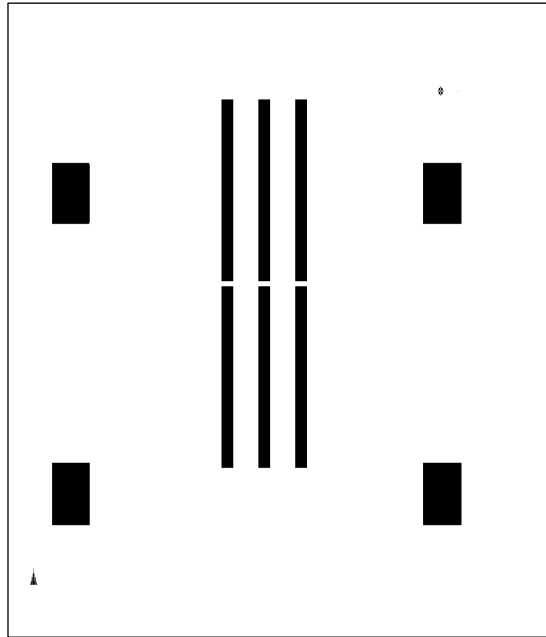


Figure 6-4 Dual wavelength LED contacts mask

### 6.5.3 Step three

The sample is then cleaned with alcohols and placed in the Plasmatherm 790 PECVD machine to deposit a 400nm thick SiO<sub>2</sub> layer. The same process and recipe used in chapter 3.3.2 is repeated for this sample.

### 6.5.4 Step four

The sample is placed on a spinner and NR7-1000PY photoresist is first spun on top of the sample at 4000 rpm for 40s followed a 1min hot plate bake at 150°C. Since we are dividing into only two selectively intermixed regions of where each area is intermixed to different extent, mask #2 is used to expose the areas to be selectively intermixed following another hot plate bake step of

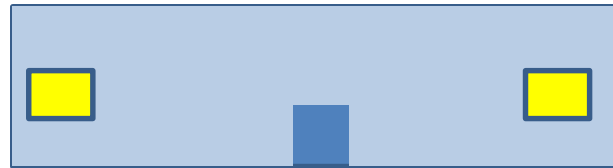
at 100°C for 1min. Finally the resist is developed using RD6 for 7s and a window is opened exposing the SiO<sub>2</sub> film at that region. The fabrication process steps are shown in Fig. 6-5.



1- First mask is exposed followed by chrome evaporation and lift-off (alignment marks)



SiO<sub>2</sub> PECVD deposition (400nm)



3- Mask two is exposed followed by subsequent Selective RIE etching to define 20µm wide uncapped window

Figure 6-5 System overview showing the fabricated test LED device

### 6.5.5 Step five

The sample is placed in the RIE chamber and the SiO<sub>2</sub> film where we opened the windows are etched off completely using the Plasmatherm machine with the same parameters mentioned in chapter 4.4.5.

### 6.5.6 Step six

The sample is cleaned and is then annealed at 975°C for 20s which is the same process in chapter 4.4.7. The 400nm SiO<sub>2</sub> intermixed areas cover the whole device except for the section where it was etched off. The SiO<sub>2</sub> is then completely removed via BOE.

### 6.5.7 Step seven

Using the chromium alignment marks that were evaporated in the first step, the final lithography step is performed to deposit contacts on top of the selectively intermixed areas, this step is mentioned in details in chapter 4.4.9.

### 6.5.8 Step eight

The sample is polished down to a thickness of 150µm using the same method described in chapter 4.4.10.

### 6.5.9 Step nine

The sample is glued to a glass slide and n-type contact is evaporated as mentioned in chapter 4.4.11. Finally the device is cleaved to about 1.8mm. Fig.6-6 shows a photograph of the fabricated device with 20µm contacts separation.

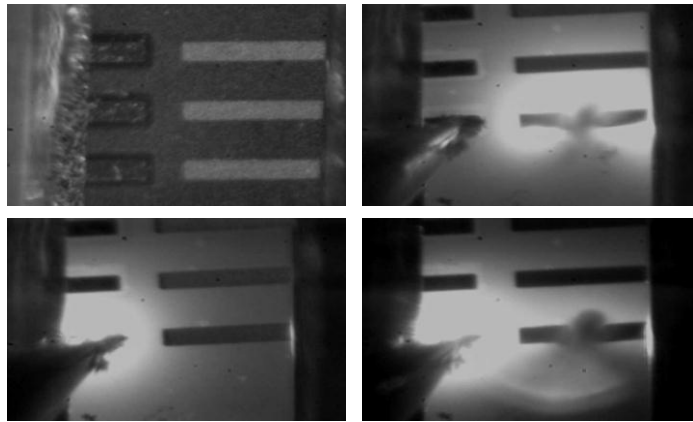


Figure 6-6 (a) Sequence pictures showing: 1.Three fabricated LED devices, 2.Current applied to the 400nm SiO<sub>2</sub> intermixed region, 3. Current applied to the uncapped region and 4.Current applied to both regions.

## 6.6 Multi Wavelength LED Fabrication

Just like the previous device, we designed and fabricated the LED on the same GaAs/AlGaAs QW graded index separate confinement heterostructure (GRINSCH) p-i-n material..

### 6.6.1 Step one

The same process mentioned in chapter 3.3.1 is used here to produce the masks for the multi-wavelength LED device. Four photolithographic masks were designed for this device. The first mask is the alignment marks mask, which is also repeated throughout the rest of the masks. The second and third masks define the 10 $\mu$ m wide by 2mm windows for the intermixed regions. Finally, the fourth mask is the P-type contacts mask.

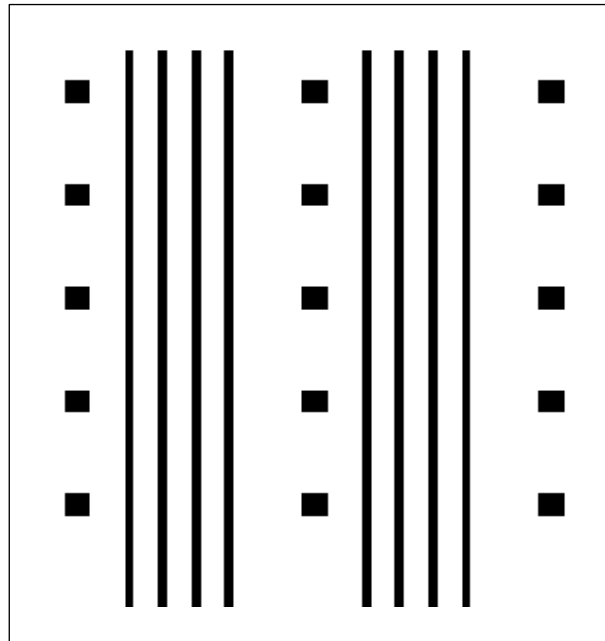


Figure 6-7 Multi Wavelength LED contacts mask design

### 6.6.2 Step two

This step is a repeat of step 6.5.2, a 100nm chromium alignment marks are evaporated on top of the sample.

### 6.6.3 Step three

This step is a repeat of step 6.5.3, a 400nm SiO<sub>2</sub> layer is deposited on top of the structure using Plasmatherm 790 PECVD machine.

### 6.6.4 Step four

This step is a repeat of step 6.5.4, we are dividing into three selectively intermixed regions of where each area is intermixed to different extent, NR7-1000PY photoresist is first spun on top of the sample at 4000 rpm for 40s followed a 1min hot plate bake at 150°C. Then mask #2 is used to expose the first 10µm areas for 5s using the aligner following by another hot plate bake step of 1min at 100°C. Finally the resist is developed using RD6 for 7s.

### 6.6.5 Step five

The sample is placed in the RIE chamber and the first set of exposed SiO<sub>2</sub> in the 10µm windows is etched using the Plasmatherm 790 machine with the same process and recipe in chapter 4.4.5. The film is etched down 200nm of SiO<sub>2</sub>.

### 6.6.6 Repeat of steps four and five

The sample is cleaned and NR7—1000PY photoresist is spun, exposed and developed using the same parameters mentioned in 6.6.4. Mask #3 is then used to create the other 10µm lines set and the SiO<sub>2</sub> layer was further etched off completely leaving us with a two 10µm lines set of 200nm SiO<sub>2</sub> and an uncapped set.

### 6.6.7 Step six

This step is a repeat of 6.5.6, the sample is cleaned and is then annealed at 975°C for 20s which is the same process in chapter 4.4.7. The 400nm SiO<sub>2</sub> intermixed areas cover the whole device except for the section where it was etched off. The SiO<sub>2</sub> is then completely removed via BOE.



### 6.6.8 Step seven

This step is a repeat of 6.5.7, using the chromium alignment marks that were evaporated in the first step, the final lithography step is performed to deposit contacts on top of the selectively intermixed areas, this step is mentioned in details in chapter 4.4.9.

### 6.6.9 Step eight

The sample is polished down to a thickness of 150 $\mu\text{m}$  using the same method described in chapter 4.4.10.

### 6.6.10 Step nine

Both samples are glued to a glass slide and n-type contacts are evaporated as mentioned in chapter 4.4.11. Finally the device is cleaved to about 1.8 mm. The complete fabrication process is shown in Fig. 6-7.

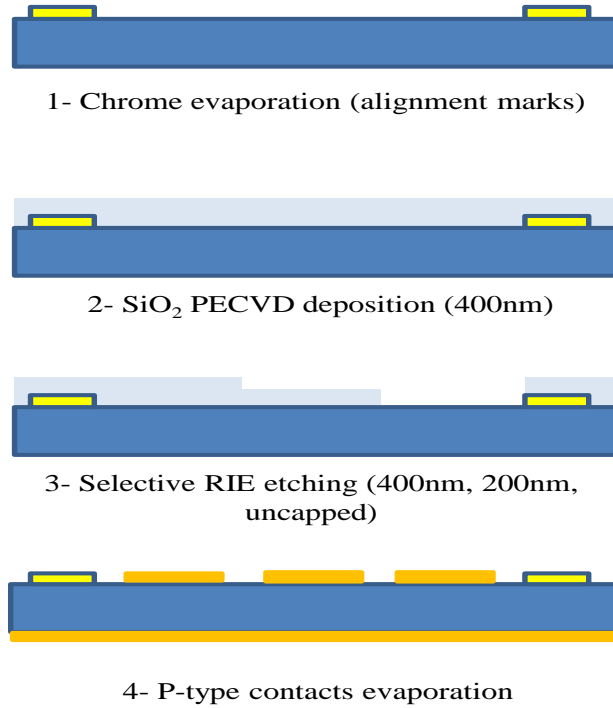


Figure 6-8 System overview showing the fabricated test LED device

## 6.7 Testing and Results

To determine the required amount of intermixing needed to emit three wavelength peaks from the LED, the degree of disordering was measured by comparing the electroluminescence for different samples with different SiO<sub>2</sub> caps as discussed previously in chapter 4.5 Fig. 4-7.

The dual LED device was cleaved at both end-facets for a total length of 350µm and its performance is investigated using two separate current drivers to inject pulsed currents to the contact stripes via micropositioner probes. Pulsed currents are applied to each contact separately then to both contacts simultaneously. When pulsed current is applied, the generated electroluminescence propagates in the slab waveguide and exiting out of both the front and back facets. The primary output facet is the one that abuts the region intermixed by the 400nm thick SiO<sub>2</sub> cap since the longer wavelength emission from the non-intermixed region can pass through intermixed region without suffering excessive absorption [68]. The final device under test is shown in Fig 6-9.

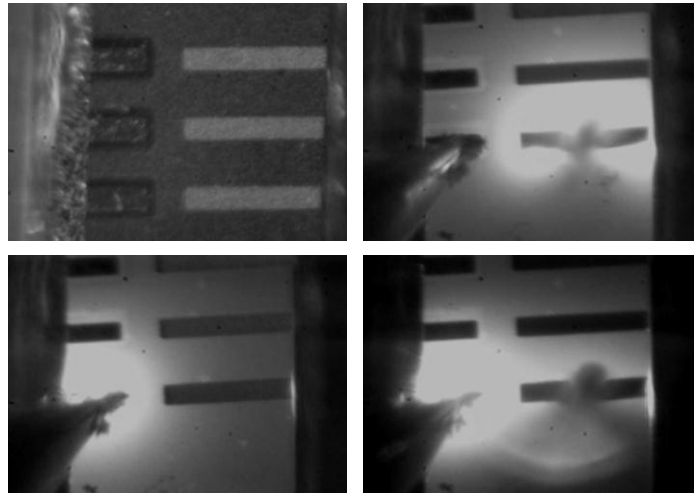


Figure 6-9 shows sequence pictures of the top view of the device with different combinations of current applied to two contacts of the device.

Using the same setup described in chapters 4.5 Fig. 4-8 and 5.4 Fig. 5-7, the device is mounted on a copper plate and pulsed electrical currents are injected into the contacts with the output facet

is collected by a 20x lens and focused on a spectrometer. The outputs from the edge facet and that from the device top surface are simultaneously monitored by two CCD cameras that are connected to a digital frame grabber. Each of the outputs is also collected by an optical fiber into an optical spectrum analyzer.

Experimental results show that the peak emission from the originally uncapped annealed region is blue shifted by 5nm from the peak wavelength of the as-grown sample. On the other hand, a controllable blue shift of the peak wavelength of emission from the SiO<sub>2</sub> capped region can be obtained depending on the thickness of the SiO<sub>2</sub> film, with a 400nm thickness producing 28nm of wavelength shift.

Fig. 6-10 shows the spectra obtained from the primary edge output facet of the device with current injected to the contacts separately. An optical power meter was placed at the output recorded an optical power of 15mW and 15.1mW for the capped and the uncapped regions respectively at 37mA current injection which resulted in a calculated responsivity of 0.4W/A. From chapter 2.3 equation 2.8 we can derive the following equation to calculate the overall quantum efficiency

$$\mathcal{R} = \frac{p_o}{I} = \frac{\eta_o h \omega}{q} \quad (6.1)$$

$$\mathcal{R} = \frac{1.24 \eta_o}{\lambda(\mu\text{m})} \quad (6.2)$$

Therefore, the overall quantum efficiency for LED is 0.141.

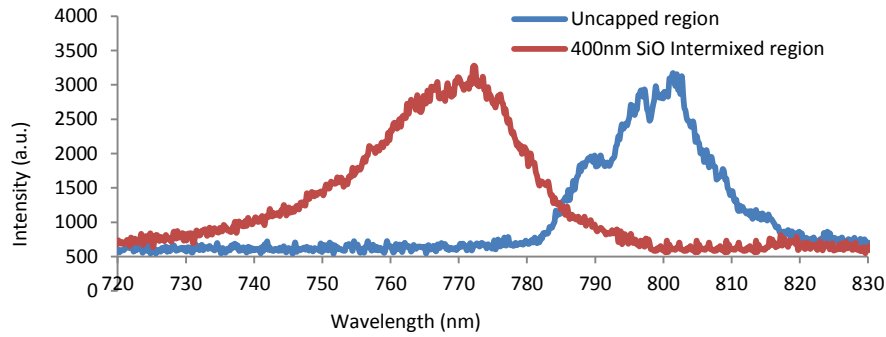


Figure 6-10 Device output spectrum.

The multi wavelength device is cleaved to a total length of 550 $\mu$ m and tested using the same set-up used to test the dual wavelength LED and extra electrical probe was added to address the third contact. The device was tested using two different orientations. First, the LED was mounted such that of the three disordered area contacts face the lens as shown in Fig 6-11(a). Therefore to collect the emitted wavelength, the lens had to be moved accordingly. This design seemed impractical because it requires a complex housing to focus the maximum amount of light coming out of each region.

As mentioned in chapter 2.6, light propagates in the active region in all directions. Therefore, to overcome the design flaw of having three consecutive outputs from one device, the device is rotated 90° so that the stripe with the maximum intermixing region is closest to the 20x lens as shown in Fig 6-11 (b) The primary output facet is the one that abuts the region intermixed by the 400nm thick SiO<sub>2</sub> cap since the longer wavelength emission from the non-intermixed region can pass through intermixed region without suffering excessive absorption [68]. However, due to the directionality of the contacts, the output power is too low. This design flaw can be avoided by adopting the design in Fig. 6-1.

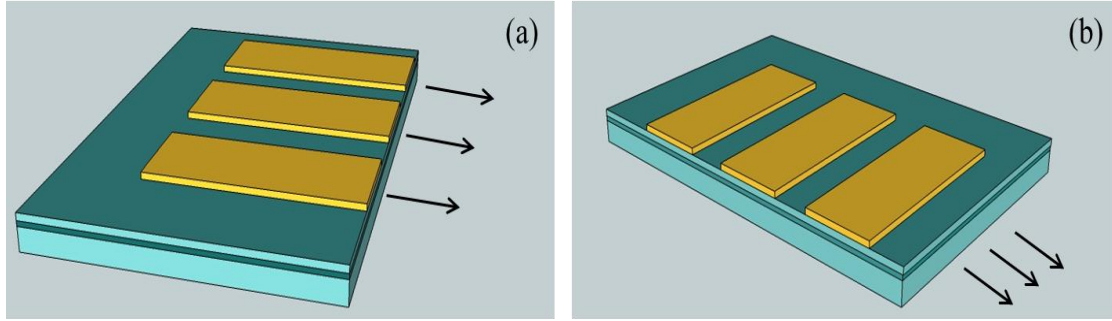


Figure 6-11 (a) Three output device test orientation (b) Single output device test orientation

Experimental electroluminescence results similar to what we have obtained for the dual wavelength LED were recorded, however an additional wavelength that corresponds to the intermediated intermixed region was obtained, which we expected based on our design.

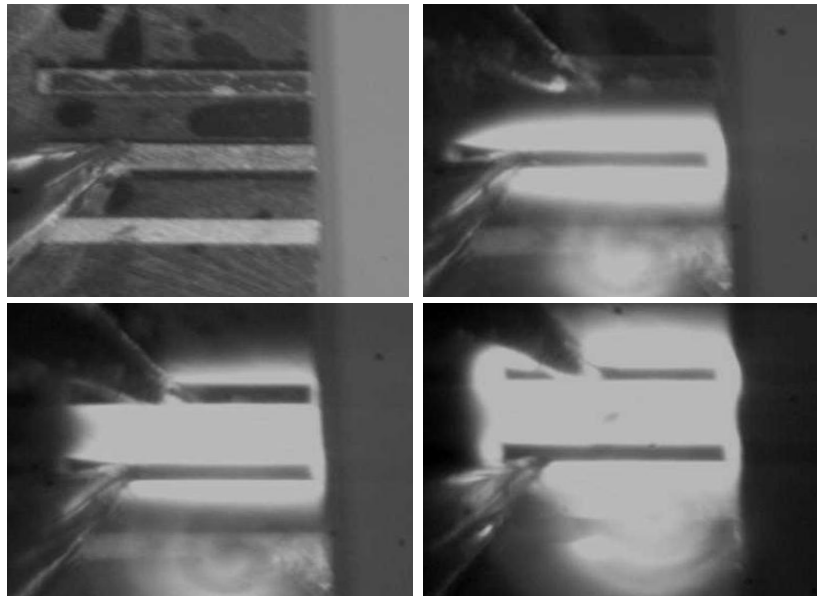


Figure 6-12 Sequence picture of the device under test

Fig. 6-12 shows the spectra obtained from the primary edge output facet of the device with current injected to the contacts separately. An optical power meter was placed at the output recorded an optical power of 11.1mW, 11.2mW and 11mW for the 400nm capped, 200nm capped and the uncapped regions respectively at 50mA current injection which resulted in a

calculated responsivity of  $\approx 0.22$  W/A. Using equation (2.6) we calculated the overall quantum efficiency to be 0.25

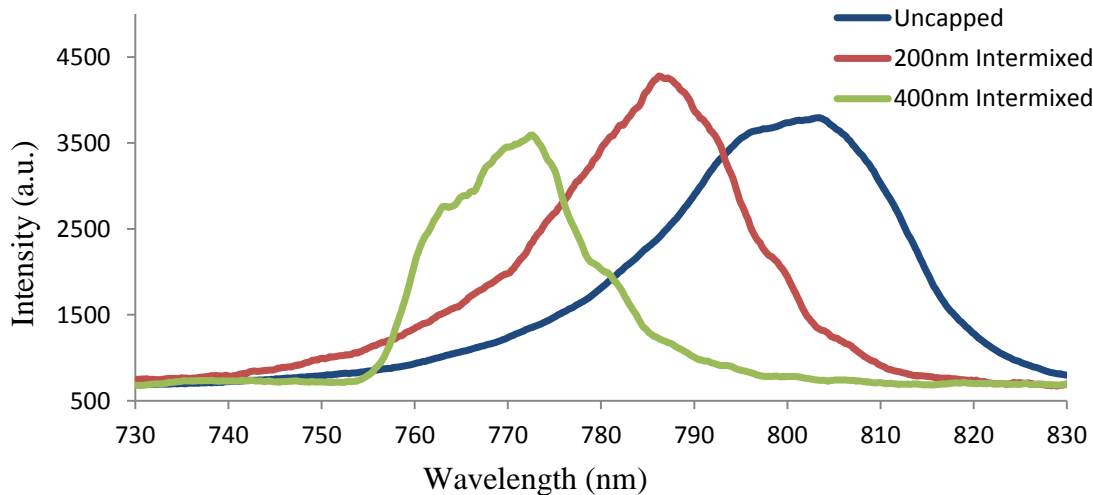


Figure 6-13 Device output spectra

## 6.8 Conclusion

In conclusion, we have fabricated and experimentally investigated two LED devices. The first device is a single output dual wavelength monolithic LED device based on a selectively intermixed GaAs/AlGaAs QW laser structure. Wavelengths intensities are independently controlled by two separate current sources. This approach shows the ability to emit two wavelengths from one structure simultaneously or separately with different intensities. The electroluminescence results indicate that the QW structure has the ability to controllably emit 800nm and 772nm either simultaneously or separately.

The second device that we have fabricated and experimentally investigated is a multi-output multi wavelength monolithic LED device based on a selectively intermixed GaAs/AlGaAs QW laser structure. Wavelengths intensities are independently controlled by three separate current sources. This approach shows the ability to emit three wavelengths from one structure simultaneously or separately with different intensities. The electroluminescence results indicate

that the QW structure has the ability to controllably emit 800nm, 789nm and 772nm either simultaneously or separately. We believe that a monolithic multicolor RGB LED can be fabricated based on the same principle shown here.

## CHAPTER 7: CONCLUSIONS & FUTURE WORK

In this work we discuss two optoelectronic devices that have been fabricated using similar methods. In particular we have applied a quantum well intermixing technique that is an impurity-free vacancy disordering process that is activated by a high temperature rapid thermal annealing of a silica capped structure. We are able to control the degree of disordering by adjusting the thickness of the deposited SiO<sub>2</sub> film. Area-selectivity is obtained by defining areas that are covered by the film as well as the thickness of the film in these areas using photolithography and reactive ion etching. The localized quantum well disordering allows for integration of multiple bandgap regions on a single semiconductor substrate.

The first device that we investigated is a monolithically integrated tunable laser diode that consists of an optical beam-steering section and a gain section. The gain section is divided by selective-area intermixing, to produce two or three regions of different optical bandgaps. The optical beam generated and then re-amplified in the same gain section is steered over a particular section of the selectively intermixed regions by optical beam-steering that relies on carrier induced refractive index reduction. The mechanism is a combination of free carrier plasma effect and refractive index change that is associated with band filling nonlinearities. As the optical beam is steered from one region to another; it emits the wavelength corresponding to gain spectrum of the region that it is steered into. It has also been shown that due to the gradient in between the selectively intermixed regions we are able to achieve fine wavelength tunability over between the gain spectra of the two intermixed QW regions. However, we were not able to achieve the full wavelength tunability range that would be predicted in the original design from the data on electroluminescence characterization of the intermixing of the QW structure. We believe that in the region that have been intermixed to the most extreme, population inversion



can no longer be achieved and therefore optical gain cannot be obtained. Hence when the optical beam is steered to that region lasing action is not possible which explains the specific missing laser wavelength. To improve the device tunability and the functionality of this laser, we believe that gradual grading in the optical band gap of the gain section will provide a better tunable laser device. Furthermore, a different choice of the semiconductor material can improve the range of bandgap change than can be obtained using the selective-area QW intermixing process. Our current material gets intermixed to the max using our 400nm SiO<sub>2</sub> film it produces a maximum of 35nm blue shift. If we were to use a material with a smaller bandgap, it will allow us to have larger blue shifts and better selectivity range compared to the highest intermixed region of the device. However, smaller bandgaps will result in infrared wavelength emission which is not desirable for our intended applications.

In the second part of this research we explore the ability to fabricate a multi wavelength LED on a one single QW structure. We utilize the same area-selective intermixing of QW in order to fabricate a monolithic LEDs with multiple wavelengths operation. We have been able to demonstrate an easy cost-effective and highly reproducible fabrication method of producing the LED. The device can be as small as 250µm<sup>2</sup>. The main idea behind this work is to be able to fabricate an LED device that emits the three primary colors (RGB) since it is a widely desirable product with huge impact on today's technology especially with booming market of color displays. Two designs have been discussed, fabricated and tested. The first device consists of two regions that emitting light with spectra that have a wavelength separation of ~33nm. The second device consists of three regions emitting light with wavelengths that cover the same range of spectra as the previous device. However while the previous device has one single physical output, this one has multiple outputs, each corresponding to the region's spectrum. More

research is needed for the LED devices in order to optimize the ability to shift the operating wavelength over a larger spectral bandwidth.

## LIST OF REFERENCES

1. Agrawal, G.P., *Fiber-Optic Communication Systems*. Second ed. Microwave and optical Engineering, ed. K. Chang. 1997, New York: John Wiley & Sons, Inc. 2-5.
2. Anle, S. *100 G Stands Tall with A Strong backbone*. Huawei editorial, 2010.
3. Proakis, J.G. and M. Salehi, *Digital Communications*. Fifth ed. 2008, New York, NY: McGraw-Hill Higher Education.
4. Rappaport, T.S., *Wireless Communications Principles and practices*. Second ed, ed. T.S. Rappaport. 2002, Upper Saddle River, NJ: Prentice Hall, Inc.
5. Sandra R. Selmic, T.-M.C., JiehPing Sih, Jay B. Kirk, Art Mantie, Jerome K. Butler, David Bour and Gary A. Evans, *Design and Characterization of 1.3- $\mu$ m AlGaInAs-InP Multiple-Quantum-Well Lasers*. IEEE J. of Selected Topics in Quantum Electronics, 2001. **7**(2): p. 340-349.
6. Tajima, K., et al., *Ultralow Loss and Long Length Photonic Crystal Fiber*. Journal of Lightwave Technology, 2004. **22**(1): p. 7.
7. Harun, S.W., et al., *An overview on S-band erbium-doped fiber amplifiers*. Laser Physics Letters, 2007. **4**(1).
8. Yahel, E., O. Hess, and A.A. Hardy, *High-power ultrashort-pulse fiber amplifiers*. IEEE Journal of Quantum Electronics, 2007. **43**(9): p. 824-832.
9. Bigo, S., *Multiterabit/s DWDM Terrestrial Transmission With Bandwidth-Limiting Optical Filtering*. IEEE Journal of Selected Topics in Quantum Electronics, 2004. **10**(2): p. 329-340.
10. Du, P.P.a.D.-Z., *Combinatorial Optimization in Communication Networks*, ed. Y.L.a.D.-Z.D. Maggie Xiaoyan Cheng. Vol. 18. 2006, Ney York, NY: Springer Science+Business Media.
11. Dan Forsberg, G.H., Wolf-Dietrich Moeller and Valteri Niemi, *LTE Security*. 2011, United Kigdom: Johm Wiley & Sons.
12. B. Cai, A.S., A. Rivers, J. S. Roberts, *Multiple Quantum Well-Tuned GaAs/AlGaAs laser*. Electronics Letters, 1989. **25**(2): p. 145-146.
13. Richard Normandin, S.L., Francoise Chatenoud, and Robin L. Williams, *Monolithic, Surface-Emitting , Semiconductor Visible Lasers and Spectrometers for WDM Fiber Communication Systems*. Jounal of Quantum Electronics, 1991. **27**(6): p. 1520- 1530.
14. Bickel, N., *Electro-optical and All-optical Switching in Multimode Interference Waveguides Incoprating Semiconductor Nanostructures*, in *CREOL,The College of Optics and Photonics*. 2010, University of Central Florida: Orlando. p. 190.
15. N. K. Dutta, W.S.H., D. Vakhshoori, H. Ham, P. N. Freeman, J.F de Jong and J. Loata, *Strain Compensated InGaAs-GaAsP-InGaP laser*. IEEE Photonics Technology Letters, 1996. **8**(7): p. 852-854.
16. Connie J. Chang-Hasnain, J.P.H., Chung-En Zah, M. W. Maeda, L. T. Florez, N. G. Stoffel, and Tien-Pei Lee, *Multiple Wavelength Tunable Surface-Emitting Laser Arrays*. IEEE Journal Quantum Electronics, 1991. **27**(6): p. 1368-1376.
17. H. S. Gingrich, D.R.C., S.-Z. Sun, S. D. Hersee, L. F. Lester and S. R. J. Brueck, *Broadly Tunable External Cavity Laser Diodes with Staggered Thickness Multiple Quantum Wells*. IEEE Photonics Technology Letters, 1997. **9**(2): p. 155-157.
18. James W. Raring, E.J.S., Leif A. Johansson, Matt N. Sysak, Jonathon S. Barton, Milan L. Mařanoviã, and Larry A. Coldren, *Demonstration of Widely Tunable Single-Chip 10-*

- Gb/s Laser-Modulators Using Multiple-Bandgap InGaAsP Quantum-Well Intermixing.* IEEE Photonics Technology Letters, 2004. **16**(7): p. 1613-1615.
19. Eldada, L., *Advances in telecom and datacom optical component.* Optical Engineering, 2001. **40**: p. 1165–1178
  20. May-Arrijoja, D.A. and P. LiKamWa, *An Integrated 1x3 InP photonic switch,* in LEOS. 2006, IEEE. p. 532-533
  21. M. Aoki, M.S., H. Sano, T. Kawano, T. Ido, T. Taniwatari, K. Uomi, and A. Takai, , *InGaAs/InGaAsP MQW electroabsorption modulator integrated with a DFB laser fabricated by band-gap energy control selective-area MOCVD.* IEEE J. Quantum Electron, 1993. **29**: p. 2088-2096.
  22. J. Werner, E.K., N. G. Stoffel, E. Colas, S. A. Schwarz et al, *Integrated external cavity GaAs/AlGaAs lasers using selective quantum well disordering.* Appl. Phys. Lett., 1989. **55**: p. 540-541.
  23. V. Jayaraman, Z.M.C., and L. A. Coldren, *Theory, Design, and Performance of Extended Tuning Range Semiconductor Lasers with Sampled Gratings.* IEEE J. Quantum. Electron, 1993. **29**(6): p. 1824-1834.
  24. H. Ishii, H.T., F. Kano, Y. Tohmori, Y. Kondo, and Y. Yoshikuni, *Quasicontinuous Wavelength Tuning in Super-structure-grating (SSG) DBR Lasers.* IEEE J. Quantum Electron, 1996. **23**(3): p. 433-441.
  25. Richard Phelan, W.-H.G., Qiaoyin Lu, Diarmuid Byrne, Brendan Roycroft, Paul Lambkin, Brian Corbett, Frank Smyth, Liam P. Barry, Brian Kelly, James O’Gorman, and John F. Donegan, *A Novel Two Section Tunable Discrete Mode Fabry-Pèrot Laser Exhibiting Nanosecond Wavelength Switching.* IEEE J. Quantum Electron., 2008. **44**(4): p. 331-337.
  26. David Welch, R.G.W., Jo S, major, Ross D. Bringans, David K. Fork, G. A. Neville Comell, Robert L. Thornton, *Monolithic multi-wavelength laser diode array.* 1995, SDL, Inc: USA.
  27. Wang, X., et al. *Silicon Cantilever-Waveguide Displacement Sensors.* in OAS/FIO. 2006.
  28. P Sievil, V.-P.R.o., O Hahtela, N Chekurov, J Kauppinen and I Tittonen, *Fabrication and characterization of an ultrasensitive acousto-optical cantilever.* Journal of Micromechanics and Microengineering, 2007. **17**: p. 852-859.
  29. Kevin E. Burcham, G.N.D.B., and Joseph T. Boyd, *Micromachined Silicon Cantilever Beam Accelerometer Incorporating an Integrated Optical Waveguide,* in SPIE Integrated Optics and Microstructures. 1992, SPIE.
  30. Alleny, M.G., *Diode laser absorption sensors for gas-dynamic and combustion flows.* Meas. Sci. Technol., 1998. **9**: p. 545-562.
  31. Peter Werle, F.S., Karl Maurer, Robert Kormann, Robert M. ucke, Bernd J. anker, *Near- and mid-infrared laser-optical sensors for gas analysis.* Optics and Lasers in Engineering, 2001. **37**: p. 101-114.
  32. Jharna Mandal, S.P., Tong Sun, Kenneth T. V. Grattan, Andreas T. Augousti, and Scott A. Wade, *Bragg Grating-Based Fiber-Optic Laser Probe for Temperature Sensing.* IEEE PHOTONICS TECHNOLOGY LETTERS, 2004. **16**(1): p. 218-220.
  33. Thomas Toö pfer, K.P.P., Yasuharu Mine, Dieter Jundt, Robert F. Curl, and Frank K. Tittel, *Room-temperature mid-infrared laser sensor for trace gas detection.* APPLIED OPTICS, 1997. **36**(30).

34. Marc N. Fiddler, I.B., Matthew A. Mickens, Michael S. Collingwood , Zerihun Assefa and Solomon Bililign, *Laser Spectroscopy for Atmospheric and Environmental Sensing*. Sensors 2009. **9**: p. 10447-10512.
35. Russell S. Harmon, F.C.D., Catherine E. McManus, Nancy J. McMillan, Thomas F. Jenkins, Marianne E. Walsh, Andrzej Miziolek, *Laser-induced breakdown spectroscopy – An emerging chemical sensor technology for real-time field-portable, geochemical, mineralogical, and environmental applications*. Applied Geochemistry, 2006(5): p. 730-747.
36. Konstantin L. Moskalenko, A.I.N., Inna A. Adamovskaya, *Human breath trace gas content study by tunable diode laser spectroscopy technique*. Infrared Physics & Technology, 1996. **37**(1): p. 181-192.
37. Joseph G. Morelli, M.O.T.T., MD; William L. Weston, MD *Treatment of Ulcerated Hemangiomas With the Pulsed Tunable Dye Laser* Am J Dis Child, 1991. **145**(9): p. 1062-1064.
38. Svanberg, S., *Environmental and Medical Applications of Photonic Interactions*. Physica Scripta, 2004. **T110**: p. 39-50.
39. Daniel Barolet, M., *Light-Emitting Diodes (LEDs) in Dermatology*. semin in cutan med and surg, 2008. **Elsevier**(27): p. 227-238.
40. Al-Ali, A., *Blood Parameter Measurement System* 2006: USA.
41. Haida Liang, B.P., Michael Hughes, Adrian Podoleanub, Marika Spring, David Saundersd. *Optical Coherence Tomography for Art Conservation & Archaeology*. in *Proc. SPIE 6618*. 2007.
42. N. Spooner, M.A., B. Smith, M. Franks and C. McElroy, *Archeological Dating by Infrared Stimulated Luminescence using a Diode Array*. Radiation Protection Dosimetry, 1990. **34**(114): p. 83-86.
43. Bimber, R.H.a.O., *Display: Fundamentals & applications*. 2011, Boca Raton, FL: A K Peters/CRC Press.
44. J. Chaves, F.M., J. C. Miñano, P. Benitez, B. Parkyn, W. Falicoff, Y. Sun. *Virtual filaments that mimic conventional light bulb filaments*. in *Nonimaging Optics and Efficient Illumination Systems*. 2004. SPIE.
45. R. L. Gunshora, A.V.N.a.N.O. *Blue II-VI laser Diodes and light Emitting Diodes*. in *Semiconductor Heterostructures for Photonic and Electronic Applications*. 1992.
46. Mottier, P., *LED for Lighting Applications*. 2009: Wiley.
47. Won Yong Lee, Y.C.L., Kirill Sokolov, Hee Joong Lee, Il Moon. *LED projection displays*. in *Nonimaging Optics and Efficient Illumination Systems*. 2004. SPIE.
48. Kasap, S.O., *Optoelectronic Devices and Photonics: Principles and Practices*. 2001, Upper Saddle River, NJ: Prentice Hall. 107-130.
49. Silfvast, W.T., *Laser Fundamentals*. Second ed. 2004, Cambridge: Cambridge University Press. 642.
50. BRIAN R. BENNETT, R.A.S., JESUS A. DEL ALAMO, , *Carrier-Induced Change in Refractive Index of InP, GaAs, and InGaAsP*. IEEE JOURNAL OF QUANTUM ELECTRONICS, 1990. **26**(1): p. 113-122.
51. Mendoza-Alvarez, J.G.Y., R. H.; Coldren, L. A., *Contribution of the band-filling effect to the effective refractive-index change in double-heterostructure GaAs/AlGaAs phase modulators*. Journal of Applied Physics, 1987. **62**(11): p. 4548-4553

52. Louay Eldada, M.N.R., Robert Scarmozzino, Miguel Levy, and Richard M. Osgood, Jr., *Laser-Fabricated Low-Loss Single-Mode Waveguiding Devices in GaAs*. Journal of Lightwave Technology, 1992. **10**(11): p. 1610-1616.
53. Marsh, J.H., *Quantum well intermixing*. Semicond. Sci. Technol, 1993. **8**: p. 1136-1155.
54. Kan'an, A.M., et al., *Area-selective disordering of multiple quantum well structures and its applications to all-optical devices*. J. Appl. Phys, 1996. **80**(6).
55. Daniel Hofstetter, B.M.o., and Hans P. Zappe, *Quantum-Well Intermixing for Fabrication of Lasers and Photonic Integrated Circuits*. IEEE J. of Selected Topics in Quantum Electronics, 1998. **4**(4): p. 794-802.
56. D. Hofstetter, D.S., C. Dunnrowicz, M. Kneissl, and D. W. Treat, *Multiwavelength Light Emitters for Scanning Applications Fabricated by Flipchip Bonding*. IEEE Photonics Technology Letters, 1998. **10**(10): p. 1371-1373.
57. A. François, V.A., J. Beauvais, M. Gendry and P. Regreny, *Enhancement of quantum well intermixing on InP/InGaAs/InGaAsP heterostructures using titanium oxide surface stressors to induce forced point defect diffusion*. Appl. Phys. Lett., 2006. **89**(164107).
58. A. Saher Helmy, S.K.M., A. C. Bryce, J. S. Aitchison, J. H. Marsh et al., *Control of silica cap properties by oxygen plasma treatment for single-cap selective impurity free vacancy disordering*. Appl. Phys. Lett., 1999. **74**(5): p. 732-734.
59. H. S. Djie, J.A., T. Mei, X. H. Tang, L. K. Ang et al., *Large blueshift in InGaAs/InGaAsP laser structure using inductively coupled argon plasma-enhanced quantum well intermixing*. Journal of Vacuum Science and Technology B, 2003. **21**: p. L1-L4.
60. X. F. Liu, B.C.Q., M. L. Ke, A. C. Bryce, and J. H. Marsh, *Control of Multiple Bandgap Shifts in InGaAs-AlInGaAs Multiple-Quantum-Well Material Using Different Thicknesses of PECVD SiO<sub>2</sub> Protection Layers*. IEEE Photonics Technology Letters, 2000. **12**(9): p. 1141-1143.
61. Henry, C.H., R.A. Logan, and K.A. Bertness, *Spectral dependence of the change in refractive index due to carrier injection in GaAs lasers*. J. Appl. Phys, 1981. **5**(27).
62. T. C. Huang, Y.C., D. B. Young, N. Dagli, and L. A. Coldren, *A Field Induced Guide-Antiguide Modulator on GaAs-AlGaAs*. IEEE PHOTONICS TECHNOLOGY LETTERS, 1991. **3**(2): p. 141-143.
63. P. A. Chen, C.J.a.C.Y.C., *Carrier-Induced Energy Shift in GaAs/AlGaAs Multiple Quantum Well Laser Diodes*. Journal of Quantum Electronics, 1993. **29**(10): p. 2607-2618.
64. May-Arrijoja, D.A., N. Bickel, and P. LiKamWa. *Integrated beam-steered optical switch*. in SPIE. 2004.
65. Coldren, L.A., *Monolithic Tunable Diode Lasers*. IEEE J. of Selected Topics in Quantum Electronics, 2000. **6**(6): p. 988-999.
66. Stewart D. McDougall, O.P.K., Craig J. Hamilton, Fernando Camacho, Bocang Qiu, Maolong Ke, Richard M. De La Rue, A. Catrina Bryce and John H. Marsh, *Monolithic Integration via a Universal Damage Enhanced Quantum-Well Intermixing Technique*. IEEE J. of Selected Topics in Quantum Electronics, 1998. **4**(4): p. 636-646.
67. Daniel Hofstetter, B.M.o., and Hans P. Zappe, *Quantum-Well Intermixing for Fabrication of Lasers and Photonic Integrated Circuits*. IEEE J. of Selected Topics in Quantum Electronics, 1998. **4**: p. 794-802.

68. Abdullah Zakariya, N.B.a.P.L. *Controlled intermixing of multiple quantum wells for broadly tunable integrated lasers*. in *Proc. SPIE*. 2011.
69. Xuesong Dong, P.L., John Loehr and Ron Kaspi, *Current-Induced Guiding and Beam Steering in Active Semiconductor Planar Waveguide*. IEEE Photonics Technology Letters, 1999. **11**(7).
70. Lalitha Ponnampalam, N.D.W., Richard Barlow, Giacinto Busico, and J.P.D. Andrew J. Ward, and David J. Robbins, *Dynamically Controlled Channel-to-Channel Switching in a Full-Band DS-DBR Laser*. IEEE Journal of Quantum Electronics, 2006. **42**(3): p. 223-230.
71. G. M. Smith, J.s.H., R. M. Lammert, M. L. Osowslu, G. C. Papen, J. T. Verdeyen, and J. J. Coleman, *Wavelength-Tunable Asymmetric Cladding Ridge-Waveguide Distributed Bragg Reflector Lasers with Very Narrow Linewidth*. IEEE Journal of Quantum Electronics, 1996. **32**(7): p. 1225-1229.
72. Ghulam Hasnain, K.T., L. Yang, Y. H. Wang, R. J. Fischer, James D. Wynn, Bonnie Weir, Niloy K. Dutta and Alfred Y. Cho, *Performance of Gain-Guided Surface Emitting Lasers with Semiconductor Distributed Bragg Reflectors*. IEEE J. of Selected Topics in Quantum Electronics, 1991. **27**(6): p. 1377-1385.
73. Larry A. Coldren, G.A.F., Y. Akulova, J. S. Barton, L. Johansson and C.W. Coldren, *Tunable Semiconductor Lasers: A Tutorial*. Journal of Lightwave Technology, 2004. **22**(1): p. 193-202.
74. Beck Mason, G.A.F., Steven P. DenBaars, and Larry A. Coldren, *Widely Tunable Sampled Grating DBR Laser with Integrated Electroabsorption Modulator*. IEEE Photonics Technology Letters, 1999. **11**(6): p. 638-640.
75. Lars E. Eng, K.B., Wupen Yuen, James S. Harris, Jr., and a.C.J. Chang-Hasnain, *Multiple-Wavelength Vertical Cavity Laser Arrays on Patterned Substrates*. IEEE J. of Selected Topics in Quantum Electronics, 1995. **1**(2): p. 624-628.
76. C. Juang, J.K.H., I. S. Yen, H. S. Shiau, *Photoluminescence of CF<sub>4</sub>/O<sub>2</sub> reactive ion etched In<sub>0.53</sub>Ga<sub>0.47</sub>As surfaces*. J. Appl. Phys. , 1992. **72**(2): p. 685-687.
77. David J. Meyer, J.R.F., and Joan M. Redwing. *Pre-passivation Plasma Surface Treatment Effects on Critical Device Electrical Parameters of AlGaIn/GaN HEMTs*. in *CS MANTECH Conference*. 2008.
78. T. S. Shamirzaev, A.L.S., K. S. Zhuravlev, A. Yu. Kobitski, H. P. Wagner, D. R. T. Zahn, *Changes in the density of nonradiative recombination centers in GaAs/AlGaAs quantum-well structures as a result of treatment in CF<sub>4</sub> plasma*. Semiconductors, 2002. **36**(1): p. 81-84.
79. Dong, X., et al., *Current-Induced Guiding and Beam Steering in Active Semiconductor Planar Waveguide*. IEEE Photonics Technology Letters, 1999. **11**(7).
80. Abdullah Zakariya, T.H.a.P.L. *Monolithic Optical Beam Steering over Selectively Intermixed GaAs/AlGaAs QW Laser Structure*. in *Frontier in Optics*. 2012. Rochester, New York United States: OSA.
81. Abdullah Zakariya, P.L. *Monolithic Tunable Laser based on Selectively Intermixed GaAs/AlGaAs QW Structure*. in *IEEE Photonics Conference*. 2012. IEEE.
82. C. Kim, D.A.M.-A., P. LiKamWa, P. Newman, J. Pamulapati, *Ultrafast all-optical multiple quantum well integrated optic switch*. Electronics Letters, 2000. **36**(23): p. 1929-1930.
83. Dilouie, C., *Advanced Lighting Controls*. 2006, Lilburn, Ga: The Fairmont Press.

84. Pierre Mahou, M.Z.K.L., Katherine S Matho, Guillaume Labroille, Xavier Morin, Willy Supatte, Jean Livet, Delphine Débarre and Emmanuel Beaurepaire, *Multicolor two-photon tissue imaging by wavelength mixing*. Nature Methods, 2012. **8**: p. 815-821.
85. Shuailong Zhang, S.W., Jonathan J. D. McKendry, David Massoubre, Andrew Cogman, Erdan Gu, Robert K. Henderson, Anthony E. Kelly, and Martin D. Dawson, Journal of Lightwave Technology, 2013. **31**(8): p. 1211-1216.
86. Seungyong Jung, S.S., Gela Kipshidze, David Westerfeld, Eric Golden et al, *Dual wavelength GaSb based type I quantum well mid-infrared light emitting diodes*. Appl. Phys. Lett., 2010. **96**(19): p. 191102.
87. Michael J. Grundmann, U.K.M., *Multi-color light emitting diode using polarization-induced tunnel junctions*. phys. stat. sol., 2007. **4**(7): p. 2830–2833.
88. al., S.K.e., *Multi-color Light Emitting Device*, U.S. Patents, Editor. 1996, Kabushiki Kaisha Toshiba: Japan.
89. Ragle, L., *Integrated Color LED Chip*. 2004, The Fox Group, Inc.: USA.
90. Hiroto Sekiguchi, K.K., and Akihiko Kikuchi, *Emission color control from blue to red with nanocolumn diameter of InGaN/GaN nanocolumn arrays grown on same substrate*. Appl. Phys. Lett., 2010. **96**: p. 231104-1-231104-3.
91. Michael C. Y. Chan, P.C.K.K., and E. Herbert Li, *The Effect of Carrier-Induced Change on the Optical Properties of AlGaAs–GaAs Intermixed Quantum Wells*. IEEE J. of Selected Topics in Quantum Electronics, 1998. **4**(4): p. 685-693.
92. Abdullah Zakariya, P.L. *Multiple Wavelength LED on Monolithic QW structure*. in *SPIE: Optics & Photonics*. 2012. SPIE.
93. Abdullah Zakariya, P.L. *Monolithic Single Output Dual Wavelength LED*. in *IEEE Photonics Conference 2012*. IEEE.